High resolution Large-Eddy Simulation of turbulent flow around buildings

Von der Fakultät für Mathematik und Physik
der Gottfried Wilhelm Leibniz Universität Hannover
zur Erlangung des Grades
Doktor der Naturwissenschaften
Dr. rer. nat.
genehmigte Dissertation
von

Dipl.-Met. Marcus Oliver Letzel MSc (Univ. of Reading)

geboren am 1. Februar 1974 in Heessen (jetzt Hamm)

2007

To my family

Abstract

The aim of the thesis was to extend the LES model PALM that is developed by Dr. Raasch to allow flow around explicitly resolved obstacles. This forms the basis of future applications for example in the fields of wind engineering and urban climate. The latter is the subject of this thesis. A commissioned urban LES study for an interdisciplinary research project in Hong Kong is also part of this thesis.

Since urban LES involves a huge number of grid points, implementation of the obstacles required optimal performance on the various architectures of today's supercomputers. The urban PALM code was successfully validated with a large model intercomparison based on a well-documented wind tunnel reference experiment. Feasibility studies of turbulent urban flow visualization were performed in close cooperation with the DFG project EVITA at the L3S and at the Regional Scientific Computing Center for Lower Saxony of the Leibniz University of Hannover for various city quarters of Tokyo, Hong Kong and Hannover. The main part of this thesis is a parameter study of the turbulence characteristics of the urban street canyon circulation driven by perpendicular wind for neutral and convective boundary layers. The most important results are: 1) A new concept of a "cavity shear layer" was developed that complements classical free shear layer concepts. 2) For the first time in urban LES Kelvin-Helmholtz instabilities were identified at the top of the urban street canyon. This is relevant for modelling urban dispersion, because the street canyon circulation is more intermittent than suggested by previous RANS results. 3) Integral turbulence profiles in deep canyons were found to scale with canyon depth. This is relevant for urban canopy parameterizations in larger-scale meteorological models.

Overall, this study demonstrated the promising potential of urban large-eddy simulation for both fundamental and applied urban research. Given the ever rising computational power, properly validated urban LES could mature to a powerful research tool within the next few years.

Keywords: Urban climate, bluff body flow, Large-Eddy Simulation

Zusammenfassung

Ziel ist dieses Dissertationsvorhabens war es, das von Herrn Raasch entwickelte und von seiner Arbeitsgruppe betriebene und weiterentwickelte LES-Modell PALM dahingehend zu erweitern, dass PALM Inhomogenitäten fortan nicht nur wie bisher durch Variation von Oberflächeneigenschaften wie z.B. Bodenwärmestrom oder Rauigkeitslänge berücksichtigt, sondern auch in Form echter Hindernisumströmung. Damit wird der Grundstein für praxisnähere Anwendungen z.B. in Fragen der Windenergieerzeugung und der Stadtklimatologie gelegt. Letztere sind Gegenstand dieses Dissertationsvorhabens. Dienstleistungen auf diesem Gebiet wurden für ein interdisziplinäres Forschungsprojekt in Hong Kong erbracht und sind daher ebenfalls Gegenstand dieses Dissertationsvorhabens.

Bei der Implementation der Hindernisse in PALM wurde großer Wert auf eine weiterhin optimale Performance auf den verschiedenen Architekturen heutiger Höchstleistungsrechner gelegt. Die urbane PALM-Modellversion wurde erfolgreich mit einer groß angelegten Modellvergleichsstudie auf Basis eines gut dokumentierten Windkanalreferenzexperimentes validiert. Machbarkeitsstudien zur urbanen Strömungsvisualisierung wurden in enger Kooperation mit dem DFG-Projekt EVITA am L3S und am Regionalen Rechenzentrum für Niedersachsen der Leibniz Universität Hannover für verschiedene Stadtteile von Tokyo, Hong Kong sowie Hannover durchgeführt. Den Hauptteil dieser Dissertation bildet eine Parameterstudie zu den Turbulenzeigenschaften bei Querüberströmung von Straßenschluchten sowohl für neutrale als auch labile thermische Schichtung.

Die wesentlichen Ergebnisse sind: 1) Ein neues Konzept für die freie Scherströmung auf Dachhöhe ergänzt klassische Konzepte freier Scherströmungen. 2) Erstmals konnten in einer urbanen LES Kelvin-Kelmholtz Instabilitäten auf Dachhöhe identifiziert werden. Dies ist von Bedeutung für die Modellierung städtischer Schadstoffausbreitung, denn die Intermittenz der Straßenschluchtzirkulation ist größer als RANS Modelle bisher vermuten ließen. 3) Integrale Turbulenzstatistiken in tiefen Straßenschluchten skalieren vertikal mit der Straßenschluchtbreite. Dies ist von Bedeutung für urbane Parametrisierungen in größerskaligen meteorologischen Modellen.

Insgesamt zeigt die vorliegende Arbeit deutlich das vielversprechende Potential urbaner LES sowohl für Fragen der Grundlagenforschung als auch für Fragen der angewandten Stadtklimatologie. Angesichts beständig wachsender Rechnerressourcen könnte eine sorgfältig validierte urbane LES innerhalb der nächsten Jahre zu einem leistungsstarken Forschungswerkzeug heranreifen.

Schlagwörter: Stadtklima, Gebäudeumströmung, Large-Eddy Simulation

Acknowledgements

Finally, my greatest thanks go to my family and especially to my wife Motoko, not only for trying to spot and correct my "German" English, but most of all for her endurance during this time of my frequent physical – or mental – absence.

Contents

Contents

List of Figures

List of Tables

List of Symbols

Roman symbols

A	upper canyon vortex aspect ratio
$c_m = 0.1$	Smagorinsky constant
d	normal distance to the nearest solid surface
D	direct pressure gradient
e	subgrid-scale turbulent kinetic energy
f	Coriolis parameter
F	body force
g	acceleration due to gravity
H	cube or canyon height
i, j, k	integer indices
K_m, K_h, K_s	turbulent diffusion coefficients for momentum, heat and scalars
l	mixing length
L	Obukhov length or street canyon length
n	number of grid points per dimension
p	air pressure
R	resolution in grid points per canyon width W; total momentum flux
Re_δ	Reynolds number for a free-stream layer of depth δ
Re_H	Reynolds number for a canyon or cube of height H
Ri_f	Richardson flux number
s	a scalar
t	time
T	averaging time
$u, v, w;\ u_i$	streamwise, spanwise and vertical velocity components (except chapter 3: streamwise, vertical and spanwise components)
u_b	bulk velocity

List of Symbols

u_H	streamwise velocity at canyon height H
u_*	friction velocity
U	mean wind speed
V	volume of a grid cell
W	canyon width
$x, y, z;\ x_i$	streamwise, spanwise and vertical Cartesian coordinates (except chapter 3: streamwise, vertical and spanwise coordinates)
$z_{0,\text{loc}}$	local wall roughness length

Greek symbols

δ	depth of free-stream layer
δ_{ij}	Kronecker delta
$\Delta;\ (\Delta_h, \Delta x, \Delta y, \Delta z)$	grid length (in horizontal, x, y, z direction)
Δ_p	local Prandtl-layer thickness
ϵ	dissipation of subgrid-scale turbulent kinetic energy
ε_{ijk}	Levi-Civita symbol (permutation symbol, antisymmetric symbol)
φ	geographical latitude
ϕ	an atmospheric variable
$\kappa = 0.4$	von Kármán constant
ν_m, ν_h, ν_s	molecular viscosities for momentum, temperature and scalars
Ω	angular velocity of the Earth
ψ	stream function
ρ	air density
σ	standard deviation
τ	stress tensor
θ	potential temperature
ζ	vorticity

Operators

$_0$	basic state (Boussinesq approximation)
$*$	departure from the basic state (Boussinesq approximation)
$'$	resolved-scale turbulent fluctuation

$''$	subgrid-scale fluctuation
$\overline{\dots}$	Reynolds average (chapter 2: spatial average of unfiltered variables; later chapters: temporal average of resolved-scale variables)
$\langle \dots \rangle$	spanwise average
$[\dots]$	horizontal average
∂	partial derivative

List of Abbreviations

ABL   Atmospheric boundary layer

BL   Boundary layer

BMBF   Bundesministerium für Bildung und Forschung (German Federal Ministry of Education and Research)

CBL   Convective boundary layer

CEDVAL   Compilation of Experimental Data for Validation of Microscale Dispersion Models

CFD   Computational fluid dynamics

DEM   Digital elevation model

DFG   Deutsche Forschungsgemeinschaft (German Research Foundation)

DIN   Deutsches Institut für Normung e.V. (German Institute for Standardization)

DKRZ   Deutsches Klimarechenzentrum (German Climate Computing Centre), Hamburg

DNS   Direct numerical simulation

DVR   Distributed Virtual Reality

DVRP   DVR Parallelized

DSVR   Distributed Simulation and Virtual Reality Environment

ERCOFTAC   European Research Community on Flow, Turbulence and Combustion

FFT   Fast Fourier Transform

GIS   Geographic information system

HKSAR   Hong Kong Special Administrative Region

HLRN   Norddeutsches Rechenzentrum für Hoch- und Höchstleistungsrechnen (German High-Performance Computing Center North)

HPC   High-performance computing

IMUK   Institut für Meteorologie und Klimatologie (Institute of Meteorology and Climatology), LUH

IPCC   Intergovernmental Panel on Climate Change

IRF   Isolated roughness flow

ISL	Inertial sublayer
K-E	Standard k-ϵ model after Launder and Spalding (1974) with wall function (Launder and Sharma, 1974)
KATO-L	Kato-Launder k-ϵ model after Kato and Launder (1993)
L3S	Learning Lab Lower Saxony, Hannover
LES	Large-eddy simulation
LUH	Leibniz Universität Hannover (Leibniz University of Hannover)
MOST	Monin-Obukhov similarity theory
MPI	Message-Passing Interface
PALM	Parallelized large-eddy simulation model
PBL	Planetary boundary layer
RANS	Reynolds-averaged Navier-Stokes equations
RNG	Renormalization group k-ϵ model after Yakhot et al. (1992)
RRZN	Regionales Rechenzentrum für Niedersachsen (Regional Scientific Computing Center for Lower Saxony), LUH
RSL	Roughness sublayer
SF	Skimming flow
SGS	Subgrid-scale
SGS-TKE	Subgrid-scale turbulent kinetic energy
TKE	Turbulent kinetic energy (resolved-scale)
TWO-L	two layer k-ϵ model after Rodi (1991)
UBL	Urban boundary layer
UCL	Urban canopy layer
VDI	Verein deutscher Ingenieure e.V. (Association of German Engineers)
WIF	Wake interference flow
ZIB	Konrad-Zuse-Zentrum für Informationstechnik, Berlin
ZIM	Zentrum für Informations- und Medientechnologie (Center of Information and Media Technology), University of Düsseldorf

1 Introduction

1.1 Urban climate research

The interactions between urban areas and the atmosphere have received growing attention in urban climate research in the last decades. In the terminology of Oke (2006) "urban climate" today comprises a rich variety of related disciplines such as geography, boundary layer meteorology, fluid dynamics and wind engineering, civil engineering, mechanical engineering, architecture, city planning, and many more. This development is to a great extent owing to the growing proportion of the world population living in urban areas and owing to the concern for comfort and well-being of these urban inhabitants. It is reflected by recent general reviews e.g. by Mestayer and Anquetin (1995), Arnfield (2003), Collier (2006), and Souch and Grimmond (2006).

The discipline of modern urban climate research started with the pioneering works of Luke Howard on the climate of London (Howard, 1818-1820, 1833) and the comprehensive monographies by Kratzer (1937, 1956). By the end of the 19th century the systematic temperature difference between cities and their surroundings that is characteristic of the urban heat island phenomenon was known for large European cities including Berlin, London, Paris, and Vienna (Landsberg, 1956, 1981). The main challenges in the 20th century were the urban heat island problem (Oke, 1995) and urban air quality issues (Helbig et al., 1999).

Nowadays urban areas face additional challenges. Recent work of the Intergovernmental Panel on Climate Change, IPCC, has raised public awareness about local and regional impacts of climate change that will be also felt in some urban areas in the form of increased threats of heat waves and declining air quality (IPCC WGII, 2007). Cities respond with mitigation attempts from local scale (for example the restoration of the Cheonggye Stream in downtown Seoul; cf. Ichinose et al., 2006) to regional scale (for example the Sustainable Development Strategy for Hong Kong; cf. chapter 6). Furthermore, urban areas are vulnerable to accidental or malicious release of harmful materials – as soft targets they are at increased risk in today's geopolitical context (Settles, 2006).

These challenges have directed research into fields like urban airflow and pollutant dispersion, cf. the reviews by Fernando et al. (2001), Robins and Macdonald (2001), Britter and Hanna (2003), Robins (2003), Hunt et al. (2004), Belcher (2005) and Batchvarova and Gryning (2006). They are mainly studied experimentally (field study, wind tunnel, water tank) or numerically (see section 1.3), often using scale models (Kanda, 2006). The present numerical study is mainly concerned with the airflow *within* the *urban canopy layer* (UCL). The UCL is part of a set of concepts that are used to describe the urban boundary layer and to divide it into typical vertical and horizontal scales. These concepts will be described in the following section 1.2.

1.2 Definition of scales

Compared to the structure of the atmospheric/planetary boundary layer (ABL/PBL, Stull, 1988; Sorbjan, 1989), the structure of the urban boundary layer (UBL) is more complex,
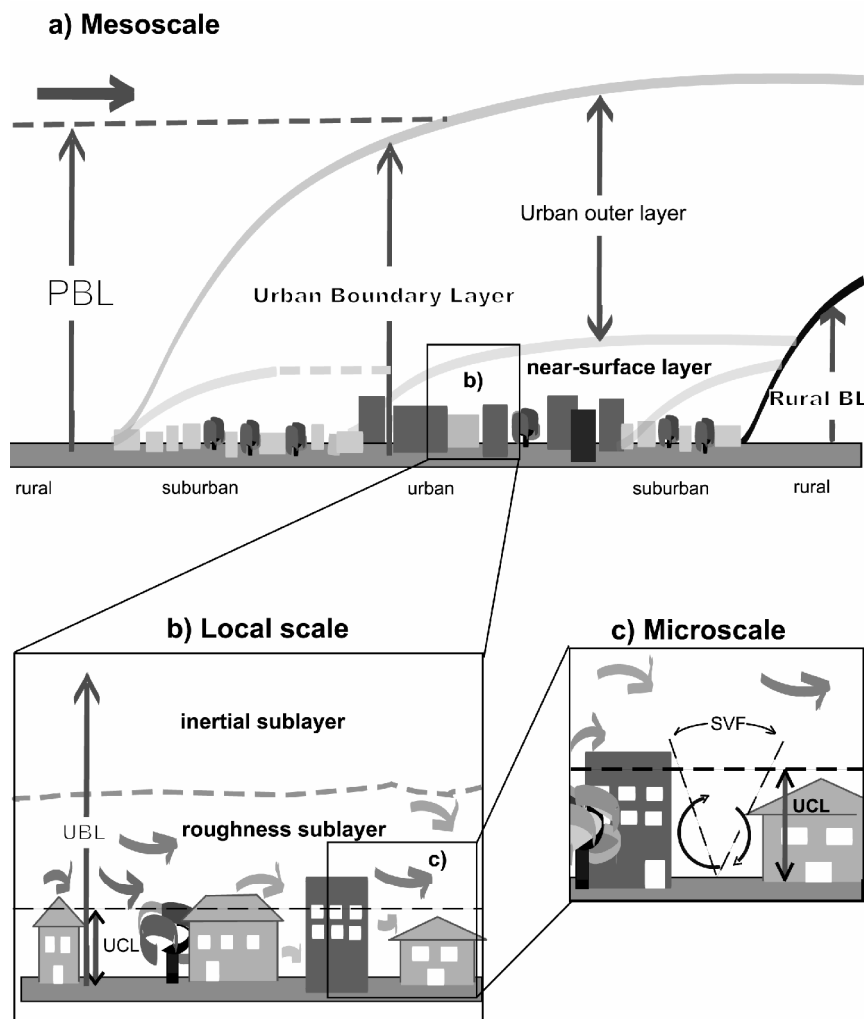
Figure 1.1: Layer concept in urban climatology, reprinted with kind permission from Rotach et al. (2005). Abbreviations: BL: boundary layer; PBL: planetary BL; UBL: urban BL; UCL: urban canopy layer; SVF: sky-view factor.

especially close to the urban fabric. The vertical structure of the UBL is usually described using a conceptual model of vertical layers that was originally developed by Oke (cf. Oke, 1987) by analogy with internal boundary layers that develop over patches of different underlying roughness (Smits and Wood, 1985; Kaimal and Finnigan, 1994). Note that this analogy assumes that dynamical processes dominate the UBL. Oke's concept has been refined subsequently; as an example Figure 1.1 shows a recent layer concept that links vertical and related horizontal urban scales (Rotach et al., 2005). Mestayer and Anquetin (1995) discuss the respective merits and limitations of several conceptual urban models including those with focus on thermal processes (the "urban dome") for explanation of the urban heat island.

The lowest vertical layer is the *urban canopy layer* (UCL) from the ground to the average building height (Fig. 1.1b,c). In the UCL air flow is dominated by turbulent structures associated with individual roughness elements. (For bluff body flow, processes such as flow separation, recirculation and channeling were already observed by Leonardo da Vinci (1452–1519), see Figure 1.2.) Therefore the UCL strongly depends on the local urban morphology.
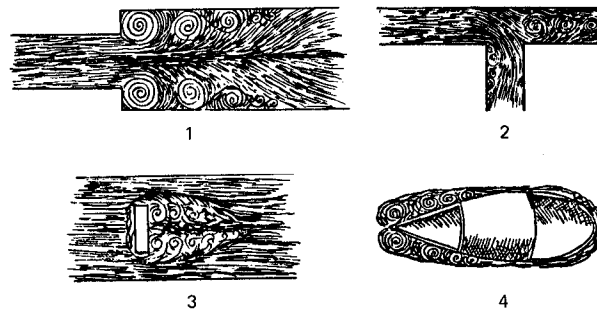
Figure 1.2: Sketches of turbulent bluff body flow from Leonardo da Vinci (1452–1519) (taken from Lugt, 1983).

The *roughness sublayer* (RSL; Fig. 1.1b) extends up to a height where the influence of individual roughness elements vanishes. This blending height is typically 1.5 to 4 times the mean building height (Christen, 2005). The RSL exhibits horizontally and vertically inhomogeneous turbulence statistics, because the flow still feels the underlying individual roughness elements through local advection and horizontal fluxes (referred to as *dispersive fluxes*).

Starting from the *inertial sublayer* (ISL) and above (Fig. 1.1a,b), standard boundary layer theory can be applied, because the flow feels the city only as a rough surface. For example, turbulent fluxes are constant with height and Monin-Obukhov similarity theory generally applies in the urban ISL.

Belcher (2005) distinguishes these layers based on the governing physical processes: in the ISL only turbulent stress acts, in the RSL additionally dispersive fluxes act, and in the UCL additionally aerodynamic drag of the obstacles acts.

Many processes in the UCL and RSL are not yet well-understood, which is why these layers are in the focus of many recent research studies including the present one.

Britter and Hanna (2003) suggest four characteristic horizontal urban scales (Figure 1.3): regional (up to 100 or 200 km), city scale (up to 10 or 20 km), neighbourhood or local scale (Fig. 1.1b; up to 1 or 2 km) and street scale or microscale (Fig. 1.1c; less than 100∼200 m). Figure 1.3 shows an illustration of such urban scales for the city of Basel (Christen, 2005). These scales are useful to illustrate the traditional fields of application of various numerical models in the following section.

1.3 Numerical modelling in urban climate research

In urban climate research both engineering-based and meteorology-based numerical codes are used today. The former had originally been developed for the small microscale that is typical of engineering, the latter for the large scales of weather forecasting and climate modelling. The growing computational power has allowed the former to extend to larger scales (by increase of domain size) and the latter to extend to smaller scales (by increase of grid resolution). Still, there are important differences between different modelling types, especially regarding the way turbulence is treated.

Urban regional or mesoscale models (Pielke, 2002, chapter 13.1.5) were the first 3D urban meteorological models. Today, the resolution of operational weather forecasting models is fine enough to resolve larger cities (Best, 2006), while the resolution of the formerly mesoscale models can now reach down to the city and even to the neighbourhood scale. However, turbulent processes are not explicitly resolved in such models and need to be parameterized

Figure 1.3: Illustration of characteristic scales and their urban morphology in the city of Basel. Photos by courtesy of M. Roth, NUS Singapore, and R. Vogt, University of Basel, reprinted with kind permission from Christen (2005).

(Masson, 2006). The limited computer power did not allow engineering models to explicitly simulate turbulent processes in the early days, either.

This has changed somewhat with the onset of numerical turbulence modelling. Letzel (2001) gave an overview of numerical turbulence modelling with focus on Large-eddy simulation (LES) and on the differences between LES, direct numerical simulation and Reynolds-averaged Navier Stokes equation modelling, including a short history of LES. Only the main findings relevant to this study are repeated here and built-upon (for details see also textbooks by Breuer, 2002; Ferziger and Perić, 2002; Fröhlich, 2006; Sagaut, 2006).

In numerical urban climate research, computational fluid dynamics (CFD) models based on the *Reynolds-averaged Navier Stokes* (RANS) equations have traditionally been widely used because of their low cost and relatively reasonable accuracy – despite of known shortcomings for flow around obstacles. They do not explicitly resolve turbulence, instead they parameterize the entire turbulence spectrum, e.g. with the $k - \epsilon$ turbulence closure model, which allows quick and thus inexpensive calculations. It is important to realize that RANS models simulate and thus produce ensemble averages only, i.e. no instantaneous turbulent data (cf. section 2.1, especially the discussion on page 9).

Direct Numerical Simulation (DNS) is the other extreme: here, all turbulent scales down to the Kolmogorov dissipation length (mm scale) are explicitly resolved. Due to its extreme computational demands, for the foreseeable future DNS will remain a pure research tool because it cannot be applied to natural scales with realistic Reynolds numbers[1].

Large-eddy simulation is in between these two approaches, because its concept is to treat large and small scales separately: LES explicitly resolves all scales of the large, energy-containing eddies and parameterizes all smaller eddies that are statistically similar (based on Kolmogorov's first hypothesis). This means that LES is a compromise between RANS and DNS both in terms of computational cost and accuracy, and ideally, it should combine the

---

[1]For a definition of the Reynolds number see equation (3.1) on page 19.

strengths of both. However, since the computational cost of LES is several times that of RANS, it was only in recent years that computers have become powerful enough to allow practical LES applications at full scale; such an example will be presented in chapter 6. The present study uses the *pa*rallelized *l*arge-eddy simulation *m*odel PALM that will be introduced in chapter 2.

Except for an improved accuracy, the most striking benefit of LES compared to conventional CFD (RANS) is that – as in field or wind tunnel measurements – LES is able to capture turbulent fluctuations in both space and time. This becomes important wherever knowledge about peak values or instantaneous values is required, in the urban context for example for wind gusts or pollutant concentrations. This means that the image of Schatzmann and Leitl (2002, Fig. 1), who contrasted the capabilities of field and wind tunnel turbulence measurements on the one side with "numerical grid modelling" on the other side, should be revised: (properly validated) LES is in the same class as field and wind tunnel studies, as opposed to RANS.

In fact, LES offers extra benefits compared to most wind tunnels: virtual measurements in 4D (time series at each grid point) at no extra cost, extensive (even simultaneous) parameter studies, exactly reproducible results and thermal stratification. Still, there are caveats of the LES approach. It is difficult to supply initial and boundary conditions with sufficient accuracy to drive LES for a direct comparison with field data (Weinbrecht et al., 2004). Direct comparison with wind tunnel data is easier but LES cannot play its full strength of simulating natural scales with realistic Reynolds numbers in such a comparison. Whereas conventional CFD/RANS models converge to a steady solution, by their very nature LES models do not, since turbulence can only become quasi-steady. To compare LES (or wind tunnel data) with RANS thus needs time-(space)-averaging. The time average needs to be long enough for statistically sound results. The resulting long simulation time is another reason of the higher cost of LES.

1.4 Scope and structure of this study

"The urban wind field is rarely simple" (Landsberg, 1981) —

this experience is perhaps a good aphorism for this study, because it is a common thread running through all chapters. This study is organized into several rather distinct chapters, each of which with an own introduction and motivation. Therefore, at this point, only a general, short overview is provided.

First, chapter 2 introduces the LES model *PALM* that is used in this study, paying special attention to the new urban code.

Chapter 3 presents a *validation* of the urban PALM version with a large LES and RANS model intercomparison based on a well-documented wind tunnel reference experiment. Although this experiment features only a single cube in turbulent channel flow, it exhibits a complex turbulent flow field.

Chapter 4 constitutes the main part of this study, it gives an example of fundamental research with urban LES: a parameter study of *urban street canyons*. Knowledge about the characteristics of the complex urban air flow is crucial for environmental issues such as air pollution and urban thermal comfort. This is especially true in poorly ventilated areas like street canyons. Therefore this study focusses on the turbulence within street canyons, with special emphasis on the deep canyon circulation that is driven by perpendicular ambient wind.

The paradigm of PALM is do as much "work" as possible on-the-fly on the supercomputer itself making maximal use of its efficiency (e.g. parallelization) in order to minimize post-processing. The calculation of turbulence statistics (section 4.3) follows this paradigm, but the *visualization of urban turbulence* in chapter 5 demonstrates the benefits (and challenges) of this paradigm even more clearly.

Chapter 6 gives an example of applied research with urban LES that is already possible today: a PALM simulation of the dense urban fabric of Tsim Sha Tsui in Kowloon, downtown *Hong Kong*. The task of this commissioned study was to investigate pedestrian level ventilation. Chapter 6 demonstrates how the knowledge and techniques from the previous chapters can be combined and applied to answer practical urban climate questions, and it also shows that today's supercomputers already provide the necessary computational power to do so.

Summary and conclusions are given in chapter 7.

2 Model description

This chapter describes the parallelized LES model PALM that has been used and extended for this study. PALM has been developed by Raasch and Etling (1991, 1998) and Raasch and Schröter (2001) at the Institute of Meteorology and Climatology of the Leibniz University of Hannover since the early 1990s.

PALM is a large-eddy simulation model whose application is the atmospheric (or oceanic) boundary layer. PALM is based on the filtered, non-hydrostatic, incompressible Boussinesq equations (section 2.1). Section 2.2 describes the numerical implementation. Section 2.3 deals with the subgrid-scale; it describes how relevant processes on scales that are smaller than the grid size are parameterized in PALM: turbulence closure and wall modelling. Section 2.4 deals with the supergrid-scale; it describes how scales that are larger than the model domain are represented in PALM. It comprises boundary conditions, initial conditions and driving modes. Section 2.5 briefly touches upon parallelization and performance issues.

Amendments to the model code are explained in the appropriate (sub)sections of this chapter: the mask method (Briscolini and Santangelo, 1989) used by Kanda et al. (2004) to explicitly resolve solid obstacles in the rectangular grid has been simplified for use in PALM (subsection 2.2.1) with modifications to optimize performance on both vector and parallel machines. The simulations performed in chapters 3 through 6 required the addition of new boundary and initial conditions and driving modes (section 2.4).

This chapter does not aim at a complete description of PALM but attempts a concise description with focus on those parts of the model that are relevant to this study or are affected by amendments. For full details and features, please refer to Raasch and Schröter (2001) and to the online documentation (available from `http://www.muk.uni-hannover.de/~raasch/PALM_group`). Recommendations for further reading (original works, reviews or textbooks) are given where appropriate.

2.1 Governing equations

The basis of the dry version of PALM that is used in this study are the Navier-Stokes equations of conservation of momentum, mass, internal energy (potential temperature) and other scalars for a viscous fluid without scalar sources or sinks. For a rotating, Cartesian frame of reference they read in tensor notation

$$\frac{\partial u_i}{\partial t} = -u_k \frac{\partial}{\partial x_k} u_i - \varepsilon_{ijk} f_j u_k - g\delta_{i3} - \frac{1}{\rho}\frac{\partial p}{\partial x_i} + \nu_m \left(\frac{\partial^2 u_i}{\partial x_j^2} + \frac{1}{3}\frac{\partial}{\partial x_i}\frac{\partial u_j}{\partial x_j} \right) \quad (2.1)$$

$$\frac{\partial \rho}{\partial t} = -\frac{\partial}{\partial x_i}(\rho u_i) \quad (2.2)$$

$$\frac{\partial \theta}{\partial t} = -u_k \frac{\partial}{\partial x_k}\theta + \nu_h \frac{\partial^2 \theta}{\partial x_j^2} \quad (2.3)$$

$$\frac{\partial s}{\partial t} = -u_k \frac{\partial}{\partial x_k}s + \nu_s \frac{\partial^2 s}{\partial x_j^2} \quad . \quad (2.4)$$

With indices $i, j, k \in [1, 2, 3]$, u_i are the three velocity components (also referred to as u, v, w), x_i (or x, y, z) are the corresponding directions in space, t is time, ρ the air density, p the air pressure, $f_i = (0; 2\Omega \cos \varphi; 2\Omega \sin \varphi)$ is the Coriolis parameter with Ω being the angular velocity of the Earth and φ the latitude, g is the acceleration due to gravity, θ the potential temperature, s a scalar, and ν_m, ν_h, ν_s are the molecular viscosities for momentum, temperature and the scalar, respectively. Wherever the same index appears twice in a term, summation over the index range is implied following the Einstein summation convention.

The above set of equations (2.1)-(2.4) undergoes a two-step process before it is used in PALM. Both steps will be outlined below. Detailed introductions are given in the following textbooks, for example:

1. *Boussinesq approximation*
   e.g. Etling (2002, chapter 12.7), Holton (2004, chapter 5.1.1), Stull (1988, chapter 3.3.3)

2. *Filtering*
   e.g., Breuer (2002, chapter 3.2), Fröhlich (2006, chapters 5.2-5.6), Sagaut (2006, chapters 2-3, 13.1-13.2)
   here: *Reynolds averaging*
   e.g. Fröhlich (2006, chapter 2.3), Holton (2004, chapter 5.1.2), Stull (1988, chapter 2.4.3)

In step one, the *Boussinesq (1903) approximation* splits the atmospheric state variables pressure, density and temperature, here designated as $\psi(x, y, z, t)$, into a basic state $\psi_0(z)$ and the departure $\psi^*(x, y, z, t)$ from the basic state

$$\psi(x, y, z, t) = \psi_0(z) + \psi^*(x, y, z, t) \quad . \tag{2.5}$$

The basic state varies only with height and fulfills both the hydrostatic equation and the equation of state for dry air. Density variations in the Navier-Stokes equations are neglected except for the buoyancy term where they are approximated as variations of potential temperature. This is convenient because temperature is easier to measure in the atmosphere than density. Numerical solution of the Boussinesq-approximated Navier-Stokes equations benefits from the incompressibility of the Boussinesq fluid (Etling, 1996, chapter 17.4). Incompressibility is inferred from the continuity equation (2.2) that reduces to the form for an incompressible, non-divergent fluid, if $\partial_z \rho_0 \approx 0$. Thus, sound waves cannot occur, which allows a time step reduction by an order of magnitude, i.e. a significant reduction of computational cost. The Boussinesq approximation is valid only for certain conditions (Mahrt, 1986) where the fluid is not too far from a hydrostatic state and departures are small, such as shallow convection ($z \lesssim 3000 \, \mathrm{m}$) simulated by PALM (Dutton and Fichtl, 1969).

In step two, equations (2.1)-(2.4) are averaged over discrete grid volumes (Raasch and Etling, 1991). The filter function can be written as

$$\overline{\psi}(V, t) = \frac{1}{\Delta x \Delta y \Delta z} \iiint_V \psi(V', t) \, \mathrm{d}V' \tag{2.6}$$

for corresponding discrete and non-overlapping grid volumes

$$V = \left[x - \tfrac{\Delta x}{2}, x + \tfrac{\Delta x}{2} \right] \times \left[y - \tfrac{\Delta y}{2}, y + \tfrac{\Delta y}{2} \right] \times \left[z - \tfrac{\Delta z}{2}, z + \tfrac{\Delta z}{2} \right] \quad . \tag{2.7}$$

This volume-balance approach (Schumann, 1975) has the advantage that the discretization acts as a Reynolds operator (Schumann, 1973). This approach is also referred to as *implicit*

filtering (Fröhlich, 2006, chapter 5.4) and it is similar to explicit filtering (Leonard, 1974) when using a top-hat (box) filter as filter function with the grid length as filter width (Breuer, 2002, chapter 3.2.1.3). Reynolds (1895) postulated that any atmospheric variable ψ can be decomposed into a "slowly varying" average $\overline{\psi}$ and a "rapidly varying" turbulent fluctuation ψ'':

$$\psi = \overline{\psi} + \psi'' \quad , \tag{2.8}$$

with the key property

$$\overline{\psi''} = 0 \quad , \tag{2.9}$$

and thus, with ϕ being a second atmospheric variable,

$$\overline{\phi \psi} = \overline{\phi}\,\overline{\psi} + \overline{\phi'' \psi''} \quad . \tag{2.10}$$

In this context "varying" is taken to refer to space, generally it refers to time and/or space. The filter (2.6)-(2.7) fulfills (2.8)-(2.10). In PALM (2.6)-(2.8) translate as follows: $\overline{\psi}(V,t)$ represents the spatial mean value of an atmospheric variable that is averaged over grid volume V at time t, and $\psi''(x,y,z,t)$ is the sub-gridscale, local spatial fluctuation at time t that is not resolved by the model.

(*This chapter* uses Reynolds averaging to distinguish the resolved scales that are denoted by an overbar and the unresolved subgrid-scale fluctuations that are denoted by a double prime ($''$). Note that *later chapters* use Reynolds averaging to temporally average resolved-scale variables ϕ, ψ. They will redefine the overbar to denote a resolved-scale time-average

$$\overline{\phi \psi} = \overline{\phi}\,\overline{\psi} + \overline{\phi' \psi'}, \tag{2.11}$$

and a single prime ($'$) will be used to denote a resolved-scale turbulent fluctuation.)

Applying steps one and two as outlined above to (2.1)-(2.4) and neglecting molecular diffusion yields the resulting governing equations of PALM, the filtered, non-hydrostatic, Boussinesq-approximated Navier-Stokes equations (conservation of momentum) that imply imcompressibility through the continuity equation (conservation of mass), the 1$^{\text{st}}$ law of thermodynamics (conservation of energy) and an equation for scalar conservation:

$$\frac{\partial \overline{u}_i}{\partial t} = -\frac{\partial}{\partial x_k} \overline{u}_k \overline{u}_i - \frac{1}{\rho_0}\frac{\partial \overline{p^*}}{\partial x_i} - (\varepsilon_{ijk} f_j \overline{u}_k - \varepsilon_{i3k} f_3 u_{g_k}) + g\frac{\overline{\theta^*}}{\theta_0}\delta_{i3} - \frac{\partial}{\partial x_k}\tau_{ki} \tag{2.12}$$

$$\frac{\partial \overline{u}_i}{\partial x_i} = 0 \tag{2.13}$$

$$\frac{\partial \overline{\theta}}{\partial t} = -\frac{\partial}{\partial x_k}\overline{u}_k\overline{\theta} - \frac{\partial}{\partial x_k}\overline{u_k'' \theta''} \tag{2.14}$$

$$\frac{\partial \overline{s}}{\partial t} = -\frac{\partial}{\partial x_k}\overline{u}_k\overline{s} - \frac{\partial}{\partial x_k}\overline{u_k'' s''} \quad . \tag{2.15}$$

Here u_g is the geostrophic wind defined by $\rho_0^{-1}\partial_{x_i}p_0 = \varepsilon_{i3k}f_3 u_{g_k}$, and $\tau_{ij} = \overline{u_i'' u_j''}$ is the subgrid-scale stress tensor (see subsection 2.3.1 on page 15).

Breuer (2002, chapter 3.2.4) notes that the LES set of equations (here: 2.12-2.15) is formally very similar to the one of RANS models. Both filter the (Boussinesq-approximated) Navier-Stokes equations. The main difference lies in the averaging procedure and thus in the meaning of τ. Whereas RANS models apply a temporal Reynolds average over a large scale compared to the characteristic scale of temporal fluctuations, LES models apply a spatial filter over quite a small scale compared to the characteristic length scales. So the RANS Reynolds stress tensor τ_{RANS} expresses the momentum flux of all turbulent fluctuations, and the

entire spectrum of turbulence must be modelled. The LES subgrid-scale stress tensor τ_{LES}, however, expresses the resolved-scale effect of the momentum flux due to small, subgrid-scale turbulence only, and only these small scales must be modelled. Another difference becomes obvious in the limit of vanishing grid length Δ. Since $\lim_{\Delta \to 0} \tau_{\text{LES}} = 0$, LES gradually becomes DNS, however, $\lim_{\Delta \to 0} \tau_{\text{RANS}}$ does not exist.

Sagaut (2006, chapter 1.5) notes that LES results are not only controlled by the filter that is applied to the Navier-Stokes equations described above. They are also influenced by approximation errors that are inherent e.g. in the numerical schemes and the turbulence closure model both of which yield additional, largely unknown filter effects. The spatial filtering in LES is believed to imply time filtering, but this has not been studied well yet (Sagaut, 2006, chapter 8.3.5).

2.2 Numerical modelling

2.2.1 Discretization

PALM is a finite difference model. Differential operators are approximated by finite differences ($\partial x_i \approx \Delta x_i$, $\partial t \approx \Delta t$). PALM stores variables on the staggered grid of the marker-and-cell method proposed by Harlow and Welch (1965) known as Arakawa C grid (Arakawa and Lamb, 1977) in meteorological literature (Fröhlich, 2006, p. 82). The staggered grid increases the effective spatial model resolution by a factor of two compared to a conventional non-staggered grid (Pielke, 2002) because second-order approximation of spatial derivatives can be achieved over only one grid length. In PALM, horizontal/vertical velocities are staggered by half a negative/positive grid length in their respective direction compared to scalar variables.

The main contribution of this study to the source code development of PALM is the ability to explicitly resolve solid obstacles within the threedimensional model domain. Previous versions of PALM could only represent inhomogeneities as ground surface inhomogeneities: gradual or sudden changes in ground surface properties such as heat or humidity fluxes, temperature, humidity or roughness length (Raasch and Harbusch, 2001; Weinbrecht and Raasch, 2001; Letzel and Raasch, 2003; Kim et al., 2004; Gryschka and Raasch, 2005; Raabe et al., 2005; Schröter et al., 2005; Inagaki et al., 2006; Steinfeld et al., 2007). The mask method (Briscolini and Santangelo, 1989) used by Kanda et al. (2004) to explicitly resolve solid obstacles on a rectangular grid was chosen as the basis for the obstacle code in PALM. The mask method belongs to the class of immersed boundary methods (Mittal and Iaccarino, 2005) that allow viscous flow simulation on Cartesian grids that do not conform to the geometry of the boundaries.

The concept of the original mask method (Briscolini and Santangelo, 1989) uses 3D flag data at each grid point to mask obstacles and their faces. A numerical model based on the original mask method would execute its full code at all grid points, regardless of whether a grid point is adjacent to an obstacle face, in the free fluid or within an obstacle. After each time step at each grid point non-applicable parts of the code (e.g. wall functions for grid points without adjacent walls) would be multiplied by zero based on the local flag data. This concept does have its merits: its ease of programming, especially for moving obstacles (e.g. traffic or moving buildings due to earthquakes or wind load) and a good vectorization.

A substantially simplified and optimized version of the mask method was developed for application of PALM to the urban boundary layer. This purpose does not require all features of the mask method. The feature to exactly represent obstacles of *arbitrary* shape and position is not maintained here, for a) many fundamental urban LES research applications including those of chapters 3 and 4 do not require this feature, and b) the exclusion of this

feature helps to optimize and speed up the code. Starting from PALM version 3.0, cubical obstacles can be represented directly if they match the numerical grid, otherwise obstacles must be approximated to fit the grid. As a further simplification in the present version, only bottom surface-mounted obstacles are permitted, and holes or overhanging structures are not included, which allows further code optimization, because in effect it reduces the 3D obstacle dimension to a 2D topography. One may argue that this is an oversimplification in view of complex urban building geometries, however, this format actually directly conforms to the Digital Elevation Model (DEM) format. DEMs of city morphologies are becoming increasingly available worldwide recently due to advances in sensing technologies such as laser scanning or lidar (Ratti et al., 2006) (see also chapters 5 and 6). As long as PALM uses such 2D urban input data, there is no point to provide the full 3D obstacle dimension, especially when using a 3D obstacle code structure would bring about a sacrifice in performance.

These simplifications allowed to adopt the masking concept to the special needs of PALM to further optimize performance on both vector and parallel machines. In PALM, 2D topography height data suffice to mask obstacles and their faces. These data are fixed in time, since moving obstacles are not considered. This means that after the 2D topography height data are discretized according to the horizontal grid, they can be directly integrated into PALM's loop structure as lower vertical index for all integration loops. Actually, PALM uses *two* 2D height index arrays, e.g. for scalars `nzb_s_inner` and `nzb_s_outer`, to separate the domain into three regions:

region A   `k > nzb_s_outer`, grid points in free fluid without adjacent walls, where only standard PALM code is executed,

region B   `nzb_s_inner < k ≤ nzb_s_outer`, grid points next to walls that require extra code (e.g. wall functions), and

region C   `0 ≤ k ≤ nzb_s_inner`, grid points within obstacles excluded from calculation.

One benefit of this division is that the additional topography code (can be computationally expensive) is only executed in region B where it is actually required; thus it minimizes the extra computational load. Figure 2.1 contrasts the conceptual difference in obstacle masking and code execution between the original mask method approach and the modifications in PALM.

Figure 2.2 shows that the obstacles faces are located where the respective wall normal velocity components u, v, and w are defined so that the impermeability boundary condition can be implemented easily. Since u, v, and w each are defined on their own staggered grid, compared to the one of central scalars such as p and θ, three extra pairs `nzb_u|v|w_inner|outer(j,i)` of 2D height index arrays exist as shown in Figure 2.3. The indices i, j, k here refer to the position of a grid cell in the discretized 3D model domain, their counterparts i_u, j_v, k_w refer to the respective staggered grids of u, v, and w. (Many publications do not introduce own indices for the staggered grids. There, $i_u = i - 0.5$, $j_v = j - 0.5$ and $k_w = k + 0.5$ would replace PALM notation.)

2.2.2 Numerical schemes

PALM simulations with obstacles use the default advection scheme by Piacsek and Williams (1970, form C3) because, as a second-order scheme, it allows an effective local implementation of boundary conditions for mask method (cf. section 2.4). Alternatives for standard non-obstacle simulations are the Upstream-Spline scheme (Price and MacPherson, 1973;
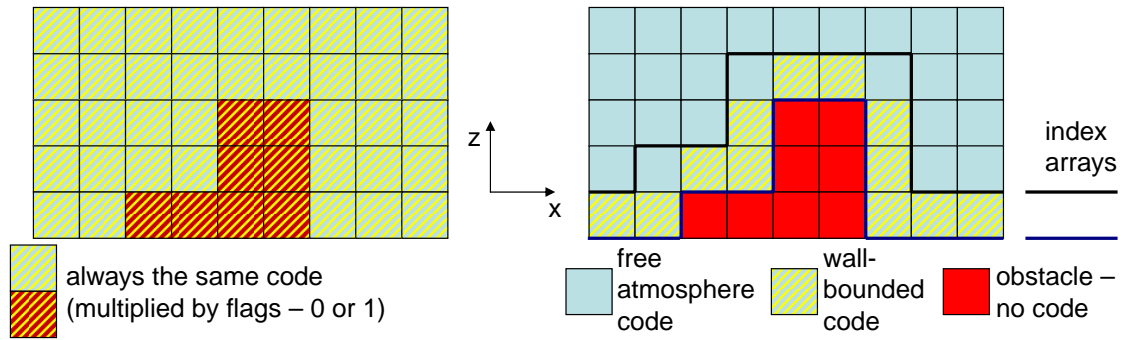
Figure 2.1: 3D masking concept of the original mask method (left) versus the 2D version in PALM (right).
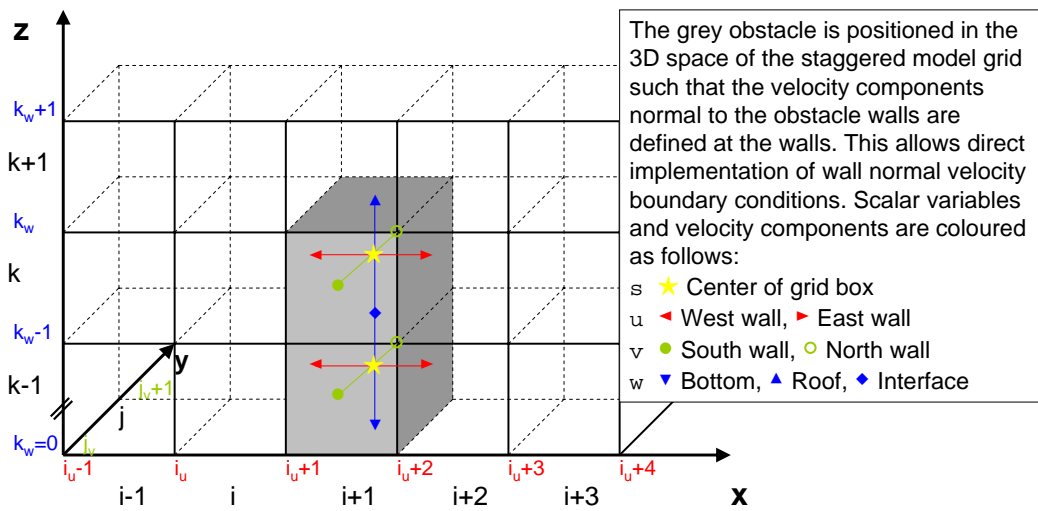
Figure 2.2: Obstacle position on the staggered grid in 3D space.
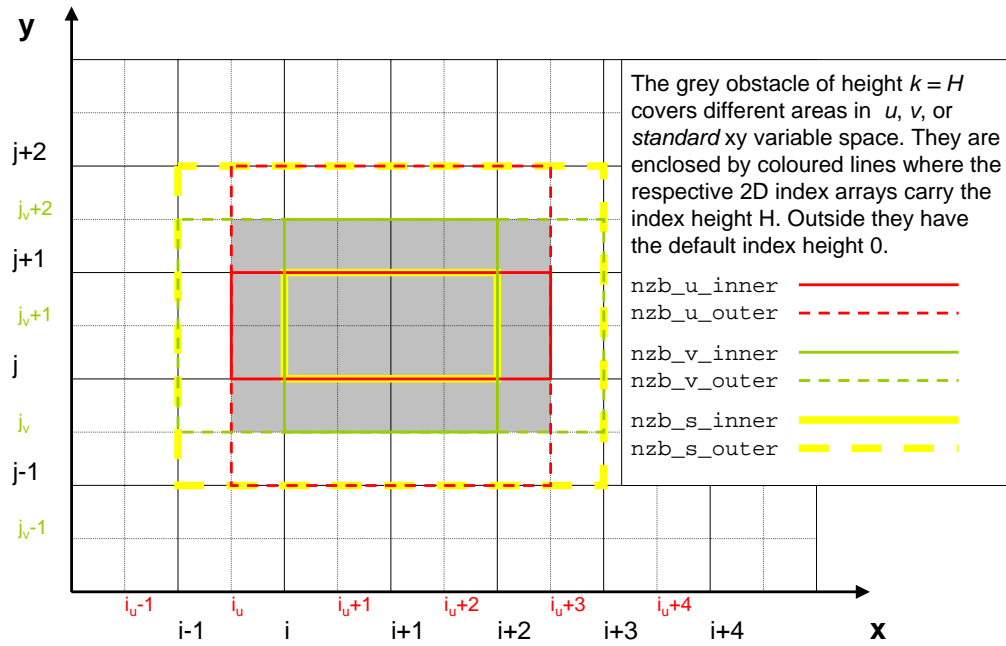
(a) In xy space.
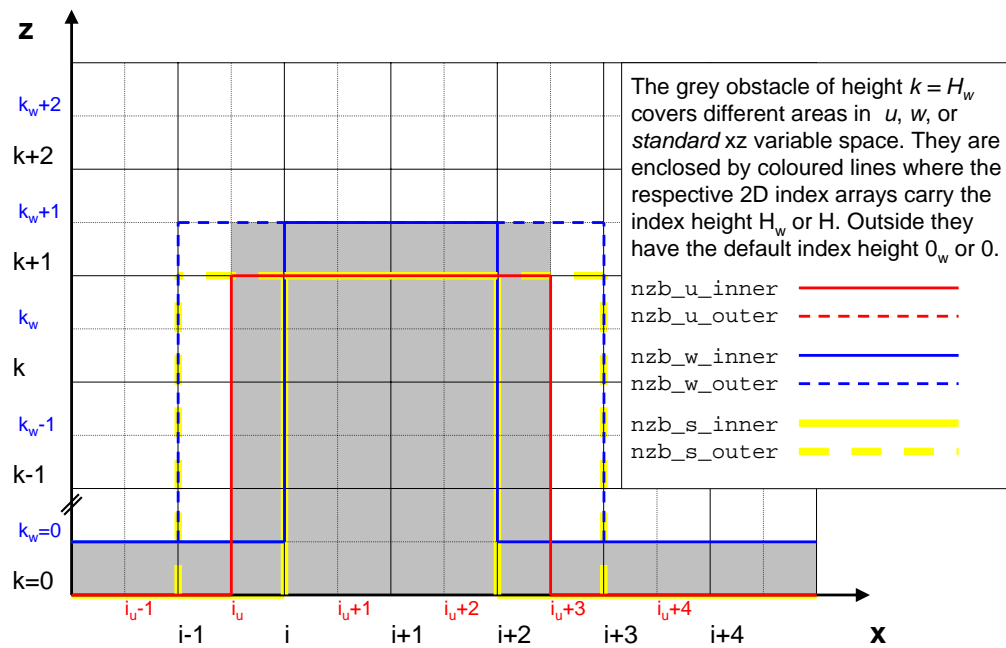
(b) In xz space.

Figure 2.3: Arrangement of 2D obstacle height index arrays.

Mahrer and Pielke, 1978) and the monotone Bott-Chlond scheme (Chlond, 1994, only scalar advection). It is well-established that second-order advection schemes produce artificial $2\,\Delta x_i$ oscillations upstream of solid walls because they cannot handle sharp gradients very well (e.g. LeVeque, 1992, Ferziger and Perić, 2002). Using the 1D nonlinear Burgers (1948) equation as a simple example, Letzel (1999) showed that the Piacsek and Williams (1970) scheme used in PALM performs better than the standard Lagrangian second-order advection but still yields a considerable amount of upstream oscillations. Although their amplitude reduces with grid refinement, they are still present in the high-resolution PALM simulations (this is visible for example in Fig. 4.6 on page 48). For the purpose of this study the Piacsek and Williams (1970) scheme produces satisfactory results, however, a better advection scheme may be required for future applications.

This study uses PALM's default 3rd-order Runge-Kutta time integration scheme that was implemented by Jansen (2004). Alternatives are Euler or leap-frog time differencing, the latter with a weak Asselin (1972) time filter to remove the computational mode.

PALM's optional cloud physics mode with evaporation, condensation and precipitation processes (Schröter, 2003, chapter 2.2.4) that was introduced with PALM version 2.0 is not used in this study. PALM uses a constant density $\rho_0 \equiv 1\ \text{kg m}^{-3}$.

2.2.3 The fractional step method

The Boussinesq equations (2.12)-(2.15) on page 9 require incompressibility, but since the time integration of (2.12) does not take into account the continuity equation (2.13), it inherently produces divergences in the flow field. These divergences can be eliminated by the fractional step method (cf. Breuer (2002, chapter 5.3.2), Ferziger and Perić (2002, chapters 6.2 and 7.3-7.6) or Fröhlich (2006, chapter 4.4.1)).

PALM uses the fractional step method[1] that was introduced by Chorin (1968, 1969) and Temam (1969) with the modifications of Patrinos and Kistler (1977) and Kim and Moin (1985). The essence of this method is a) to exclude the pressure term $-\rho_0^{-1}\partial_{x_i}\overline{p^*}$ from (2.12) during time integration, which yields only a provisional velocity $\overline{u}_{i,\text{prov}}^{t+\Delta t}$, b) to decompose

$$\overline{u}_i^{t+\Delta t} = \overline{u}_{i,\text{prov}}^{t+\Delta t} - \frac{r\Delta t}{\rho_0}\frac{\partial \overline{p^*}^t}{\partial x_i} \quad , \tag{2.16}$$

and c) to demand incompressibility of $\overline{u}_i^{t+\Delta t}$ by inserting (2.16) into (2.13)

$$\frac{\partial}{\partial x_i}\overline{u}_i^{t+\Delta t} = \frac{\partial}{\partial x_i}\left(\overline{u}_{i,\text{prov}}^{t+\Delta t} - \frac{r\Delta t}{\rho_0}\frac{\partial \overline{p^*}^t}{\partial x_i}\right) \overset{!}{=} 0 \quad . \tag{2.17}$$

The factor r depends on the time integration scheme. This process yields a Poisson equation for the perturbation pressure $\overline{p^*}^t$

$$\frac{\partial^2 \overline{p^*}^t}{\partial x_i^2} = \frac{\rho_0}{r\Delta t}\frac{\partial \overline{u}_{i,\text{prov}}^{t+\Delta t}}{\partial x_i} \tag{2.18}$$

whose exact solution $\overline{p^*}^t$ would carry all the divergence of $\overline{u}_{i,\text{prov}}^{t+\Delta t}$, so that $\overline{u}_i^{t+\Delta t}$ would be free of divergence. In practice, a divergence reduction by several orders of magnitude is considered sufficient.

---

[1]For leap-frog time integration the fractional step method reduces to a two-level predictor-corrector method.

In PALM, three Poisson solvers are available: iterative SOR, multigrid or FFT. The latter applies the direct method by Schumann and Sweet (1988) to Fourier transform the Poisson equation in both horizontal directions and to solve the resulting tridiagonal matrix for the transformed pressure which is then re-transformed (Raasch and Schröter, 2001). The combination of the mask method with 2nd-order spatial finite differences and explicit time integration poses no problem here provided correct boundary conditions are set (Kawamura, 1996, chapter 6.3.1)[2]. The FFT solver of PALM was adopted in the LES-CITY code of Kanda et al. (2004) and subsequently re-adopted in the obstacle code of PALM.

2.3 Subgrid-scale modelling

2.3.1 Turbulence closure

Turbulence closure is one main challenge, if not *the* challenge in LES (and RANS) modelling. Numerous reviews treat this subject, for example Meneveau and Katz (2000), Breuer (2002, chapter 3.3), Fröhlich (2006, chapter 6), and Sagaut (2006, chapters 5-7), to name but a few.

The second-order moments $\tau_{ki} = \overline{u_k'' u_i''}$, $\overline{u_k'' \theta''}$ and $\overline{u_k'' s''}$ in the Boussinesq equations (2.12), (2.14) and (2.15) on page 9 contain unknown subgrid-scale fluctuations and need to be parameterized in terms of resolved-scale quantities to close the equations. PALM uses a modified version of the Smagorinsky (1963) model, the flux-gradient relationships of the 1½th order Deardorff (1980) scheme

$$\overline{u_k'' u_i''} = -K_m \left(\frac{\partial \overline{u}_i}{\partial x_k} + \frac{\partial \overline{u}_k}{\partial x_i} \right) \tag{2.19}$$

$$\overline{u_k'' \theta''} = -K_h \frac{\partial \overline{\theta}}{\partial x_k} \tag{2.20}$$

$$\overline{u_k'' s''} = -K_s \frac{\partial \overline{s}}{\partial x_k} \quad . \tag{2.21}$$

The turbulent diffusion coefficients for momentum and heat, K_m and $K_h \ (= K_s)$, are parameterized by the subgrid-scale turbulent kinetic energy (SGS-TKE), $\overline{e} = \frac{1}{2} \overline{u_i'' u_i''}$,

$$K_m = c_m l \sqrt{\overline{e}} \tag{2.22}$$

$$K_h = \left(1 + \frac{2l}{\Delta} \right) K_m \quad , \tag{2.23}$$

with the Smagorinsky constant $c_m = 0.1$, the mixing length l and the characteristic grid length $\Delta = \sqrt[3]{\Delta x \cdot \Delta y \cdot \Delta z}$. The mixing length l is

$$l = \begin{cases} \min \left(\Delta, \ 0.7 \, d, \ 0.76 \sqrt{\overline{e}} \left(\frac{g}{\theta_0} \frac{\partial \overline{\theta}}{\partial z} \right)^{-\frac{1}{2}} \right) & \text{stable stratification,} \\ \min \left(\Delta, \ 0.7 \, d \right) & \text{otherwise.} \end{cases} \tag{2.24}$$

d is the normal distance to the nearest solid surface (bottom, obstacle wall or rooftop). The last remaining unknown is the SGS-TKE $\overline{e}$ itself that requires an additional prognostic equation (using the notation of Stull, 1988, chapter 5) with further parameterizations

$$\frac{\partial \overline{e}}{\partial t} = -\frac{\partial}{\partial x_j} \overline{u}_j \overline{e} - \tau_{ij} \frac{\partial \overline{u}_i}{\partial x_j} + \frac{g}{\theta_0} \overline{u_3'' \theta_j''} - \frac{\partial}{\partial x_j} \left\{ \overline{u_j'' \left(e + \frac{p''}{\rho_0} \right)} \right\} - \epsilon \tag{2.25}$$

---

[2]Kanda (2004) is acknowledged for pointing out this reference.

$$\overline{u_j'' \left(e + \frac{p''}{\rho_0} \right)} = -2 \, K_m \, \frac{\partial \overline{e}}{\partial x_j} \tag{2.26}$$

$$\epsilon = \left(0.19 + 0.74 \frac{l}{\Delta} \right) \cdot \frac{\overline{e}^{\frac{3}{2}}}{l} \quad . \tag{2.27}$$

The calculation of SGS-TKE dissipation rate ϵ here follows Moeng and Wyngaard (1988).

2.3.2 Wall modelling

The treatment of solid walls is another difficult task especially in LES modelling, because near walls the dominant scale of energy-containing eddies reduces drastically. Again numerous reviews exist, e.g. Piomelli and Balaras (2002)[3], Breuer (2002, chapter 3.5.2), Fröhlich (2006, chapter 8) and Sagaut (2006, chapter 10.2). The two fundamental approaches are

1. local grid refinement near walls (wall-resolving LES) and

2. modelling of wall effects (LES with wall functions).

Approach 1 seems intuitive following the original LES idea, however, a well-resolved LES (Cabot and Moin, 1999) requires not only a fine wall-normal resolution but also grid refinement in the wall-parallel directions. The corresponding time step reduction makes this approach computationally expensive.

PALM follows approach 2 and assumes a Prandtl-layer at each wall surface. The similarity theory introduced by Monin and Obukhov (1954, MOST) provides the wall functions (e.g. Sorbjan (1986, 1989, chapter 4.2), Foken (2006), Garratt (1992, chapter 3.3) and Etling (2002, chapters 21.1-21.6)). This has the advantage that rough wall and stratification effects, that are both typical of atmospheric flows, are accounted for.

Wall surfaces in PALM can be horizontal (bottom surface or rooftop, facing upwards) or vertical (facing N, E, S or W). At horizontal surfaces, PALM allows a) to specify the surface values (θ, s) or b) to prescribe their surface fluxes; at vertical surfaces, b) is currently the only choice. In case a) the respective surface fluxes are calculated from MOST. Momentum surface fluxes are always calculated from MOST. In this study, all surface fluxes are directly prescribed; hence the following description of MOST in PALM covers only momentum fluxes.

Let Δ_p be the local Prandtl layer thickness (half the wall normal grid length), $v_{\text{tangential}}$ the tangential velocity, i.e. the absolute velocity in the nearest parallel plane (at distance Δ_p from the wall), and v_{normal} the wall normal velocity. Then the wall normal momentum flux can be expressed as $\tau_{\text{normal}} = -u_*^2$ with the wall friction velocity u_* obtained from integration of the Dyer-Businger functions (Businger et al., 1971),

$$u_* = \begin{cases} \dfrac{\kappa \, v_{\text{tangential}}}{\ln \left(\dfrac{\Delta_p}{z_{0,\text{loc}}} \right) + 5 \, Rif \, \dfrac{\Delta_p - z_{0,\text{loc}}}{\Delta_p}} & \text{stable \& neutral stratification,} \\[2em] \dfrac{\kappa \, v_{\text{tangential}}}{\ln \left(\dfrac{1+h_2}{1-h_2} \cdot \dfrac{1-h_1}{1+h_1} \right) + 2 \left(\arctan(h_2) - \arctan(h_1) \right)} & \text{otherwise,} \end{cases} \tag{2.28}$$

$$h_1 = (1 - 16 \, Rif)^{-\frac{1}{4}} \,, \qquad h_2 = \left(1 - 16 \, Rif \, \frac{z_{0,\text{loc}}}{\Delta_p} \right)^{-\frac{1}{4}} \,, \tag{2.29}$$

---

[3]The review of Piomelli and Balaras (2002) is of limited use in the context of this study because they (i) do not consider stratification effects and (ii) give only a brief treatment of geophysical/meteorological flows.

where $\kappa = 0.4$ is the von Kármán constant, $z_{0,\text{loc}}$ the local wall roughness length, and the (neutral) Richardson flux number is

$$Rif = \frac{\Delta_p}{L} = -\frac{\kappa\, g\, \overline{w''\theta''}_0}{\overline{\theta}_0\, u_*^3}\, \Delta_p \quad . \qquad (2.30)$$

L is the Obukhov length, $\overline{w''\theta''}_0$ is the subgrid-scale LES turbulent heat flux, and the subscript $_0$ refers to the adjacent grid box. The interdependence of equations (2.28) and (2.30) formally requires an iterative solution. In practice, Rif from the preceding time step is considered to be a sufficient approximation.

According to Cai (2006), no concensus has been obtained yet how to model rough vertical wall effects for non-neutral thermal stratification. For example, Cai (2006) uses an extension of the Louis scheme as thermal boundary condition for urban vertical walls (Uno et al., 1995; Louis, 1979). Wall functions for turbulent natural convection at (smooth) vertical walls from the engineering community may be another alternative (Cai, 2006). The present study applies MOST, which was originally developed only for a horizontally homogeneous boundary layer, to all local walls. In the urban context, i.e. for rough vertical walls, these attempts including MOST are still awaiting validation. The validation of PALM obstacle code in chapter 3 is confined to the neutral boundary layer. It should be treated and interpreted carefully in simulations with non-neutral thermal stratification.

2.4 Supergrid-scale modelling

By analogy with the subgrid-scale in the previous section 2.3, the topics of the following subsections can be summarized as super-grid scale modelling. This is because they refer to scales that are beyond or related to the discretized model domain (Fröhlich, 2006, p. 201): boundary conditions, initial conditions and driving modes. The different simulations performed for this study each require a distinct set-up, e.g. for free stream or channel flow.

2.4.1 Boundary conditions

Cyclic *lateral boundary* conditions are chosen for this study, which yields an infinite, periodically repeating horizontal model domain.

At the *top boundary*, the set of boundary conditions depends on the chosen set-up. Free stream flow requires Neumann boundary conditions for the horizontal velocity components: $\partial_z \overline{u}|_{z_{\text{top}}} = \text{const}$ and $\partial_z \overline{v}|_{z_{\text{top}}} = \text{const}$; channel flow has $\overline{u}$ and $\overline{v}$ set to the speed of the top plate (Diriclet). Vertical velocity and perturbation pressure are always kept zero (Diriclet); SGS-TKE $\overline{e}$ and potential temperature $\overline{\theta}$ currently always obey a Neumann boundary condition.

The description of the *bottom boundary* (horizontal surfaces, where $\overline{w}$ is defined but $\overline{u}$ and $\overline{v}$ are not) is analogous to vertical obstacle walls. The Diriclet boundary condition applies to the vertical velocity: $\overline{w}(z=0) = 0$. Static friction (no-slip) demands also $\overline{u}$ and $\overline{v}$ to vanish at the surface. On the staggered grid, where $\overline{u}(z)$ and $\overline{v}(z)$ are defined at $z = \pm\frac{\Delta z}{2}$, this is realized by a mirror boundary condition: $\overline{u}(-\frac{\Delta z}{2}) = -\overline{u}(+\frac{\Delta z}{2})$ and $\overline{v}(-\frac{\Delta z}{2}) = -\overline{v}(+\frac{\Delta z}{2})$. SGS-TKE $\overline{e}$, potential temperature $\overline{\theta}$ and perturbation pressure p^* obey a Neumann boundary condition: $\overline{e}(-\frac{\Delta z}{2}) = \overline{e}(+\frac{\Delta z}{2})$, $\overline{\theta}(-\frac{\Delta z}{2}) = \overline{\theta}(+\frac{\Delta z}{2})$ and $p^*(-\frac{\Delta z}{2}) = p^*(+\frac{\Delta z}{2})$. Wherever possible, PALM avoids explicit setting of these boundary conditions at vertical walls for performance reasons and sets them indirectly e.g. by multiplication with wall-normal velocity components (zero) or through the loop structure.

2.4.2 Initial conditions and driving modes

By default, PALM simulates the atmospheric boundary layer with Coriolis force driven by the geostrophic wind. This study uses alternative sets of initial conditions and driving modes suited to the problems studied. For example, a direct body force has been added to the code in form of a constant external horizontal pressure gradient, which gives an additional term $D_i = -\rho_0^{-1}\partial_{x_i}p_{\text{ext}}$ for $i \in [1,2]$ on the right-hand-side of equation (2.12). This is useful to drive the flow (to balance surface friction) when simulating wind tunnel or other experiments without Coriolis effect. Fröhlich (2006, chapter 7.2.2) states a variable body force to ensure mass flux conservation as an alternative method. This method reduces to volume flow conservation in PALM ($\rho = \text{const}$); it has also been implemented.

Initial conditions often serve the purpose of initializing the model close to its (quasi-)steady state to save computation time. PALM's 1D model serves this purpose for simulations with neutral stratification and geostrophic wind (Coriolis effect). Based on the analytical solution of Poisseuille flow (Etling, 2002, chapter 18.3), an initialization for directly driven flows without Coriolis effect was implemented. It prescribes the vertical profile of horizontal wind

$$\overline{u}_i(z) = \overline{u}_i(z_{\text{ref}}) + \frac{D_i}{2\,\widetilde{K_m}}\,(z - z_{\text{ref}})\,\Big(n\,(z_{\text{top}} - z_{\text{ref}}) - (z - z_{\text{ref}})\Big) \qquad (2.31)$$

for $i \in [1,2]$. z_{top} is the height of the model domain, z_{ref} is a reference height, the parameter n is equal to 1 for channel flow and equal to 2 for free stream flow. *A priori* information is required to specify the value of the turbulent diffusion coefficient $\widetilde{K_m}$; for example, it can be inferred from a previous simulation or from a set of values $\overline{u}_i(z_{\text{ref}})$ and $\overline{u}_i(z) \neq \overline{u}_i(z_{\text{ref}})$.

2.5 Parallelization and performance

The Fortran 95 programming of the equations and numerical schemes discussed so far in this chapter requires special care to make full use of available computational resources. Common architectures of today's supercomputers include parallel clusters of scalar or vector processors interconnected by a network whose performance is always a bottleneck. The subject of *high-performance computing* deals with the techniques to optimize code performance on such architectures (cf. the detailed introduction to HPC by Breuer, 2002, chapter 6). The key strategies in PALM are *single processor optimization* for different processor architectures (e.g. cache-based systems like IBM-Regatta, or vector architectures like NEC-SX) and *parallelization*. Parallelization in PALM uses the Message Passing Interface (MPI, Gropp et al., 1999) with a one- or two-dimensional horizontal domain decomposition or OpenMP[4]. Since these optimization strategies and the good performance of PALM are well documented, e.g. by Raasch and Schröter (2001), Ketelsen (2002) and Schröter (2003), they are not discussed here further.

The implementation of the obstacle code causes no additional non-local data dependencies that would affect parallelization performance, and, thanks to its special loop steering, it avoids `IF`-structures within loops that would affect vectorization. Performance tests of a single building simulation (not shown) have shown that the obstacle code parallelizes well.

---

[4]Specifications are avaibable at `http://www.openmp.org`.

3 Validation

One of the goals of this research project was to surpass the accuracy of existing LES models by using an unprecedented, fine grid resolution in urban PALM simulations. For validation of the obstacle code a large LES (and RANS) model intercomparison based on a well documented wind tunnel reference experiment was chosen, that also allows a comparison of accuracy among the LES codes.

Martinuzzi (1992) and Martinuzzi and Tropea (1993) investigated the fully turbulent flow around a single surface-mounted cube in a shallow wind tunnel of double cube height. Their measurement data are available from the reference database of the European Research Community on Flow, Turbulence and Combustion (ERCOFTAC, `www.ercoftac.org`). This experiment served as reference for test case B2 of the 1995 "Workshop on Large Eddy Simulation of Flows past Bluff Bodies" in Rottach-Egern, Germany (Rodi et al., 1995) that forms the basis of the validation of the obstacle code of PALM.

A single cubical obstacle in fully developed turbulent neutral channel flow is well suited for CFD model validation because despite of the simple geometry the flow is complex, with multiple separation lines and vortices, and fully three-dimensional, even in the time-average. A detailed synopsis of both the wind tunnel experiment and the LES & RANS intercomparison is given by Breuer (2002, chapter 7.2) who draws together material from a number of earlier publications (including Breuer et al., 1996; Lakehal and Rodi, 1997; Martinuzzi, 1992; Martinuzzi and Tropea, 1993; Rodi et al., 1995; Rodi, 1997; Rodi et al., 1997; Rodi, 1998; Shah and Ferziger, 1997). Recently, Krajnović and Davidson (2002) and Tseng et al. (2006) also validated their respective urban LES codes using this reference experiment.

Section 3.1 describes the set-up of the validation experiment. Validation starts with a more qualitative comparison of the time-mean flow topology in section 3.2, followed by a quantitative comparison of turbulence statistics in section 3.3. Based on the validation results section 3.4 gives resolution recommendations for urban PALM simulations.

3.1 Set-up

Figure 3.1 shows the geometry of the LES and RANS intercomparison experiment whose coordinate notation is adopted in this chapter so that y is the vertical and z the spanwise coordinate. The wind tunnel experiment used a cube of height $H = 25$ mm in a channel of height $h = 2\,H$, upstream length $x_1 = 52\,h$, downstream length $x_2 = 26\,h$ and spanwise width $b = 12\,h$. Turbulence was artificially generated at the inlet to obtain fully developed turbulent channel flow at least $5\,h$ upstream of the cube. The Reynolds number was

$$Re_H = \frac{u_b\,H}{\nu_m} = 40\,000 \tag{3.1}$$

based on the inflow bulk velocity u_b and the cube height H.

For the numerical simulations Rodi et al. (1995) recommend a horizontally reduced computational domain with $h = 2\,H$, $x_1 = 3\,H$, $x_2 \geq 6\,H$ and $b = 7\,H$ to save computational resources, a) assuming the channel side walls had a negligible influence on the cube flow in the wind tunnel, and b) requiring the models to provide a fully developed turbulent inflow.
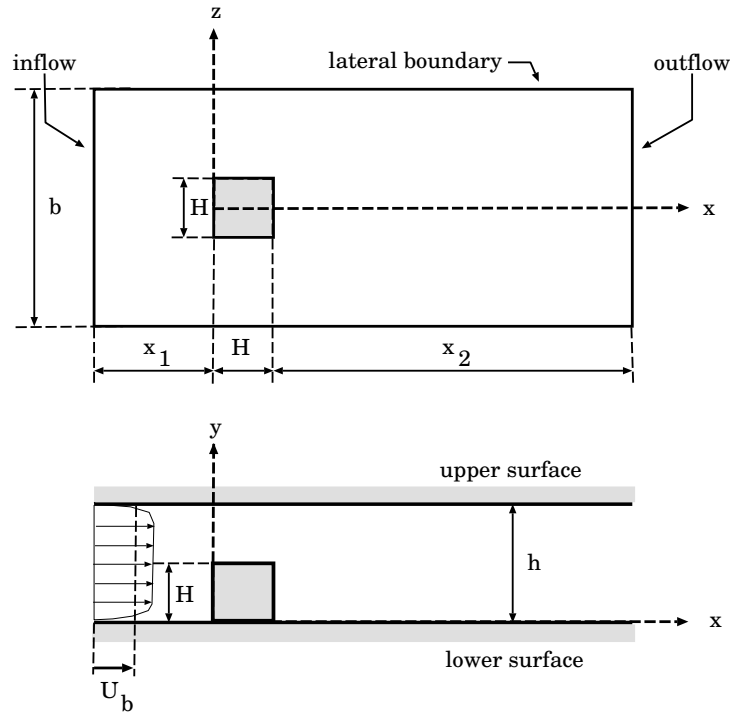
Figure 3.1: Geometry of the LES and RANS intercomparison experiment (reprinted with kind permission from Rodi et al., 1995). Note that this figure is not drawn to scale.

For a) free-slip or periodic boundary conditions were recommended in spanwise direction, for b) inflow-outflow boundary conditions in streamwise direction. A choice of no-slip boundary conditions or wall functions is offered for all solid walls. Simulations were requested for cases B1 with $Re_H = 3\,000$ and B2 with $Re_H = 40\,000$.

This set-up was transferred to scales that are more typical of the urban atmosphere with $H = 50\,\mathrm{m}$ and $u_b = 1\,\mathrm{m\ s^{-1}}$. The resulting larger Reynolds number $Re_H = 3.3 \cdot 10^6$ poses no principal problem for the validation since the flow is in the fully turbulent regime in all three cases and the computational differences between B1 and B2 were found to be very small (Rodi et al., 1997). The "urban cube" was assigned an urban roughness of $z_{0,\mathrm{loc}} = 0.1\,\mathrm{m}$ at all faces.

PALM does not offer a solid wall boundary condition at the top boundary. This validation is a shallow channel flow, therefore a simple no-slip wall boundary condition at the domain top was added as an ad-hoc solution for this validation. Contrary to the bottom surface and obstacle walls, however, no wall functions were implemented at the top wall where friction is thus underestimated. The channel top wall is thus underresolved, which does locally affect the flow as will be shown in the following sections.

Contrary to the above recommendations (and contrary to the sketch in Fig. 3.1) PALM uses periodic boundary conditions in both horizontal directions because this was the only choice at the time when the simulations were performed. The flow is directly driven (without Coriolis force) by a constant external pressure gradient (see subsection 2.4.2). The flow reaches an approximately constant bulk velocity u_b once the governing forces (pressure gradient and friction) are in balance. Here, the pressure gradient is set to $D_1 = -\partial_x p_{\mathrm{ext}} = 0.00016\,\mathrm{Pa\ m^{-1}}$; this value was determined empirically to obtain the desired bulk velocity $u_b \approx 1\,\mathrm{m\ s^{-1}}$. The simulation is initialized according to equation (2.31) on page 18 with $u(0) = 0.6\,\mathrm{m\ s^{-1}}$, $u(H) = 1.15\,\mathrm{m\ s^{-1}}$ and $n = 1$.

Since the flow is fully 3D, time-averaging is the only way to produce reliable statistics. The workshop submissions for case B2 considered here were averaged over

$$T_{\text{averaging}}^* = \frac{T_{\text{averaging}} \cdot u_b}{H} = 100 \sim 700 \qquad (3.2)$$

dimensionless timesteps. $T_{\text{averaging}}^* = 10$ used in a further submission (IIS-KOBA) was found insufficient. A parameter study with PALM (not shown) that repeatedly doubled the averaging time starting from $T_{\text{averaging}} = 1\,\text{h}$ found an optimal value of $T_{\text{averaging}} = 8\,\text{h}$, i.e. $T_{\text{averaging}}^* = 576$ based on a symmetry criterion. Of course, the symmetry about the central vertical axis ($\frac{z}{H} = 0$) could be used for ensemble averaging, but this is not very useful because a) it would only slightly improve statistics, and b) the symmetry criterion could then no longer be used to determine the averaging time (Breuer, 2002).

The synopsis of case B2 given by Breuer (2002, chapter 7.2) includes three own LES contributions (LES3-LES5) and one LES contribution by H. Wengle, University of the Federal Armed Forces Munich (UBWM2). These models are finite volume codes with non-uniform grids and centered second-order discretization of spatial derivatives. It further includes four RANS contributions by Breuer et al. (1996); Lakehal and Rodi (1997):

K-E   standard k-ϵ model after Launder and Spalding (1974) with wall function (Launder and Sharma, 1974),

RNG   renormalization group k-ϵ model after Yakhot et al. (1992),

KATO-L   Kato-Launder k-ϵ model after Kato and Launder (1993),

TWO-L   two layer k-ϵ model after Rodi (1991).

Tables 3.1, 3.2 and 3.3 list further details on the LES and RANS models including PALM simulations. All LES results presented in the following sections 3.2 and 3.3 are time-averaged over $T_{\text{averaging}}^*$ dimensionless time steps as listed in Table 3.1.

3.2 Time-mean flow topology

From wind tunnel flow visualization and measurements Martinuzzi (1992) devised the topology of time-averaged flow shown in Figure 3.2. (Based on LES, Wang and McNamara (2005) present 3D mean flow streamlines that resemble this topology quite well.) The flow approaches the cube from the left and separates in front of the cube, it is diverted partly over the cube and partly around it. The primary and secondary separation vortices are bent around the cube to form the horse-shoe vortex that owes its name to its typical shape with convergence followed by divergence further downstream. Flow separation occurs also at the front corners of the cube and produces the roof and side wall vortices. Downstream of the cube there is a large separation region with an average length of ca $1.6\,H$. Its integrated arch vortex just behind the cube is a dominant feature in the vertical cross-section of Figure 3.3 and also leaves two footprints (N_{14}) on the channel floor as is shown in Figure 3.4.

In Figure 3.3 only the primary separation vortex in front of the cube is visible close to the channel floor. The mean flow does not reattach on the roof. In Figure 3.4 the primary and secondary separation vortices (A, B) forming the horse-shoe vortex (D) are clearly visible.

---

[1]According to equation (2.24) on page 15.
[2]TWO-L makes use of the horizontal symmetry of the problem and simulates only one half of the domain.

Name	Grid	#GP	WR	TI	SGS model	WT	$T^*_{\text{averaging}}$
LES3	$165 \times 65 \times 97$	$1.0 \cdot 10^6$	0.0125	AB	Smagorinsky, VDD	WF	150
LES4	$165 \times 65 \times 97$	$1.0 \cdot 10^6$	0.0125	AB	Dynamic	WF	109
LES5	$165 \times 65 \times 97$	$1.0 \cdot 10^6$	0.0125	AB	Smagorinsky, VDD	NS	151
UBWM2	$144 \times 58 \times 88$	$6.3 \cdot 10^5$	0.02	LF	Smagorinsky	WF	650-700
PALM N10-N80	see Table 3.2			RK3	Deardorff, VDD[1]	WF	576

Table 3.1: Details of the LES models including PALM.
Abbreviations: #GP: number of grid points; WR: grid resolution at walls $\Delta_{\text{min, wall}}$ in units of H; TI: time integration scheme, AB: Adams-Bashforth, LF: Feap-frog, RK3: Runge-Kutta 3$^{\text{rd}}$ order; VDD: Van Driest (1956) damping; WT: wall treatment, WF: wall function, NS: no-slip.

Name	Grid	#GP	WR	CFR
N10	$192 \times 64 \times 20$	$2.5 \cdot 10^5$	0.1	10
N20	$384 \times 128 \times 40$	$2.0 \cdot 10^6$	0.05	20
N32	$640 \times 192 \times 64$	$7.9 \cdot 10^6$	0.03125	32
N40	$768 \times 256 \times 80$	$1.6 \cdot 10^7$	0.025	40
N50	$960 \times 320 \times 100$	$3.1 \cdot 10^7$	0.02	50
N64	$1280 \times 384 \times 128$	$6.3 \cdot 10^7$	0.015625	64
N80	$1536 \times 512 \times 160$	$1.3 \cdot 10^8$	0.0125	80

Table 3.2: Details of the resolution study with PALM. Abbreviations as in Table 3.1 plus CFR: cube face resolution in grid points.

Name	Grid	#GP	WR
K-E	$110 \times 32 \times 66$	$2.3 \cdot 10^5$	0.01
RNG	$110 \times 32 \times 66$	$2.3 \cdot 10^5$	0.01
KATO-L	$110 \times 32 \times 66$	$2.3 \cdot 10^5$	0.01
TWO-L[2]	$142 \times 84 \times 64$	$7.6 \cdot 10^5$	0.001

Table 3.3: Details of the RANS models. Abbreviations as in Table 3.1.
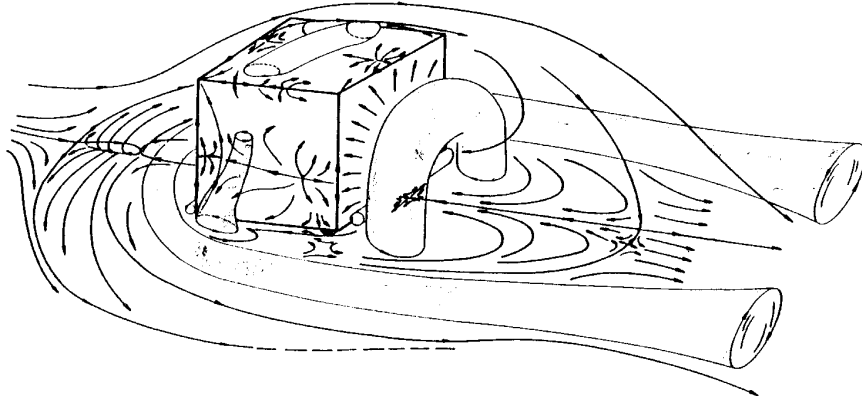
Figure 3.2: Topology of time-averaged flow (reprinted with kind permission from Martinuzzi, 1992 and Martinuzzi and Tropea, 1993).
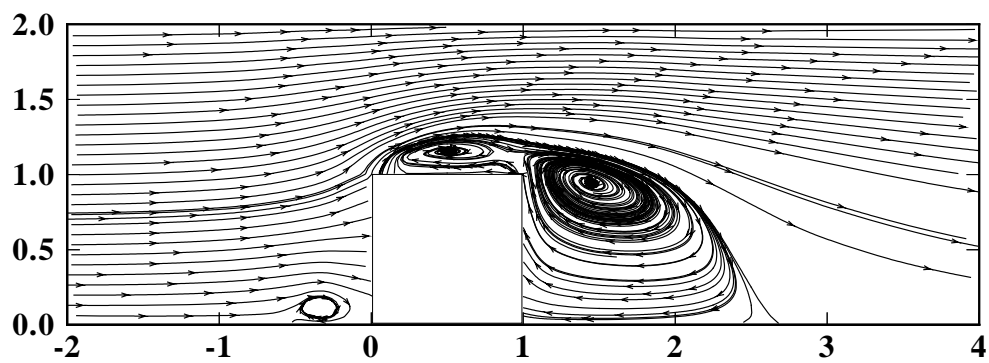
Figure 3.3: Reference experiment streamlines of time-averaged flow in the vertical symmetry plane $\left(\frac{z}{H} = 0\right.$, data of Martinuzzi, 1992, figure reprinted with kind permission from Rodi et al., 1995).

About $1.6\,H$ behind the cube the flow that is diverted over the cube reattaches on the channel floor (R).

Shah and Ferziger (1997) note that topology features such as the arch vortex and the horse-shoe vortex are in fact highly intermittent, they are symmetric only in the mean flow, but not instantaneously.

Figures 3.5 and 3.6 allow a qualitative comparison between LES, RANS models, PALM simulations and the wind tunnel reference experiment (Fig. 3.3) for the flow in the central vertical cross-section. The LES models including PALM capture all three main flow features well, the primary separation, the roof and the arch vortex. (Quantitative analysis of the recirculation length is provided further below.) The experimental uncertainty concerning the location of the primary separation vortex/head of the horse-shoe vortex is rather large, which makes a judgement difficult (Breuer, 2002). PALM reaches convergence with run N32; the lower resolution runs N10 and N20 do not (accurately) reproduce these vortices. The RANS models behave similar to the lowest PALM resolution run N10: the roof vortex is almost not or not at all reproduced, while the recirculation length is notably overestimated. Among the RANS models, RNG performs best for the recirculation length, TWO-L performs best for the roof vortex.

Figures 3.7 and 3.8 allow a similar qualitative comparison together with Fig. 3.4 for the horizontal flow near the channel floor. Although the LES models including PALM well reproduce all characteristic flow features (horse-shoe vortex, side vortices, recirculation zone with arch vortex footprints), there are differences especially concerning the ability of the models to produce the convergent part of the horse-shoe vortex that is upstream of labels "D" in Fig. 3.4.

Parameter studies such as LES3-5 and N10-80 – simulations that differ in only one parameter – allow to attribute these observations to these parameters. LES4 best represents the shape of the horse-shoe vortex as observed in the wind tunnel, which can easily be credited to its dynamic SGS model (Germano et al., 1991) since this is the only difference to the second best run, LES3, that uses the Smagorinsky (1963) model. LES5 is also based on LES3 with the only difference that wall functions have been replaced by a simple no-slip boundary condition. LES5, UBWM2 and the low resolution PALM runs N10 and N20 fail to produce the convergence of the horse-shoe vortex. The well-reproduced convergence in the higher resolution PALM runs N32-N80 appears to slightly intensify with resolution. Altogether three factors influencing the horse-shoe vortex in LES models thus can be identified: SGS model, wall functions and grid resolution.

Among the RANS models, only TWO-L is able to produce a qualitatively correct shape of the horse-shoe vortex, the other three a) produce the upstream flow separation too close to the cube and b) fail to produce any convergence downstream. All RANS models have a too long recirculation region.

As a first step towards a more quantitative analysis, Figure 3.9 defines characteristic length scales of flow separation and reattachment in the symmetry plane at the channel floor or at rooftop that are listed in Table 3.4.

Breuer (2002) notes that length X_{F1} a) is difficult to obtain numerically as well as experimentally and b) depends on the Reynolds number and should thus be interpreted with care. Within these bounds of uncertainty the LES models including PALM and the TWO-L RANS model relatively well agree with each other and the experimental value. The three other RANS models clearly underestimate X_{F1}, as could already be seen from the streamlines.

Neither the wind tunnel nor LES3-5 show a reattachment of the flow on the roof, but PALM and UBWM2 give X_T between 0.84 and 0.96. Breuer (2002) relates this to a poor grid resolution of UBWM2 at the wall ($\Delta_{\text{min, wall}} = 0.02$). It is not clear whether the same
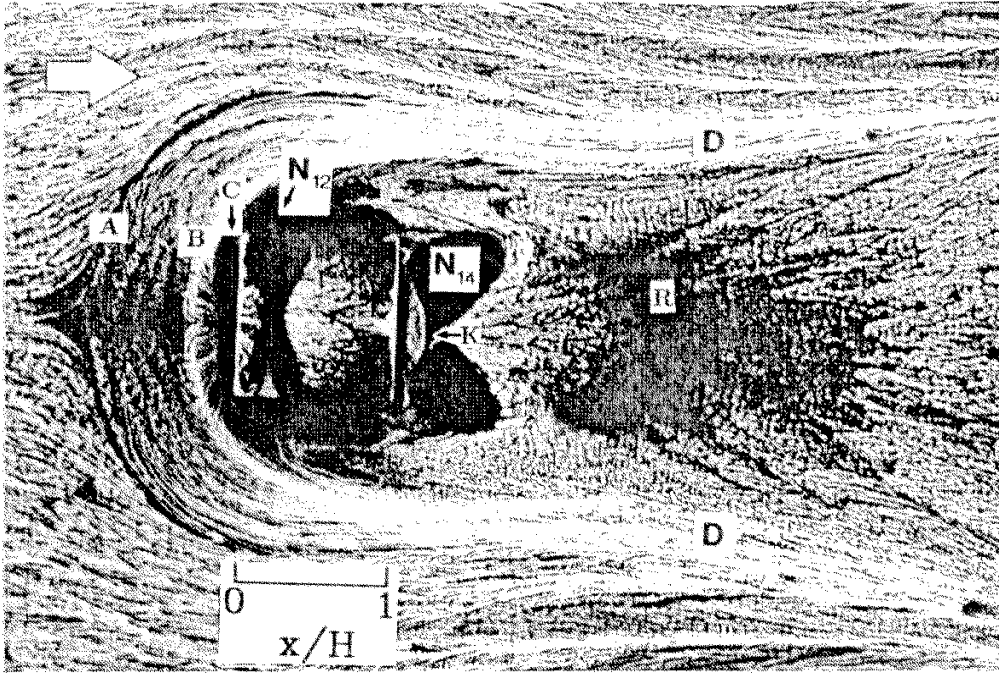
Figure 3.4: Reference experiment oil-film visualization of time-averaged flow in a horizontal plane near the channel floor and at the cube rooftop (reprinted with kind permission from Martinuzzi, 1992; Martinuzzi and Tropea, 1993).

Name	X_{F1}	X_B	X_T	X_{R1}	X_{R2}
EXP	1.040		–	1.612	
LES3	1.287		–	1.696	0.265
LES4	0.998		–	1.432	0.134
LES5	1.228		–	1.700	0.22
UBWM2	0.808		0.837	1.722	
N10	0.950	–	0.850	1.950	–
N20	1.175	–	0.925	1.525	–
N32	1.016	–	0.922	1.484	0.172
N40	0.963	–	0.888	1.538	0.213
N50	0.910	–	0.890	1.570	0.230
N64	0.898	0.398	0.930	1.648	0.242
N80	0.894	0.369	0.956	1.694	0.244
K-E	0.65		0.432	2.20	0.02
RNG	0.52		0.24	2.08	
KATO-L	0.65		–	2.73	0.02
TWO-L	0.95		–	2.73	0.25

Table 3.4: Characteristic length scales of flow separation and reattachment in units of H as defined in Figure 3.9. The length scale X_{F1} relates to separation vortex A, the new length scale X_B relates to separation vortex B in Figure 3.4.

25

(a) LES3

(b) RANS: K-E

(c) LES4

(d) RANS: RNG

(e) LES5

(f) RANS: KATO-L

(g) UBWM2

(h) RANS: TWO-L
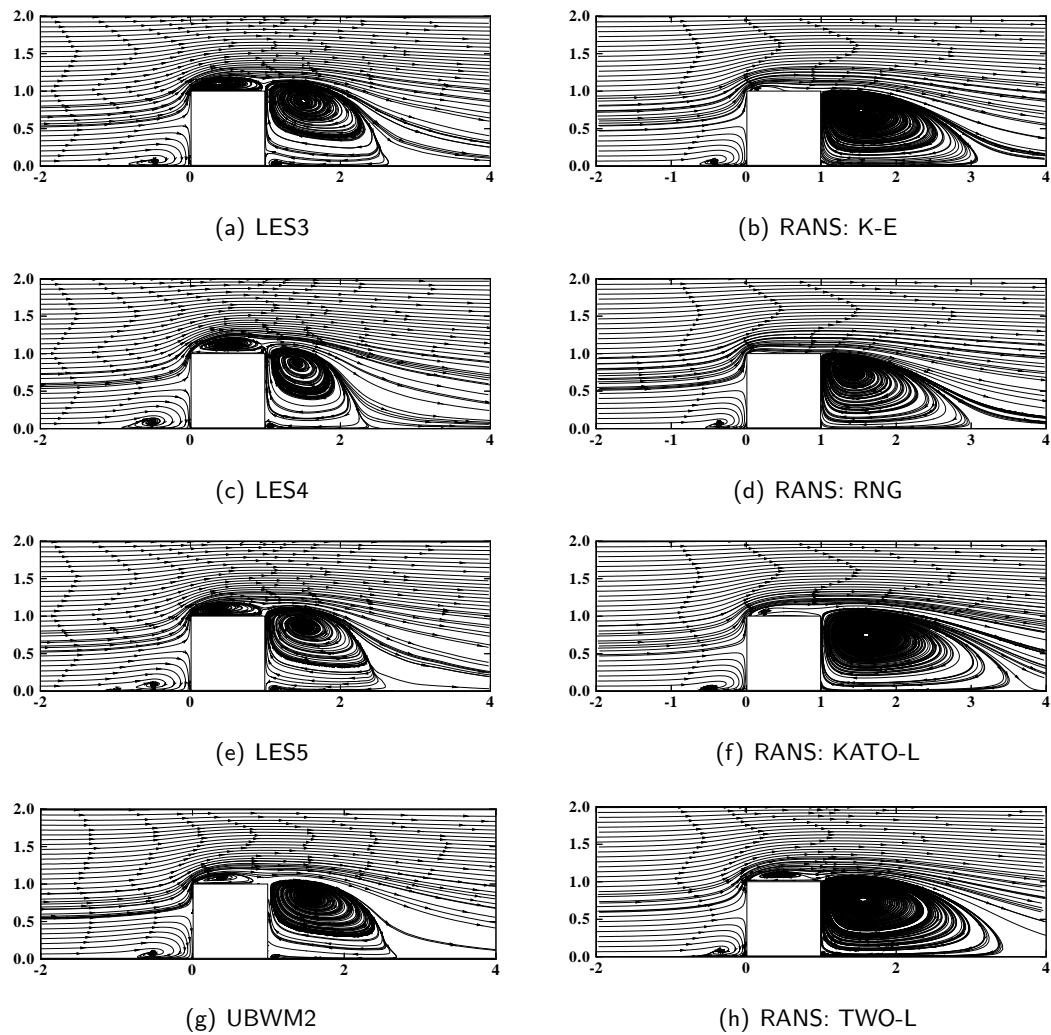
Figure 3.5: LES (left; a,c,e,g) and RANS (right; b,d,f,h) model streamlines of time-averaged flow in the vertical symmetry plane ($\frac{z}{H} = 0$) (reprinted with kind permission from Breuer, 2002). For abbreviations refer to Tables 3.1 and 3.3 on page 22.

(a) N10

(b) N20

(c) N32

(d) N40

(e) N50

(f) N64

(g) N80
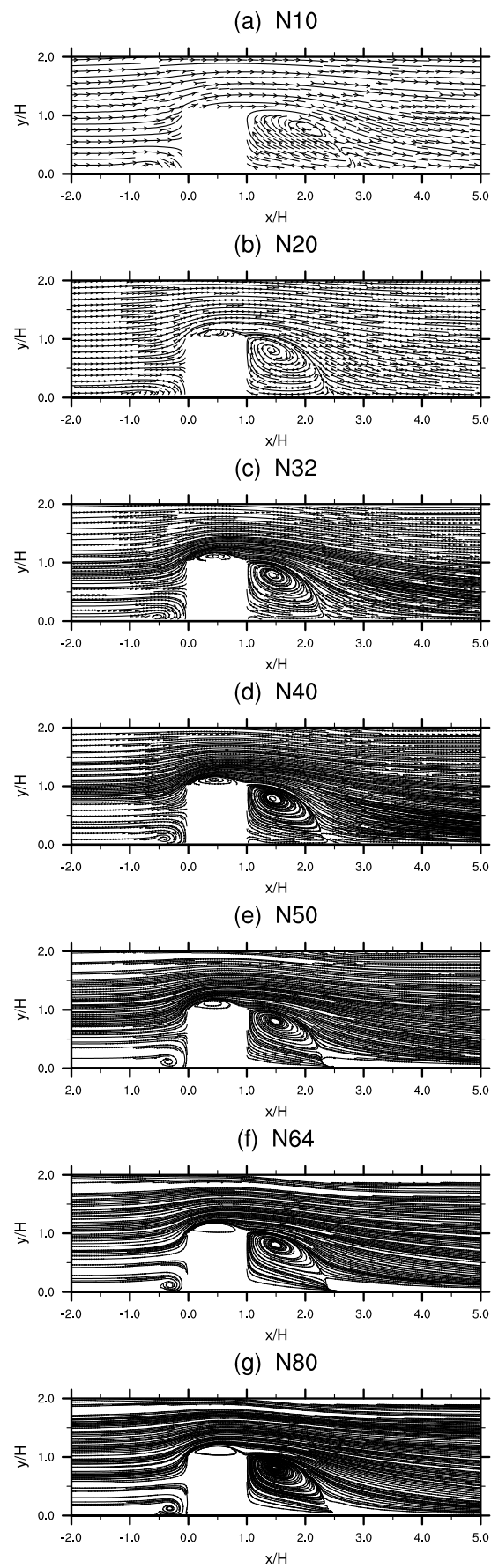
Figure 3.6: PALM streamlines of time-averaged flow in the vertical symmetry plane ($\frac{z}{H} = 0$) from simulations with different resolution.

(a) LES3

(b) LES4

(c) LES5

(d) UBWM2

(e) RANS: K-E

(f) RANS: RNG

(g) RANS: KATO-L

(h) RANS: TWO-L
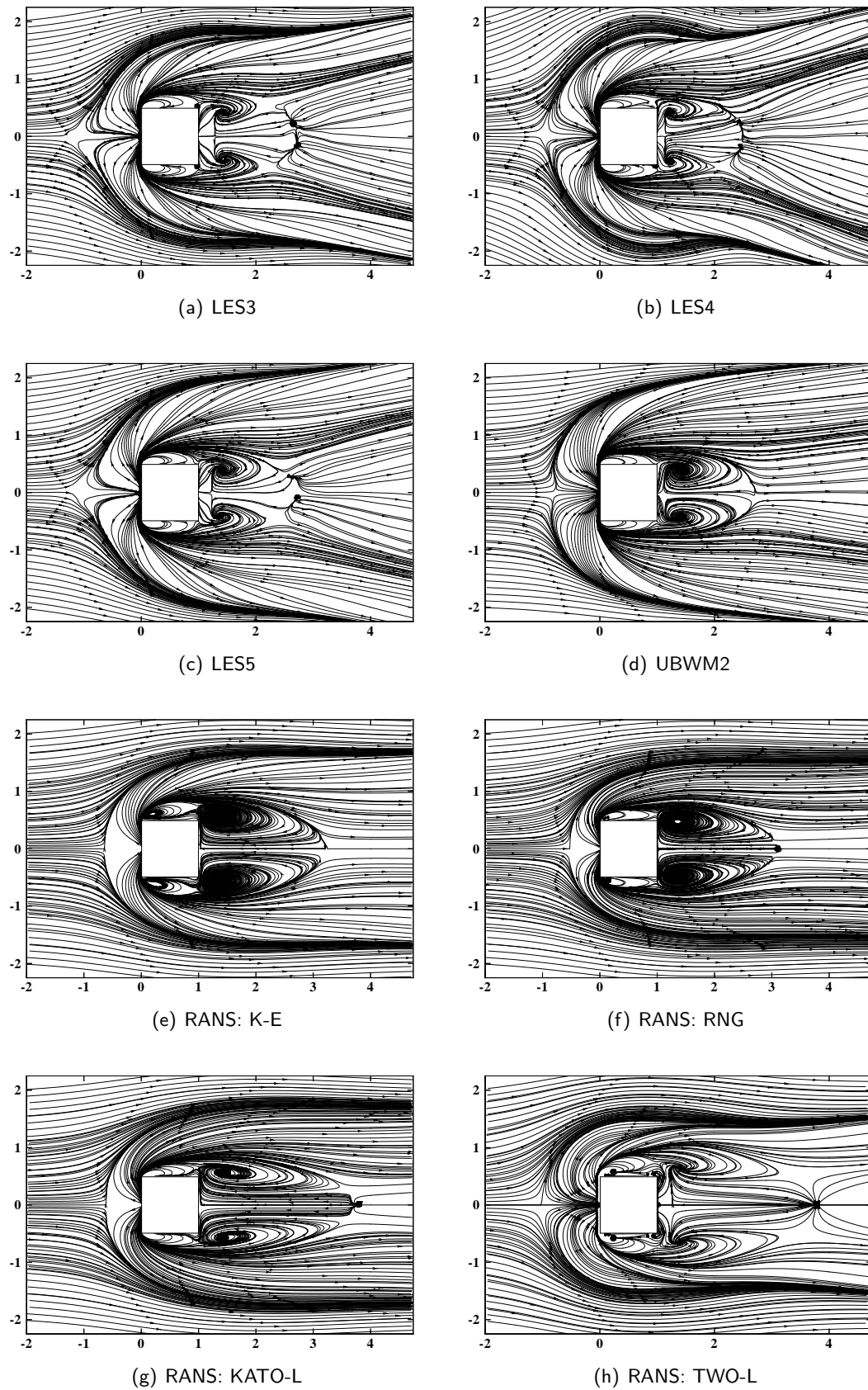
Figure 3.7: LES (a-d) and RANS (e-h) model streamlines of time-averaged flow in a horizontal plane near the channel floor (reprinted with kind permission from Breuer, 2002). For abbreviations refer to Tables 3.1 and 3.3 on page 22.
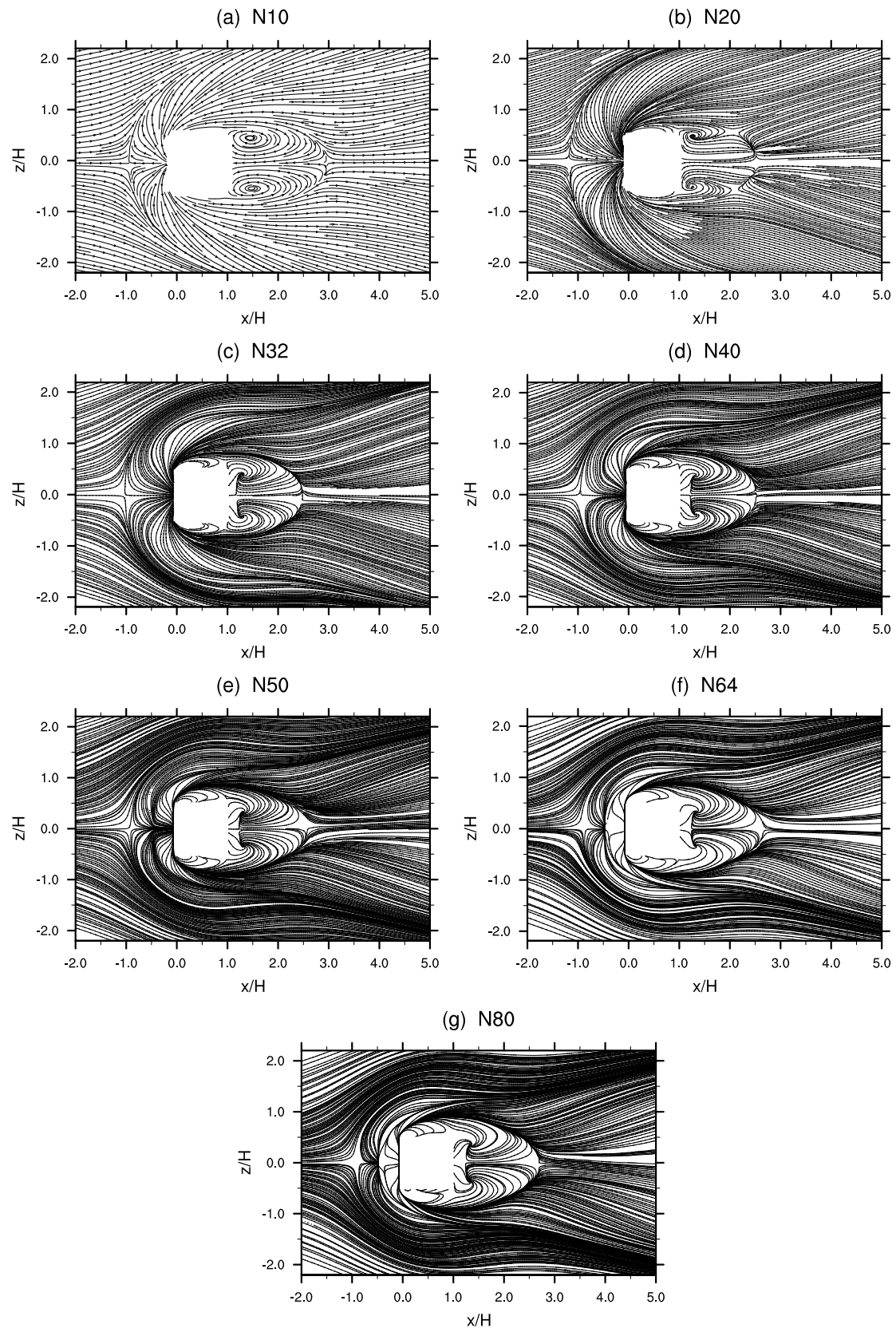
Figure 3.8: PALM streamlines of time-averaged flow in a horizontal plane near the channel floor from simulations with different resolution.
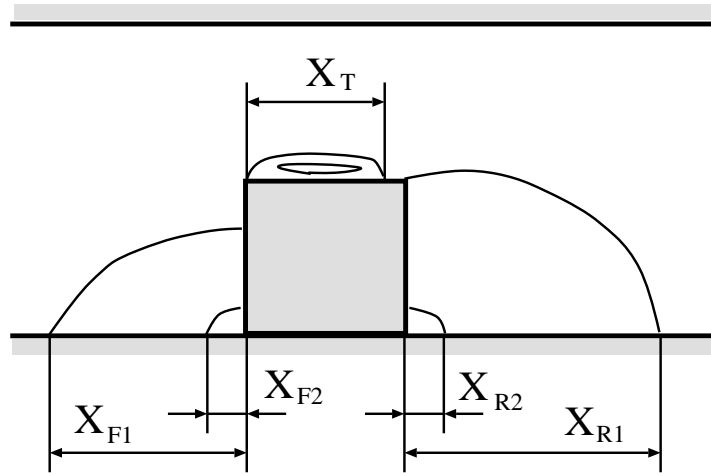
Figure 3.9: Definition of characteristic length scales in the symmetry plane ($\frac{z}{H} = 0$, reprinted with kind permission from Rodi et al., 1995). X_{F1} relates to separation vortex A, the new length scale X_B (not shown) relates to separation vortex B in Figure 3.4.

holds for PALM since even the highest resolution run N80 with $\Delta_{\text{min, wall}} = 0.125$ (same as LES3-5) produces reattachment. Possible reasons may be the higher Reynolds number or the different surface treatment in PALM where the top wall is smooth without wall functions whereas all other surfaces are rough. Two RANS models do not produce the roof vortex at all, the two others give X_T between 0.24 and 0.43.

Generally good agreement among the LES models including PALM and the wind tunnel experiment is observed for the reattachment length X_{R1}. Exceptions are LES4 (dynamic SGS) that underestimates X_{R1} and the lowest resolution PALM run N10 that overestimates X_{R1} as do all RANS models.

From the wind tunnel experiment Martinuzzi (1992) inferred the existence of a vortex in the corner just behind the cube and the channel floor but could not measure X_{R2}. LES3, LES5, PALM N40-N80 and TWO-L suggest a value of ca 0.21-0.26.

Table 3.4 also includes a new length scale X_B. It relates to the separation vortex B in Figure 3.4 that appears to be picked up by the two highest resolution PALM runs N64 and N80. However, B is not discernible from the streamline cross-sections (Figs. 3.6 and 3.8). Figure 3.10 shows that while indeed only N64 and N80 actually reproduce B, increasing PALM resolution starting from N32 already seems to indicate the formation of B. It also shows the existence of a corner vortex not only just behind but also just in front of the cube in higher resolution runs.

3.3 Turbulence statistics

For a more quantitative validation compared to the previous section, this section uses vertical profiles of turbulence statistics at selected locations along the symmetry plane ($\frac{z}{H} = 0$). It quantitatively analyses and compares the LES and RANS results with the wind tunnel experiment.

Figures 3.11 and 3.12 show vertical profiles of streamwise velocity $\overline{u}$, its temporal variance $\overline{u'u'}$, and temporal shear stress $\overline{u'v'}$ at $\frac{x}{H} = 0.5, 2.0, 4.0$ from LES3-5 and PALM N10-N80, respectively. Breuer (2002) discusses the relatively small differences between LES3-5 and finds no clear superiority of the dynamic SGS model (LES4) because its good performance
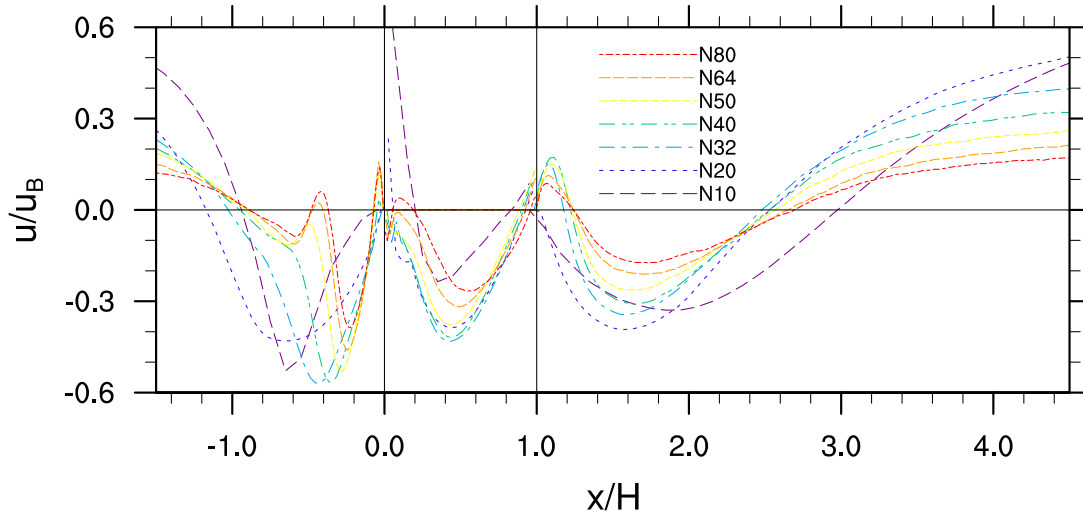
Figure 3.10: Streamwise velocity normalized by the bulk velocity u_b in the symmetry plane $(\frac{z}{H} = 0)$ at the lowest grid level above the channel floor/cube rooftop from PALM simulations with different resolution. Note that this normalization alone does not collapse lines N10-N80 because it does not account for the different height of the respective grid levels.

above the cube $(\frac{x}{H} = 0.5)$ and its good reproduction of the horse-shoe vortex are partly counterbalanced by the poor representation of the recirculation region $(\frac{x}{H} = 2)$. The PALM profiles of $\overline{u}$ in Fig. 3.12a-c behave very similar to UBWM2 (Rodi et al., 1995, not shown): in (a) the roof vortex is weaker and more shallow than in the wind tunnel (which is consistent with the reattachment observed in both UBWM2 and PALM), in (b) the strength and height of the recirculation region are underestimated and in (c) $\overline{u}$ is overestimated in the height interval between 0.8 and $1.6\,H$.

Profiles of higher-order moments $\overline{u'u'}$ and $\overline{u'v'}$ in Fig. 3.12d-f agree quite well with those of LES3-5 in 3.11d-f. Agreement with experimental profiles obtained from measurements in the $(u\text{-}w)$ plane in Figs. 3.12e and 3.11e is much better than from the $(u\text{-}v)$ plane, as noted by Breuer (2002). The PALM resolution study obtains convergence starting from run N32. Due to the relatively long averaging time $(T^*_{\text{averaging}} = 576)$ the PALM profiles of higher-order moments are smoother than those of LES3-5 $(T^*_{\text{averaging}} \approx 108\ldots151)$.

Vertical profiles of streamwise velocity $\overline{u}$ at $\frac{x}{H}$ = -1.0, 0.5, 1.0, 1.5, 2.5, 4.0 in the symmetry plane $(\frac{z}{H} = 0)$ are shown in Figure 3.13 for LES3-4 and RANS models and in Figure 3.14 for PALM. All start with a good agreement with the wind tunnel at $\frac{x}{H}$ = -1.0 (a). Above the cube center PALM, KATO-L and TWO-L produce a weaker roof vortex, K-E and RNG do not produce a roof vortex (cf. section 3.2). Due to the reattachment on the roof PALM does not produce the shallow recirculation at $\frac{x}{H} = 1.0$ observed in LES3-4 and in the wind tunnel, nor do the RANS models. However, PALM very well reproduces the wind profile further aloft. At $\frac{x}{H} = 1.5$, well within the recirculation region, none of the models is able to capture the full strength and height of this region adequately; LES3 comes closest to the measurements. The overestimation of the length of the recirculation region by the RANS models becomes obvious at $\frac{x}{H} = 2.5$, close to the reattachment point, where they still give reverse flow. Due to its underestimation of the recirculation length LES4 here gives too large values of $\overline{u}$ close to the channel floor. LES3 and PALM perform best here. The difference between LES models including PALM and RANS models is perhaps most striking at $\frac{x}{H} = 4.0$, in a region where the flow has already reattached and fully-developed channel

(a) $U : x/H = 0.5$

(b) $U : x/H = 2.0$

(c) $U : x/H = 4.0$

(d) $\overline{u'u'} : x/H = 0.5$

(e) $\overline{u'u'} : x/H = 2.0$

(f) $\overline{u'u'} : x/H = 4.0$

(g) $\overline{u'v'} : x/H = 0.5$

(h) $\overline{u'v'} : x/H = 2.0$

(i) $\overline{u'v'} : x/H = 4.0$
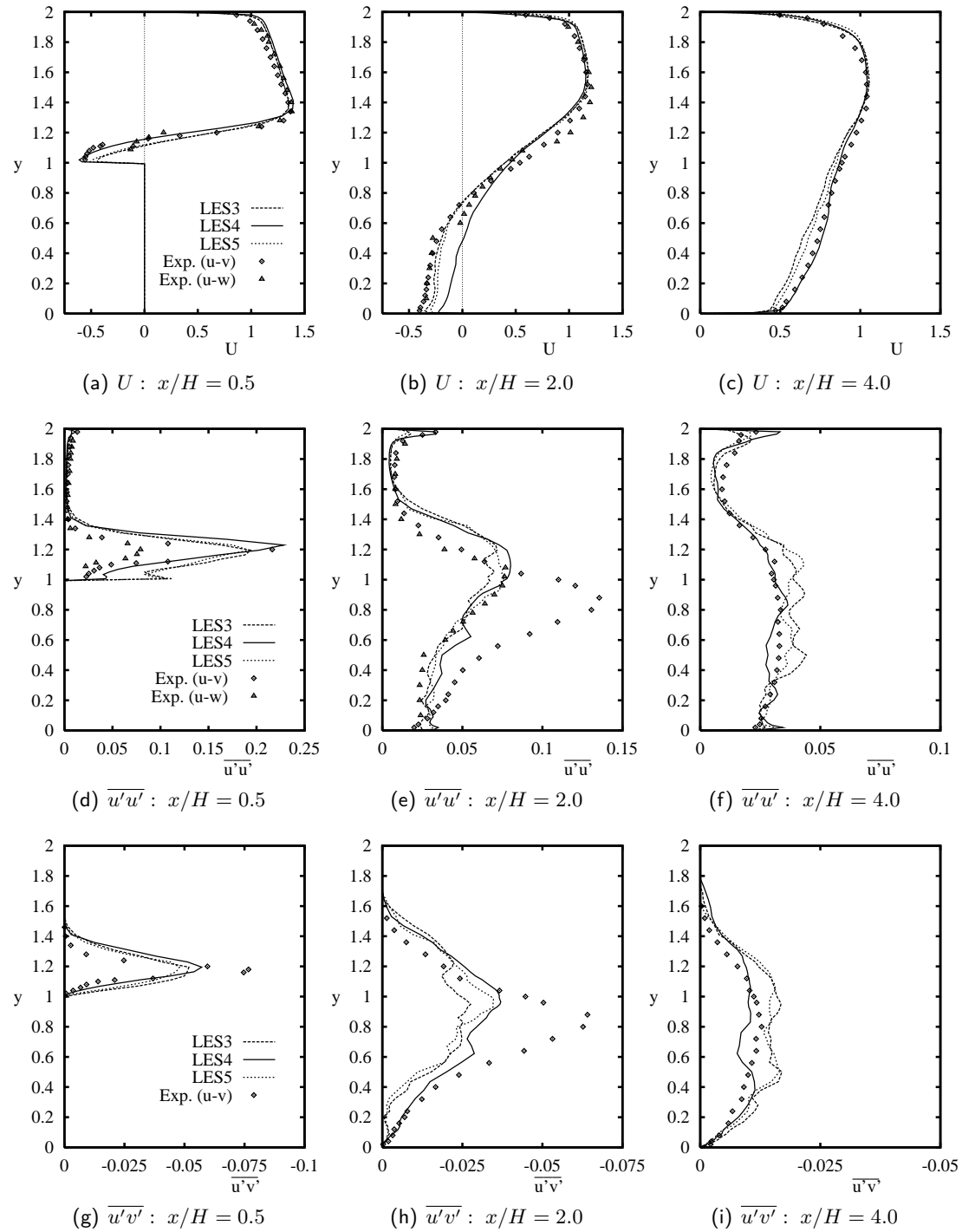
Figure 3.11: Vertical profiles of streamwise velocity $\overline{u}$, its temporal variance $\overline{u'u'}$, and temporal shear stress $\overline{u'v'}$, normalized by the bulk velocity u_b, at $\frac{x}{H} = 0.5, 2.0, 4.0$ in the symmetry plane $\left(\frac{z}{H} = 0\right)$ from LES3-5 (reprinted with kind permission from Breuer, 2002).
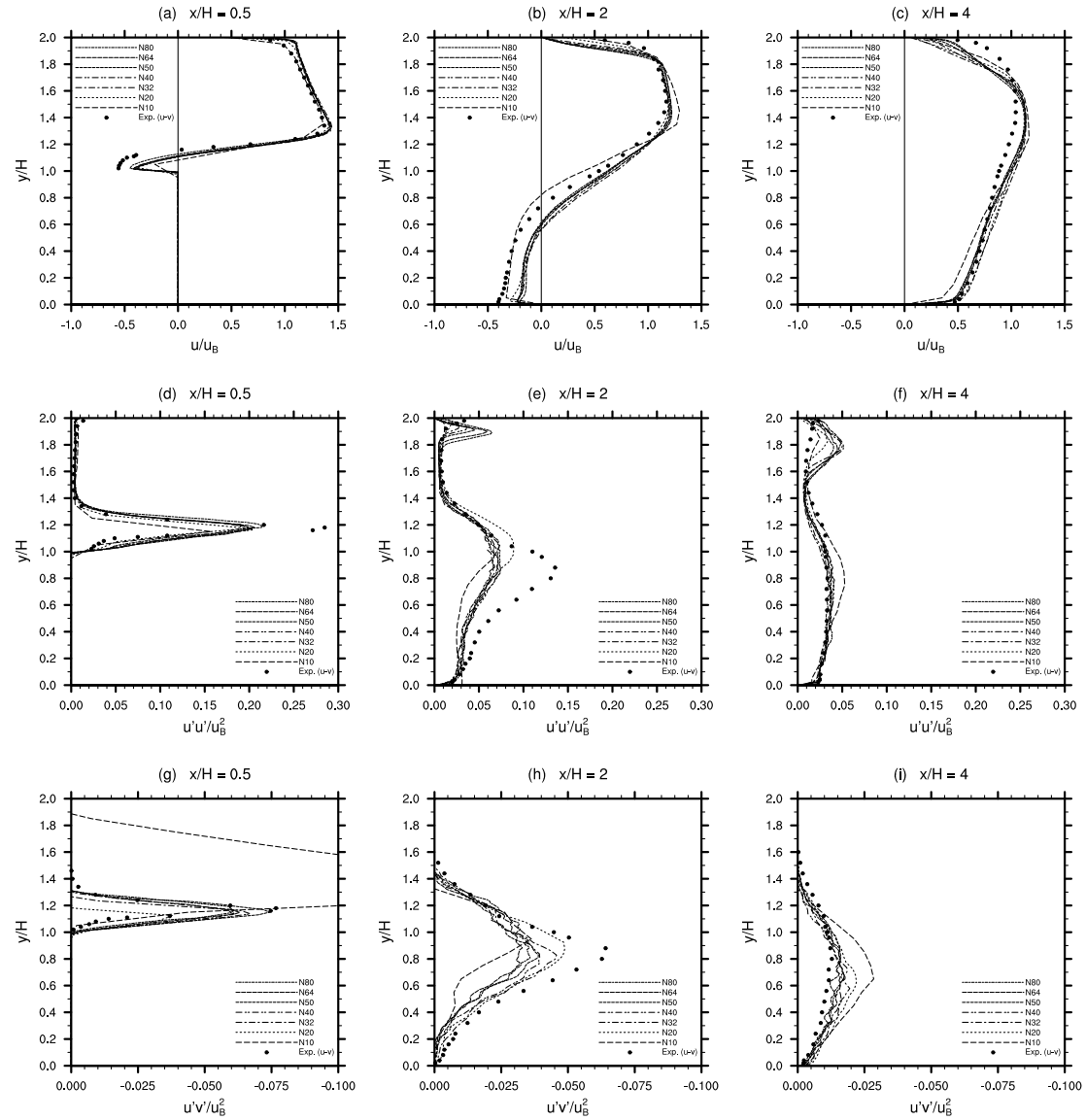
Figure 3.12: Vertical profiles of streamwise velocity $\overline{u}$, its temporal variance $\overline{u'u'}$, and temporal shear stress $\overline{u'v'}$, normalized by the bulk velocity u_b, at $\frac{x}{H} = 0.5,\ 2.0,\ 4.0$ in the symmetry plane $\left(\frac{z}{H} = 0\right)$ from PALM simulations N10-N80.
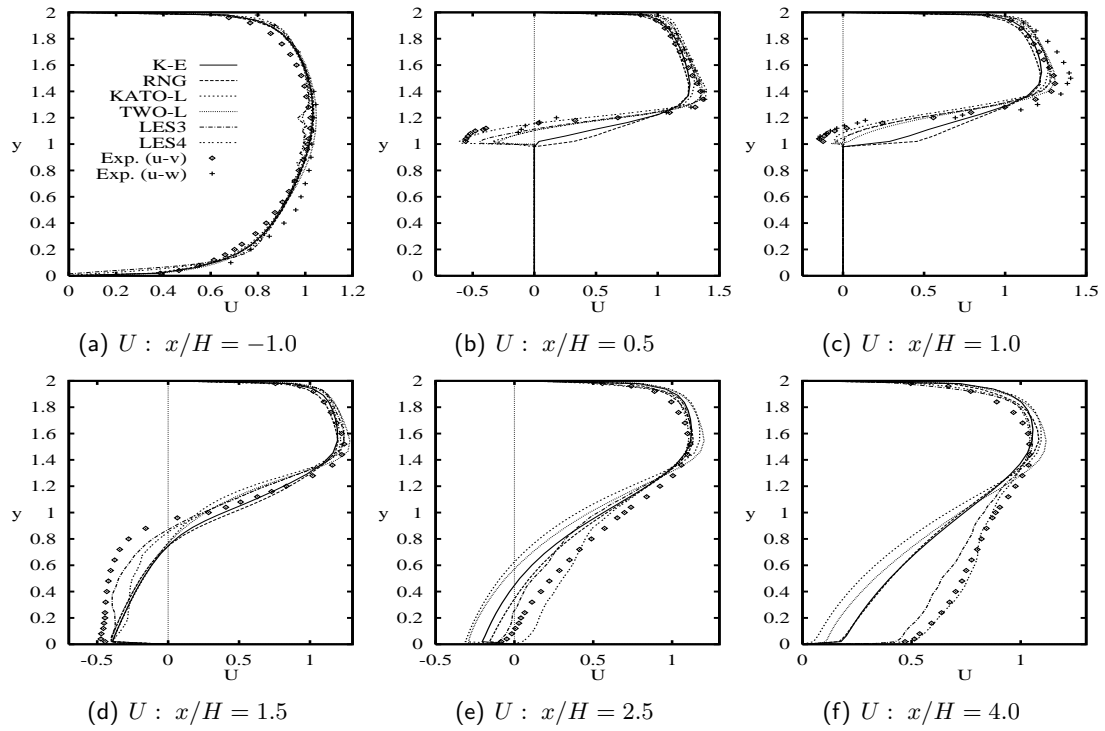
Figure 3.13: Vertical profiles of streamwise velocity $\overline{u}$ normalized by the bulk velocity u_b at $\frac{x}{H} =$ -1.0, 0.5, 1.0, 1.5, 2.5, 4.0 in the symmetry plane $\left(\frac{z}{H} = 0\right)$ from LES3-4 and RANS models (reprinted with kind permission from Breuer, 2002).
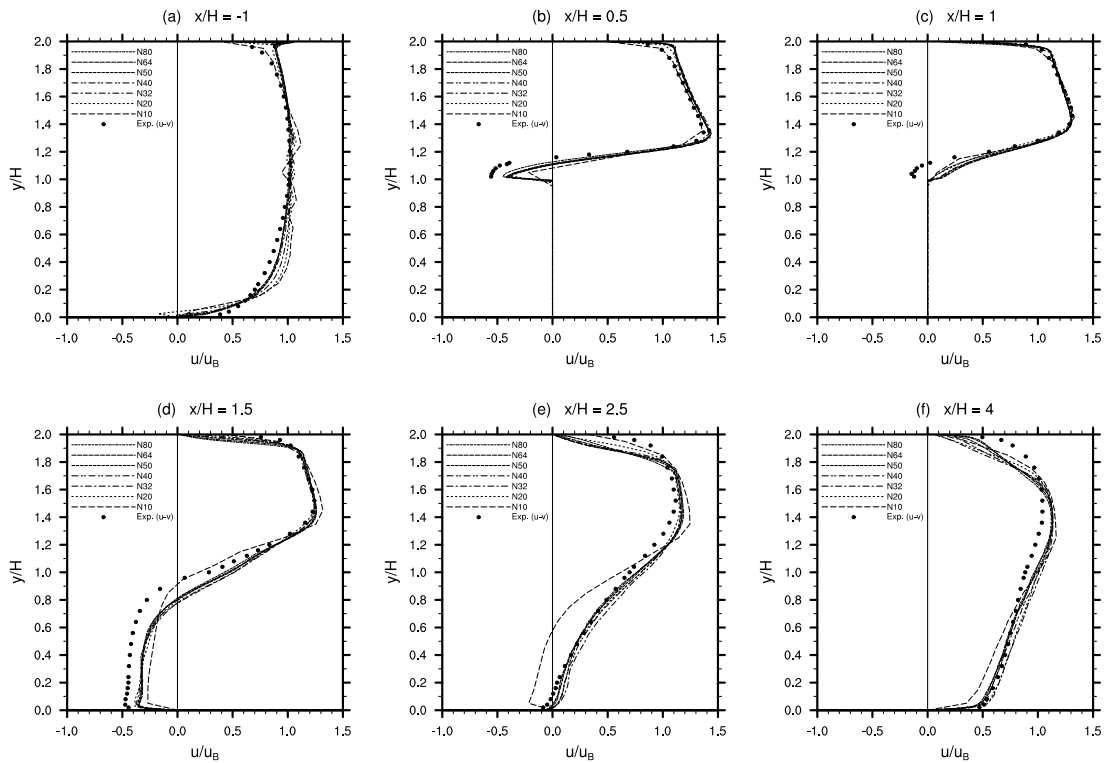
Figure 3.14: Vertical profiles of streamwise velocity $\overline{u}$ normalized by the bulk velocity u_b at $\frac{x}{H} =$ -1.0, 0.5, 1.0, 1.5, 2.5, 4.0 in the symmetry plane $\left(\frac{z}{H} = 0\right)$ from PALM simulations N10-N80.
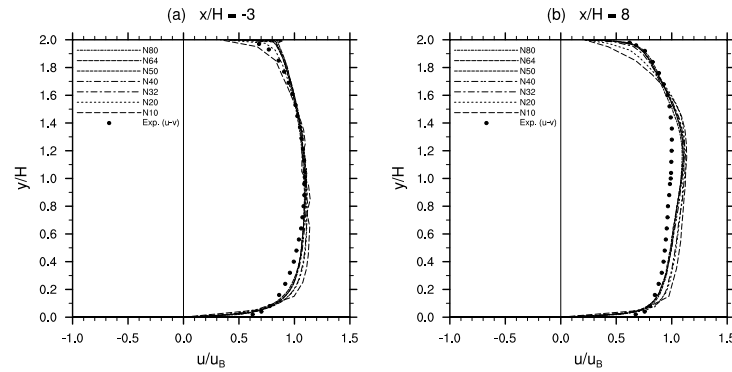
Figure 3.15: Vertical profiles of streamwise velocity $\overline{u}$ normalized by the bulk velocity u_b at $\frac{x}{H} =$ -3.0, 8.0 in the symmetry plane ($\frac{z}{H} = 0$) from PALM simulations N10-N80.

flow is slowly regenerated. This process is well captured by LES including PALM, while $\overline{u}$ shows a large deficit below $\frac{y}{H} = 1.2$ in all RANS models.

As mentioned in section 3.1, cyclic boundary conditions in both horizontal directions were the only choice at the time the validation simulations were performed. Periodic boundary conditions in streamwise direction were, however, clearly discouraged by the workshop organizers (Rodi et al., 1995). One submission for case B1 that did use them with a streamwise domain length of $12\,H$ indeed produced significantly different results. Rodi et al. (1995) and Breuer (2002) mainly attribute this submission's error to the observation that the flow (re-)approaching the cube had not yet recovered to a fully developed channel flow. In order to avoid this error, PALM runs N10-N80 used an enlarged streamwise domain length of $19.2\,H$. Experimental reference data are available at $\frac{x}{H} =$ -3.0 and up to $\frac{x}{H} = 8.0$. This allows the comparison of the channel flow recovery in PALM with the wind tunnel measurements shown in Figure 3.15. At $\frac{x}{H} = 8.0$ PALM slightly overestimates $\overline{u}$, while at $\frac{x}{H} =$ -3.0 the wind tunnel profile is well reproduced. This suggests that the use of periodic streamwise boundary conditions may be justified provided the computational domain is long enough.

3.4 Resolution recommendation for PALM

PALM has been shown to well reproduce the flow around a single surface-mounted cube in fully developed turbulent neutral channel flow and to perform on the level of other LES models. Although PALM simulated urban scales with a much larger resulting Reynolds number ($Re_H = 3.3 \cdot 10^6$) and used cyclic streamwise boundary conditions, no significant differences have been found, which suggests that their effects on the main flow are small in the present configuration.

PALM runs N10-N80 have been performed with a resolution ranging from 10 to 80 grid points per cube face corresponding to $\Delta_{\text{min, wall}}$ ranging from 0.1 to 0.0125 (Table 3.2). The project goal to surpass the accuracy of existing LES models by using an unprecedented, fine grid resolution could not be achieved: with increasing grid resolution the PALM simulations converged to one solution, and this one solution was comparable to but not better than the solutions of existing LES models. This behaviour may on the one hand be due to deficiencies in the PALM simulations, e.g. different boundary conditions (cyclic streamwise boundary conditions and the missing Prandtl layer at the top of the model domain) or numerical schemes (advection, SGS, ...). However, on the other hand, none of the various LES models was able to match the wind tunnel results exactly throughout the entire domain. This

observation could hint at a systematic difference in the experimental set-up between the wind tunnel and the numerical models (e.g. spanwise boundary conditions). In this case the accuracy of PALM could in the end only be measured by a comparison with the other LES models.

The results presented in the previous sections 3.1 and 3.3 suggest that for many PALM applications N32 can be expected to yield sufficient results, i.e. a simulation with 32 grid points per cube face or $\Delta_{\mathsf{min, wall}} = 0.03125$. At this resolution the near-wall flow, especially in corners, appears to have negligible influence on the main flow. However, if the near-wall or corner flow are of specific interest, then a much higher resolution (N40~N64) may be necessary.

It should be noted that the recommendations given in this chapter are based on an experiment where the obstacle is actively approached by the flow. They may not hold in obstacle configurations that include stagnant zones such as the lower parts of deep street canyons or courtyards. A resolution study for such a set-up will be given in the following chapter.

The resolution used in urban LES and in LES of obstacle flow varies. Uniform grids like in PALM are widely used, which allows an intuitive resolution comparison in terms of the number of grid points per cube face. For neighbourhood/local scale LES like the Hong Kong study in chapter 6, Tseng et al. (2006) consider 6-8 grid points the minimum. For street scale/microscale LES Hanna et al. (2002) and Kanda et al. (2004) use 10 and Stoesser et al. (2003) 25 grid points (cf. Hellsten and Rautaheimo, 1999). Based on comparison with experimental data by Castro et al. (2006) and DNS by Coceal et al. (2006), Xie and Castro (2006) conclude that urban LES requires at least 15-20 grid points to get the large-scale flow dynamics right. Krajnović and Davidson (2002) recommend about 32 grid points per cube face, and so do Coceal et al. (2006) for DNS ($Re = 5\,000$). Several LES models use non-uniform grids (e.g. LES3-5, UBWM2, Shah and Ferziger, 1997) and can easily obtain a smaller, locally refined $\Delta_{\mathsf{min, wall}}$ near obstacles than models with uniform grids. Based on the evidence from literature and the present study, it can be concluded that PALM simulations with 32 grid points per cube face are a good compromise between accuracy and speed and are thus recommended.

4 Research example: Street canyon

This chapter constitutes the main part of this study and gives an example of fundamental research with urban LES: a parameter study of urban street canyons. Section 4.1 motivates the street canyon study and introduces the terminology, and section 4.2 describes the experimental set-up. Section 4.3 introduces a method of computationally efficient calculation of higher-order turbulent statistics in complex geometry flows. The basic topology and dynamic driving mechanism of street canyon (skimming) flow is discussed in section 4.4, followed by results, discussion and conclusions in sections 4.5, 4.6 and 4.7, respectively.

4.1 Introduction

By analogy with natural canyons, the term *street canyon* refers to the space between buildings lining up along both sides of a street, from street surface to rooftop level. The street canyon forms the basic urban geometric unit in many urban areas worldwide.

Vardoulakis et al. (2003) and Ahmad et al. (2005) compiled the following canyon terminology that is commonly used in urban climate literature. The key parameter to describe the geometry of a street canyon is its *aspect ratio* of canyon height H divided by canyon width W. A *regular* or *uniform* canyon has $H/W \approx 1$ without major inhomogeneity along its axis. $H/W < 0.5$ characterizes *shallow*, $H/W > 2$ *deep* canyons. The canyon length L (along the canyon axis) is limited, for example, by major intersections; canyons with $L/H \approx 3, 5, 7$ are called *short*, *medium*, and *long*, respectively. *Symmetric* or *even* canyons have equal building heights on either side. In case of perpendicular *free-stream* flow above rooftop, the downwind canyon wall is often called *windward* (because this is where the high momentum flow impinges), upwind canyon wall is called *leeward*. *Asymmetric* canyons are either *step up* canyons with high-rise buildings downstream or *step down* canyons with high-rise buildings downstream.

The classification into three perpendicular canyon flow regimes introduced by Oke (1988) provides a useful framework for further discussion in this chapter; this classification is commonly used in urban climate literature. Figure 4.1 sketches the flow regimes associated with airflow across street canyons of different aspect ratio H/W. They are composed of the same flow structures as in the symmetry plane of the single building case discussed in chapter 3: an upstream recirculation, flow separation with reattachment, and a larger downstream recirculation. In shallow canyons, the buildings are sufficiently separated so that their flow fields do not interact, this is the *isolated roughness flow* regime (IRF, Fig. 4.1a). For a closer building spacing they do interact, which is referred to as *wake interference flow* (WIF, Fig. 4.1b). In regular and deep canyons the buildings are so densely spaced that the bulk of the flow just skims over them and does not enter the canyon. Vertical wind shear atop the canyon drives a recirculation within − the canyon vortex (discovered by Albrecht and Grunow, 1935). This is the *skimming flow* regime (SF, Fig. 4.1c).

Note that in fluid mechanics turbulent flow over rough walls is classified into *k-type* and *d-type* roughness (Perry et al., 1969; Jiménez, 2004). Isolated roughness and wake interference flow correspond to k-type, skimming flow corresponds to d-type roughness. The present study solely uses the terminology of Oke (1988).

(a) Isolated roughness flow

(b) Wake interference flow   (c) Skimming flow
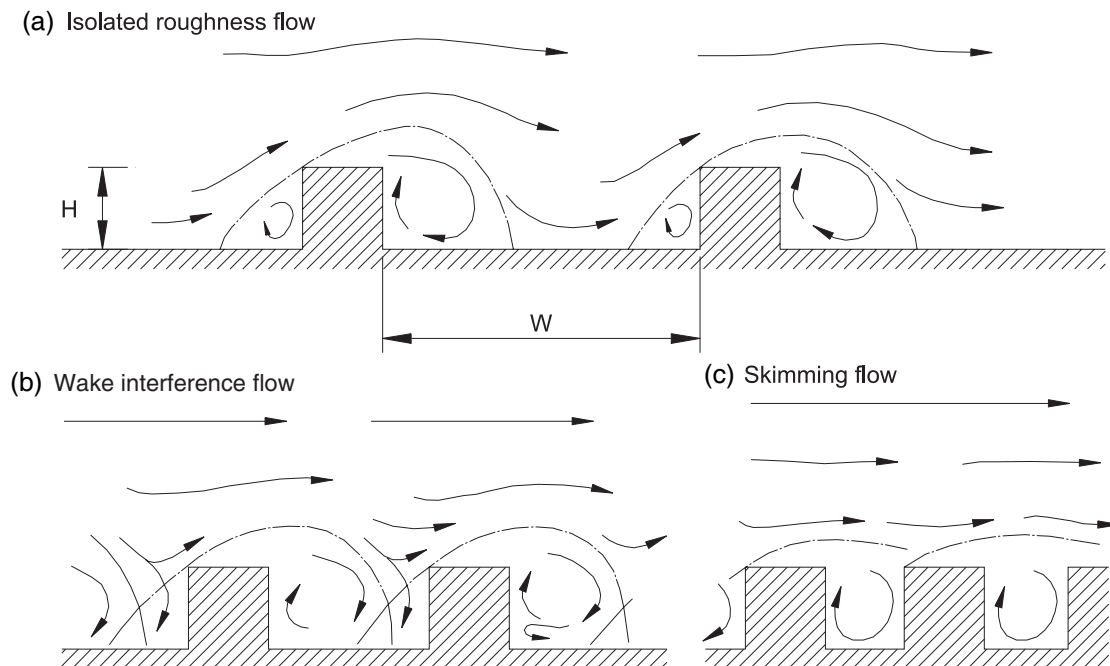
Figure 4.1: Flow regimes of airflow over street canyons of different aspect ratio of canyon height H to width W (modified after Oke, 1988).

The airflow structure within street canyons is of crucial importance for the dispersion of pollutants (especially vehicular exhausts generated at street level) and has thus attracted research over many decades. Dabberdt et al. (1973), DePaul and Sheih (1985, 1986), Yamartino and Wiegand (1986) and Nakamura and Oke (1988) conducted early field experiments aiming at these questions. These and scale model results (e.g. Hoydysh and Dabberdt, 1988) were also used to validate simple urban dispersion models. Street canyon ventilation was found weakest in case of a truly perpendicular flow across deep canyons when the vertical exchange at roof level as well as the along-canyon flow are weak. Already a small wind component parallel to the canyon axis causes flow channeling within the street canyon, which is more beneficial for pollutant dispersion. The present study therefore focusses on street canyons approached by perpendicular free stream flow.

Based on a literature review Oke (1988) suggested that the critical canyon aspect ratio limits between the isolated roughness, wake interference and skimming flow regimes are $H/W \approx 0.3$ and 0.65, respectively, in the 2D limit of infinitely long street canyons. Besides further field studies, these regimes were subsequently also studied using indoor and outdoor scale models as well as numerical models, which is covered in comprehensive reviews by Kanda (2006) and Li et al. (2006), respectively. As one result, the *skimming flow* regime was subdivided according to the vertical number of mean flow recirculations. Whereas regular canyons have a single recirculation, two vortices form in deep canyons with $H/W \gtrsim 2$ where the ambient wind drives the upper vortex that in turn drives a counterrotating, weaker lower vortex (Ahmad et al., 2005). Some numerical studies identified a weak third vortex at even higher aspect ratios. Among the five numerical studies that are compared by Li et al. (2006) there is a significant scatter concerning the aspect ratio thresholds between one (SF1), two (SF2), and three (SF3) canyon recirculations. Table 4.1 chronologically lists over twenty numerical street canyon studies; it provides basic information about the employed numerical models and confirms the scatter between SF1, SF2, and SF3. This scatter is one of the

Reference	Mod.	$z_{0,loc}$	SF1	SF2	SF3	Remarks
Ghia et al. (1982)	2 R		1			lid-driven cavity; high resolution (257×257)
Lee and Park (1994)	2 R	no-slip	0.3–2.1	2.4–3		
Ca et al. (1995)	2 L		≤ 1	≥ 2		
Johnson and Hunter (1995)	3 R		0.87–1.2			WIF at $H/W = 0.52 \ldots 0.67$
Sini et al. (1996)	3 R	0.05	0.67–1.67	1.96	3	WIF at $0.67 < H/W < 0.14$; IRF at $H/W = 0.1$
Chabni et al. (1998)	2 L					WIF at $H/W = 0.5$
Hassan and Crowther (1998)	2 R		0.25–1			WIF at $H/W = 0.125$
Baik and Kim (1999)	2 R	no-slip	1	1.5–3	3.5	model of Lee and Park (1994) with $k - \varepsilon$ closure
Huang et al. (2000)	2 R		0.25–1			
Kim and Baik (2001)	2 R	0.05	0.6–1.2	1.4–3.2	3.4–3.6	
Chan et al. (2002)	2 R	0.0015	1	3		$z_{0,loc}$ of Meroney et al. (1996); WIF at $H/W = 0.25$
Jeong and Andrews (2002)	2 R	0.05	0.67–1.6	1.6–3	>3	
Kovar-Panskus et al. (2002a)	3 R		0.5–1.43	2	3.33	
Soulhac et al. (2001)	2/3 R	0.015	1	3		threshold SF1-SF2 depends on $z_{0,loc}$
Walton and Cheng (2002)	3 L/R		1.2			
Leonardi et al. (2003)	3 D	no-slip	0.33	?	?	SF at $H/W = 0.25 \ldots 3$; WIF at $H/W = 0.18$; IRF at $H/W = 0.14 \ldots 0.05$
Cui et al. (2004)	3 L		1			cyclic streamwise b.c.
Liu et al. (2004)	3 L	no-slip	0.5–1	2		wall-resolving LES; cyclic streamwise b.c.
Li et al. (2005)	2 R	no-slip	0.5–1	2		validated by LES of Liu et al. (2004)
Santiago and Martín (2005)	3 R	0.1	1	2	4	
So et al. (2005)	3 L	no-slip	1–1.2	1.5–2		wall-resolving LES; WIF at $0.3 < H/W < 1$; IRF at $H/W < 0.3$
present study (2007)	3 L	0.01–0.1	0.25–2	2.9–4		cyclic streamwise b.c.; WIF at $H/W = 0.15$

Table 4.1: Numerical street canyon studies in chronological order.
Abbreviations: Mod.: Model type (2=2D, 3=3D, R=RANS, L=LES, D=DNS); $z_{0,loc}$: local wall roughness length [m]; SFn: skimming flow with n canyon vortices; WIF: wake interference flow; IRF: isolated roughness flow; b.c.: boundary conditions.

main reasons that motivated the present study; therefore its focus is on the skimming flow regime.

Table 4.1 also reflects the gradual shift from 2D to 3D and from RANS to LES models in recent years in recognition of the well-known shortcomings of 2D and RANS models (Li et al., 2006). Even in the 2D limit of an infinitely long street canyon, the turbulent flow is still fully 3D (e.g. Liu et al., 2004; Li et al., 2006). LES gives more accurate mean results than RANS, however, it may be even more important that LES also gives spatial and temporal turbulent fluctuations (cf. section 1.3) that allow a deeper insight into the canyon flow processes. Therefore the present study does not stop at comparing the mean canyon flow topology with previous results. It also explores turbulence statistics *within* the street canyon with an unprecedentedly high resolution.

In his review Roth (2000) scaled urban turbulence statistics from over fifty field studies to produce a consistent picture of turbulence *above* the urban canopy. However, turbulence statistics *within* the urban canopy are less consistent. Turbulence statistics from the present street canyon parameter study are compared with results from street canyon field studies by Rotach (1995); Christen et al. (2003); Christen (2005); Eliasson et al. (2006), wind tunnel studies by Brown et al. (2000); Uehara et al. (2000); Kastner-Klein et al. (2001, 2004) and LES by Walton and Cheng (2002); Cui et al. (2004); Liu et al. (2004). Furthermore, a comparison with LES by Kanda et al. (2004) and DNS by Coceal et al. (2006), who both investigated arrays of cubes, and the review by Britter and Hanna (2003) will stress the differences between different urban morphologies.

Reviews by Robins and Macdonald (2001); Hunt et al. (2004); Kastner-Klein et al. (2004) and Belcher (2005) cover further aspects of turbulent flow and dispersion in urban areas that are beyond the scope of the present study. Also, a recent series of reviews in volume 84 of *Theoretical and Applied Climatology* from the Sixth International Conference on Urban Climate (ICUC-6) contains comprehensive bibliographies on street canyon-related urban climate topics such as dispersion (Batchvarova and Gryning, 2006), field observations (Grimmond, 2006), scale modelling (Kanda, 2006) and parameterizations (Masson, 2006).

4.2 Set-up

The design of the present study follows the goals set in the previous section 4.1. Figure 4.2a defines the geometry of the street canyon experiment. (Fig. 4.2b will be discussed later.)

The present street canyon study consists of four parameter studies:

1. Aspect ratio parameter study (Table 4.2)

2. Resolution parameter study (Table 4.3)

3. Local roughness parameter study (Table 4.4)

4. Convective feasibility study (Table 4.5)

All studies feature a single street canyon of fixed width $W = 50$ m in the center of a periodic model domain of horizontal size $(1.92\,W)^2$ in studies 1–3 and $(20\,W)^2$ in study 4. The street canyon height varies according to the canyon aspect ratio H/W listed in Tables 4.2 to 4.5.

Studies 1–3 are neutral without Coriolis force and have a free stream layer above the street canyon. Following Liu et al. (2004), this free stream layer is shallow; here it has a fixed depth of $\delta = 0.5\,W = 25$ m. Although not mentioned by Liu et al. (2004), the reason for this
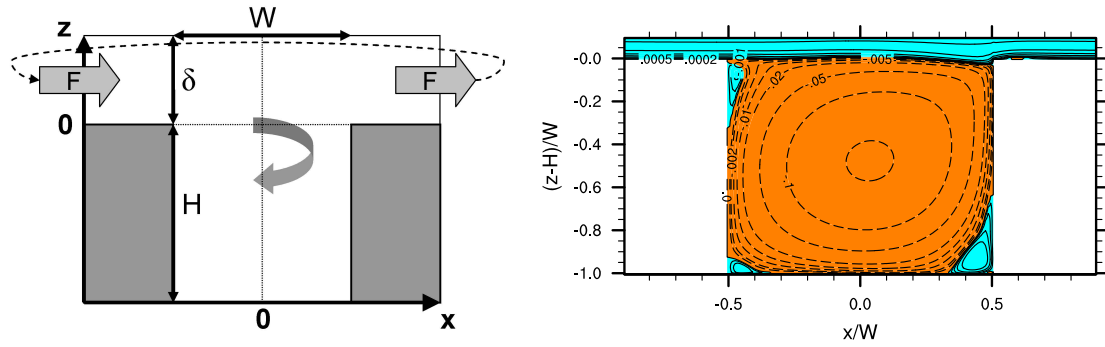
(a) Street canyon geometry.
Abbreviations: H: canyon height; W: canyon width; F: driving force in the free stream layer of depth δ with cyclic streamwise boundary conditions.

(b) Normalized streamfunction for $H/W = 1$. Clockwise rotation is highlighted in red fills – here one single canyon vortex. Anticlockwise rotating vortices are highlighted in light blue – here three corner vortices.

Figure 4.2: Geometry and sample flow topology of the street canyon experiment.

choice of arrangement lies in the time required for the free stream layer to reach equilibrium – this time scales with $\delta^2/\nu_{\text{eff}}$ (Holton, 2004)[1]. For $\delta = 25$ m it is about one hour.

The free stream is driven with a direct body force $F = D_1 = 0.0006$ Pa m^{-1} (cf. subsection 2.4.2 on page 18). A sensitivity study found that this pressure gradient gives the desired bulk velocity of $u_b \approx 1$ m s^{-1}. The free stream Reynolds number is thus $Re_\delta = u_b\delta/\nu_m \approx 10^6$. The model atmosphere is initialised with equation (2.31) in the free stream layer ($u_{z_{\text{ref}}=H} = 0.6$ m s^{-1}, $u_{z_{\text{top}}=H+\delta} = 1.6$ m s^{-1}) and with zero wind speed within the canyon.

The previous paragraph does not apply to cases UB8–UB100, where volume flow conservation at $u_b \equiv 1$ m s^{-1} is applied (Table 4.3, cf. subsection 2.4.2).

The simulation time of studies 1–3 is 3 h; all output data are averaged over the last 2 h.

Study 4 is with Coriolis force. It has a convective boundary layer ($\delta + H \approx 500$ m at simulation end with $H = 25 \ldots 175$ m) with a constant surface heatflux prescribed at the roof and at the street surface, except for the neutral reference case AR0050_H00. The dominant eddies in the CBL are much larger than in studies 1–3. This implies that on the one hand, study 4 requires a much larger horizontal domain size to capture the large, organized convective structures, on the other hand, a coarser resolution is acceptable. The optimal resolution ($R = 32$) and domain size $(20\,W)^2$ have been determined based on an analysis of characteristic vertical profiles and horizontal cross-sections of two sensitivity studies (not shown). Needless to say, the resolution of $R = 32$ means that the level-of-detail within the street canyon is reduced compared to studies 1 and 3 where $R = 100$.

The simulation time of study 4 is 2 h; all output data are averaged over the last 30 min.

---

[1] ν_{eff} is an effective viscosity due to surface friction and the drag that is exerted by the street canyon.

Case	H/W	Case	H/W
AR0015	0.15	AR0290	2.9
AR0025	0.25	AR0300	3.0
AR0050	0.5	AR0310	3.1
AR0060	0.6	AR0320	3.2
AR0100	1.0	AR0340	3.4
AR0120	1.2	AR0360	3.6
AR0140	1.4	AR0400	4.0
AR0180	1.8	AR1000	10.0
AR0200	2.0		

Table 4.2: Aspect ratio parameter study 1 ($R = 100$, $D_1 = 0.0006$ Pa m^{-1}, $z_{0,\text{loc}} = 0.1$ m).

Case	D_1[Pa m^{-1}]	Case	u_b [m s^{-1}]	R
DP8	0.0006	UB8	1	8
DP16	0.0006	UB16	1	16
DP32	0.0006	UB32	1	32
DP40	0.0006	UB40	1	40
DP50	0.0006	UB50	1	50
DP64	0.0006	UB64	1	64
DP80	0.0006	UB80	1	80
DP100	0.0006	UB100	1	100

Table 4.3: Resolution parameter study 2 ($H/W = 3.6$, $z_{0,\text{loc}} = 0.1$ m).

Case	H/W	$z_{0,\text{loc}}$ [m]
AR0050s	0.5	0.01
AR0050r	0.5	0.05
AR0050	0.5	0.1
AR0100s	1.0	0.01
AR0100r	1.0	0.05
AR0100	1.0	0.1
AR0200s	2.0	0.01
AR0200r	2.0	0.05
AR0200	2.0	0.1
AR0360s	3.6	0.01
AR0360r	3.6	0.05
AR0360	3.6	0.1

Table 4.4: Local roughness parameter study 3 ($R = 100$, $D_1 = 0.0006$ Pa m^{-1}).

Case	H/W	Heat flux [K m s^{-1}]
AR0050_H00	0.5	0
AR0050_H01	0.5	0.1
AR0050_H04	0.5	0.4
AR0100_H01	1.0	0.1
AR0200_H01	2.0	0.1
AR0350_H01	3.5	0.1

Table 4.5: Convective feasilibity study 4 ($R = 32$, $z_{0,\text{loc}} = 0.1$ m).

Abbreviations:

H/W: aspect ratio of canyon height H divided by width W; R: Resolution in grid points per canyon width; D_1: direct body force in x-direction; $z_{0,\text{loc}}$: local roughness length applied at all walls; u_b: bulk velocity in the free stream layer.

4.3 Calculation of higher-order turbulent statistics

Traditionally, in LES of the horizontally homogeneous atmospheric boundary layer the higher-order (≥ 2) turbulent statistics are computed from turbulent fluctuations that are conveniently defined as *spatial fluctuations*, i.e. as a deviation from the (instantaneous) horizontal mean.

This paradigm does not hold in complex geometry flows such as urban LES. In a 2D street canyon the canyon axis still offers one dimension of spatial homogeneity, however, this is generally not the case in real complex urban geometries. Then the only possible way is to define turbulent fluctuations as *temporal fluctuations*, i.e. as a deviation from the (local) temporal mean.

However, since the temporal mean of a quantity is only known at the end of the averaging period, this would require data from all time steps (of the averaging period) to be stored until that time has been reached. Thereafter, calculation of turbulent fluctuations could take place in a post-processing step. Two extreme examples illustrate that this may not always be feasible:

Study 1:   During its 2 h averaging period run AR1000 would produce $3.9 \cdot 10^7$ grid points $\times\ 3.4 \cdot 10^4$ time steps $\times$ 4 byte $\times$ 5 variables (e.g., u, v, w, θ, s) $= 2.7 \cdot 10^{13}$ byte $= 24$ TB.

Study 4:   During its 30 min averaging period run AR0040_04 would produce $1.4 \cdot 10^8$ grid points $\times\ 1.1 \cdot 10^4$ time steps $\times$ 4 byte $\times$ 5 variables $= 3.1 \cdot 10^{13}$ byte $= 28$ TB.

The data volume is so large that it can neither be kept in machine memory nor efficiently output on file.

One obvious solution is to reduce the data volume to only selected time steps and only selected 1D profiles or 2D cross-sections instead of 3D volume data.

However, turbulence statistics defined through Reynolds decomposition allow an elegant alternative solution. Consider, as an example, the time-averaged resolved-scale second-order moment $\overline{\phi'\psi'}$ in eqn. (2.11) on page 9. $\overline{\phi'\psi'}$ may constitute a turbulent flux or a variance if $\phi = \psi$. ϕ' and ψ' are unknown until the end of the averaging period, however, both other terms in eqn. (2.11), $\overline{\phi\psi}$ and $\overline{\phi}\,\overline{\psi}$, can easily be computed on-the-fly by stepwise summation over all time steps during the averaging period and a final division by the number of time steps. This comes at a relatively small expense of machine memory: to obtain $\overline{\phi'\psi'}$, three 3D arrays are required for summation: ϕ and ψ, and one extra array summing their instantaneous products $\phi\psi$.

This approach was adopted for the street canyon parameter study. Its advantages are that higher-order moments contain contributions from all time steps, that they are available at each single grid point, and that they are computed in a computationally highly efficient manner with minimal post-processing. Its disadvantages are that only the temporal averages of higher-order moments can be calculated this way, and that more complicated expressions (for example 3rd- or 4th-order moments, or normalization of turbulent quantities with nonlinearly correlated other quantities) may require summation of many more arrays.

4.4 Basic topology and dynamic driving mechanism of street canyon flow

Before the results of the parameter studies 1–4 will be presented in the following section 4.5, the present section uses case AR0100 as an introductory example to explain the basic

43

topology of street canyon flow and to investigate its dynamic driving mechanism. Case AR0100 represents the skimming flow regime (SF1); it features the *regular canyon* that has been intensively studied in literature.

Figure 4.2b on page 41 shows the streamfunction ψ computed from the 2D flow in the xz-plane (spanwise and temporal average denoted by angle brackets $\langle\rangle$ and an overbar) by integration of

$$\frac{\partial\psi}{\partial z} = \langle\overline{u}\rangle \qquad \text{and} \qquad \frac{\partial\psi}{\partial x} = -\langle\overline{w}\rangle \,. \tag{4.1}$$

The streamfunction is normalized with the bulk velocity u_b and the canyon width W. Clockwise (anticlockwise) rotation for negative (positive) ψ is highlighted in red (light blue). The street canyon flow topology exhibits vortices of significantly different strength; in the present study the local extrema of ψ span at least two orders of magnitude. In order to visualize weak and strong vortices equally well within a single plot, Fig. 4.2b and all following streamfunction plots use pseudo-logarithmic contour values (0 and $\pm 1, 2, 5 \cdot 10^n$, starting from $+0.0002$ and -0.001, respectively).

As expected from literature for aspect ratio $H/W = 1$, a single clockwise rotating vortex fills the entire canyon. Its center is shifted slightly in positive x- and z-direction in agreement with the single canyon water channel experiment of Baik et al. (2000) and the horizontally periodic LES of Cui et al. (2004) and Liu et al. (2004). The single cavity wind tunnel experiment of Kovar-Panskus et al. (2002b) shows a stronger shift in positive x-direction only, while the one of Caton et al. (2003) shows a slight upward shift only.

Note that transition effects due to upstream roughness changes (for a review see Smits and Wood, 1985) hinder a direct comparison of the present periodic canyon with isolated canyons (Kastner-Klein et al., 2001, 2004; Bohnenstengel et al., 2004) and at least the first three of a row of canyons (Brown et al., 2000). For the same reason a direct comparison with single cavities may fail.

Three very small and weak, anticlockwise rotating vortices are also discernible in Fig. 4.2b, two in the bottom corners and one near the top of the leeward wall (just below the upstream flow separation). The former are observed in most models listed in Table 4.1 given a sufficient spatial grid resolution, but the latter is generally reproduced only by LES and DNS models.

The corner vortices have first been postulated by Moffatt (1964) on theoretical grounds for the viscous limit of Stokes flow ($Re = 0$). Arguably, shear-driven street canyon flow and lid-driven cavity flow share a similar flow topology near the bottom, far away from their respective forcing; the review by Shankar and Deshpande (2000) shows how these corner vortices increase their size and strength when $Re \to \infty$ in a driven cavity.

The mean free stream flow appears almost undisturbed by the underlying canyon judging from the parallel alignment of streamfunction contours at and above roof level, which means that case AR0100 indeed belongs to the skimming flow regime. This finding is also supported by Meroney et al. (1996).

One of the most interesting features of street canyon flow is the *turbulent shear layer* that drives the skimming flow canyon recirculation. Many scale model and most numerical studies including the present one model the canyon geometry with just flat roofs and thus produce a strong turbulent shear layer at or just above roof level.[2]

In wind tunnel experiments with both flat and pitched roofs Louka et al. (2000) and Caton et al. (2003) found the canyon recirculation quite *intermittent* – contrary to the conventional

---

[2]In case of pitched roofs this shear layer is elevated and modified – cf. Rafailidis (1997, 2000); Louka et al. (1998); Barlow and Pascheke (2006) – so that the canyon vortex may not form at all (Kastner-Klein et al., 2004). Field studies of Christen (2005) and Eliasson et al. (2006) in real pitched roof canyons were able to detect a canyon recirculation.
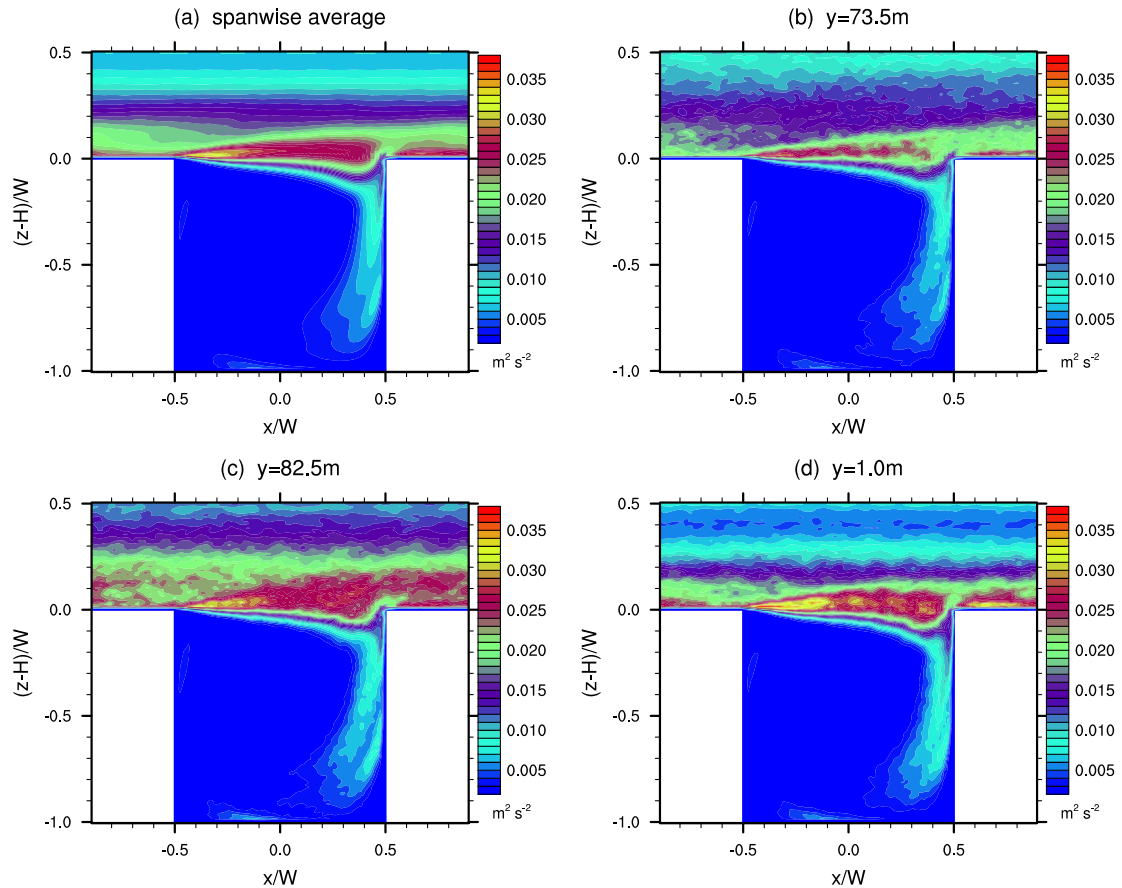
Figure 4.3: Cross-sections of time-averaged turbulent kinetic energy (TKE) for case AR0100 ($H/W = 1$).

picture of skimming flow with a steady canyon vortex; they suggested mixing layer concepts to describe the turbulent exchange at roof level. Meroney et al. (1996), however, found the "urban canyon vortex" (conventional skimming flow) much less intermittent than the "rural canyon vortex" (skimming flow with upstream roughness change). Santos et al. (2005) observed a clear effect of large-scale convective turbulent motion on intermittency. The present study now addresses the shear layer and its intermittency.

Figure 4.3a displays the time- and spanwise averaged resolved-scale turbulent kinetic energy (TKE) for case AR0100. Peak TKE values occur at roof level. A branch of high TKE extends downward along the windward wall in agreement with Brown et al. (2000) and Caton et al. (2003).

Louka et al. (2000) analysed the individual budget terms of the TKE equation and demonstrated that the peak TKE layer at roof level is associated with the turbulent shear layer shed from the upwind roof. They concluded that this shear layer becomes unstable through Kelvin-Helmholtz instabilities and postulated that its depth increases across the canyon following the mixing-layer analogy of vegetation canopies (Raupach et al., 1996; Finnigan, 2000). (A *plane mixing layer* is a shear layer that develops at the interface of two co-flowing streams of different speed; the corresponding velocity profile shows one characteristic inflection point, see Figure 4.4a).

Figure 4.3 shows that the depth of the peak TKE layer indeed increases with downstream distance, just as it would also be expected in a plane mixing layer (e.g., Pope, 2000; Schlicht-

(a) Plane mixing layer

(c) Cavity shear layer

(b) Plane wake
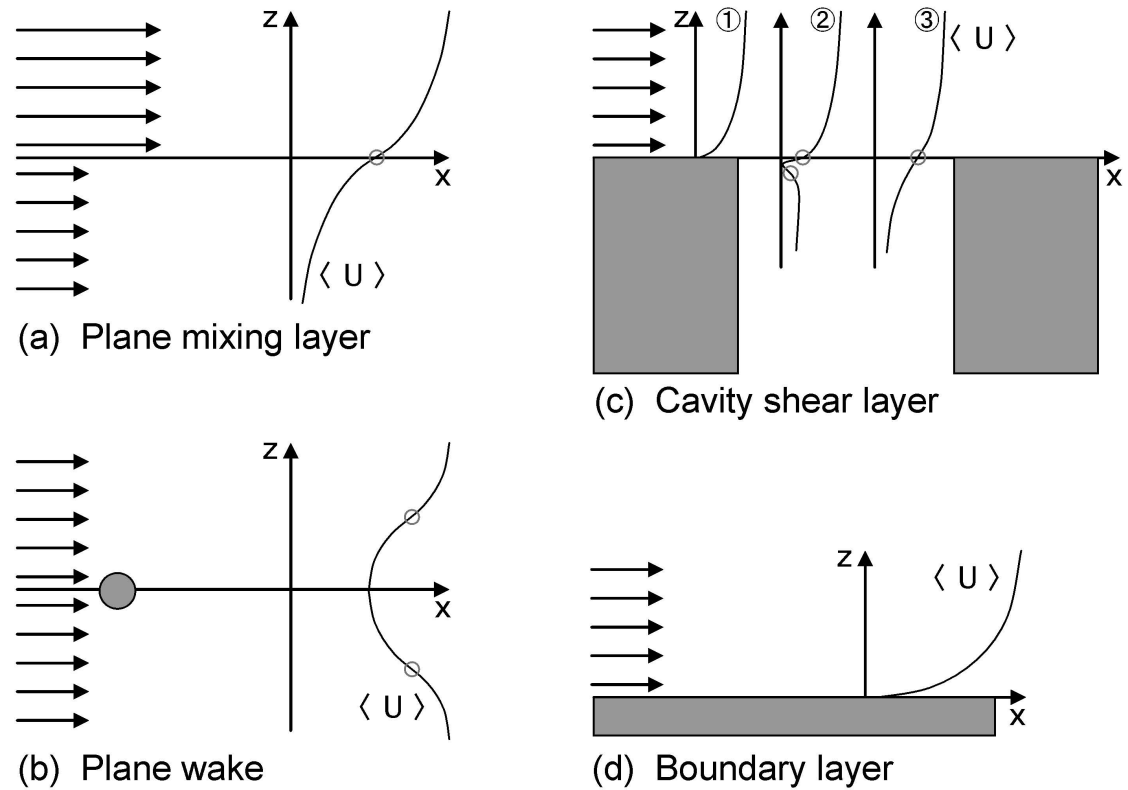
(d) Boundary layer

Figure 4.4: Sketches of free shear layers with their characteristic vertical profile(s) of streamwise velocity: (a) Plane mixing layer, (b) Plane wake, (c) Cavity shear layer, (d) Boundary layer. Grey circles indicate inflection points. In (c), encircled numbers ①–③ indicate profiles at distinct streamwise positions (see text for details). (a), (b), and (d) are modified after Pope (2000).

ing and Gersten, 2006).

Temporal fluctuations of TKE would be useful for investigation of intermittency, but they are not available in the present study (cf. section 4.3). Instead, *local* cross-sections of time-averaged TKE are shown in Fig. 4.3b-d at three different y-positions. They demonstrate the spanwise variability of the peak TKE layer in terms of its strength, structure and inclination, which is also contrary to the conventional skimming flow picture.

One apparent detail in Fig. 4.3 requires further discussion: the streamwise position of maximal TKE in the canyon is close to the upwind roof, in agreement with some studies (Baik and Kim, 1999; Liu and Barth, 2002; Li et al., 2005) but contrary to others (Walton and Cheng, 2002; Caton et al., 2003). Kim and Baik (2003) demonstrated that two local TKE maxima exist at roof level, one near the upwind roof and one near the downwind roof, and that the level of inflow turbulence intensity determines the absolute maximum.

The present study found a dependence of this position on grid resolution for cases DP8–DP100 of the resolution parameter study 2 that are comparable with AR0100 because they also belong to the skimming flow regime. At moderate resolution ($R = 32 \ldots 40$) the TKE maximum occurs near the downstream roof, however, it shifts to the upstream roof at higher resolution ($R = 50 \ldots 100$). Indeed, the yellow-coloured maximal TKE layer in Fig. 4.3a at $x/H = -0.45 \ldots -0.2$ is so thin that even with $R = 100$ it can be resolved by 3–4 grid points only; this implies that simulations with $R < 50$ inherently cannot resolve it. This example stresses the importance of high-resolution simulations (and measurements) in complex geometry flows. The following discussion will explain why the streamwise position

of maximal TKE indeed depends on the grid resolution.

In order to investigate why the TKE maximum occurs near the upstream roof it is intuitive to consider streamwise velocity $\langle \bar{u} \rangle$ and its vertical shear $\partial \langle \bar{u} \rangle / \partial z$ shown in Figure 4.5. $\langle \bar{u} \rangle$ is horizontally fairly uniform in the free stream layer, but it shows large variability in the canyon both in the streamwise and in the vertical direction due to the canyon vortex. The slight asymmetry of this vortex (Fig. 4.2b) together with the weak roof level corner vortex at $x/W = -0.5$ explain the asymmetric distribution of $\langle \bar{u} \rangle$ and $\partial \langle \bar{u} \rangle / \partial z$ in the canyon region just below roof level. At roof level a layer of strong positive shear $\partial \langle \bar{u} \rangle / \partial z$ is shed from the building roof and extends across the canyon. (Note that the higher the grid resolution, the larger are the shear and hence the TKE above the roof.) The contour $\partial \langle \bar{u} \rangle / \partial z = +0.2 \text{ s}^{-1}$ extends up to $x/H = -0.2$, which coincides with the horizontal extent of the yellow-coloured maximal TKE layer in Fig. 4.3a. The TKE budget term analysis of Louka et al. (2000) showed that at canyon roof level the TKE production term $-\overline{w'u'} \cdot \partial \langle \bar{u} \rangle / \partial z$ dominates the TKE equation. As will be shown in subsection 4.5.2.2, $-\overline{w'u'}$ peaks at roof level. This means that maximal TKE production occurs at roof level especially at $x/H = -0.5 \ldots -0.2$, which is the explanation for the TKE maximum near the upstream roof at high grid resolution.

The strong shear layer atop the canyon is equivalent to the existence of an inflection point in the vertical profile of streamwise velocity at roof level (Fig. 4.4a; such profiles will be shown in subsection 4.5.2.1). This means that the mixing-layer analogy is indeed applicable here as postulated by Louka et al. (2000). Note that no inflection point exists in the classical boundary layer that develops over the building (Fig. 4.4d).

However, actually there is a second shear layer at $x/H = -0.5 \ldots 0.0$ just below roof level at $(z - H)/W \approx 0.0 \ldots -0.2$ in Figure 4.5b. The shear here is about an order of magnitude weaker – and negative. This second shear layer implies the existence of a second inflection point. Indeed, vertical profiles of streamwise velocity with two inflection points near the leeward canyon wall are frequently observed, for example in the field study of Eliasson et al. (2006), the wind tunnel experiment of Kovar-Panskus et al. (2002a), LES of Liu and Barth (2002), Cui et al. (2004) and the present study and RANS of Kim and Baik (2001) and Xie et al. (2006). The question is whether this requires a refinement of the mixing-layer analogy. Since this shear layer is slanted, the vorticity needs to be considered to answer this question.

Figure 4.6 shows spanwise vorticity

$$\bar{\zeta}_y = \frac{\partial \overline{w}}{\partial x} - \frac{\partial \overline{u}}{\partial z} \tag{4.2}$$

at the same cross-section positions as in Fig. 4.3. The result well agrees with the vorticity measured by Caton et al. (2003).[3] The strong shear layer at roof level (Fig. 4.5b) now appears as a layer of large negative vorticity, while the weaker shear layer just below it spirals around the vortex core. Strictly speaking, the second inflection point means that flow in the canyon roof region should be described as a superposition of *two* shear flow regimes: a weak *plane wake* (Fig. 4.4b; cf. again Pope, 2000; Schlichting and Gersten, 2006) superimposed on the dominant *plane mixing layer*. The resulting new regime may be called a *cavity shear layer*, as depicted in Figure 4.4c. The sketch shows the three stages in the streamwise boundary layer transition: ① the classical boundary layer without inflection points over the upstream building, ② a region with two inflection points near the leeward canyon wall and ③ the mixing layer near the windward canyon wall with only one inflection point.

The region with two inflection points ② should theoretically produce two distinct levels of strong and weak shedding of Kelvin-Helmholtz waves with opposite rotation (cf. Lugt, 1983;

---

[3]Cf. subsection 2.2.2 on page 11 concerning the $2 \Delta x$ oscillations at $(z - H)/W = 0$ that originate from the building corner at $x/W = +0.5$.
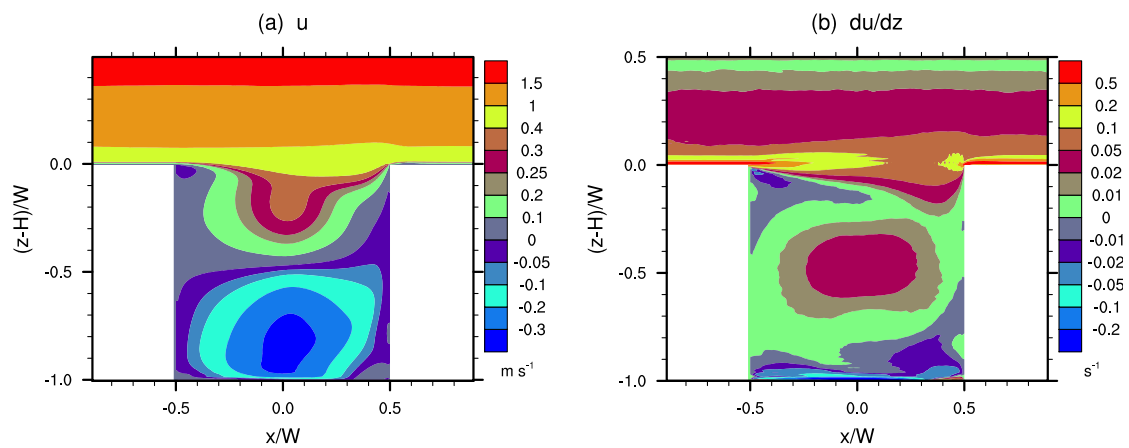
Figure 4.5: Cross-sections of time- and spanwise averages of (a) streamwise velocity $\langle \bar{u} \rangle$ and (b) its vertical shear $\partial \langle \bar{u} \rangle / \partial z$ for case AR0100.
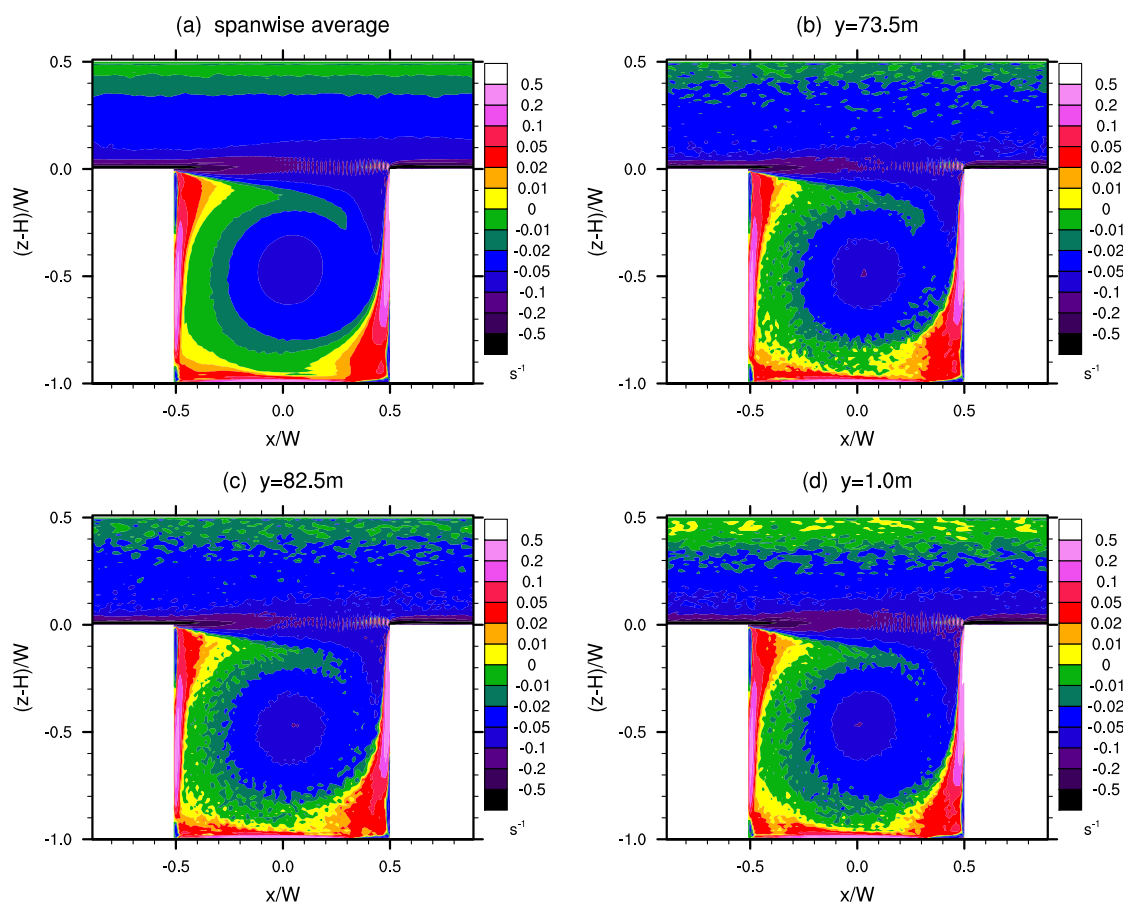
Figure 4.6: Cross-sections of time-averaged spanwise vorticity $\bar{\zeta}_y$ at the same positions as in Figure 4.3.
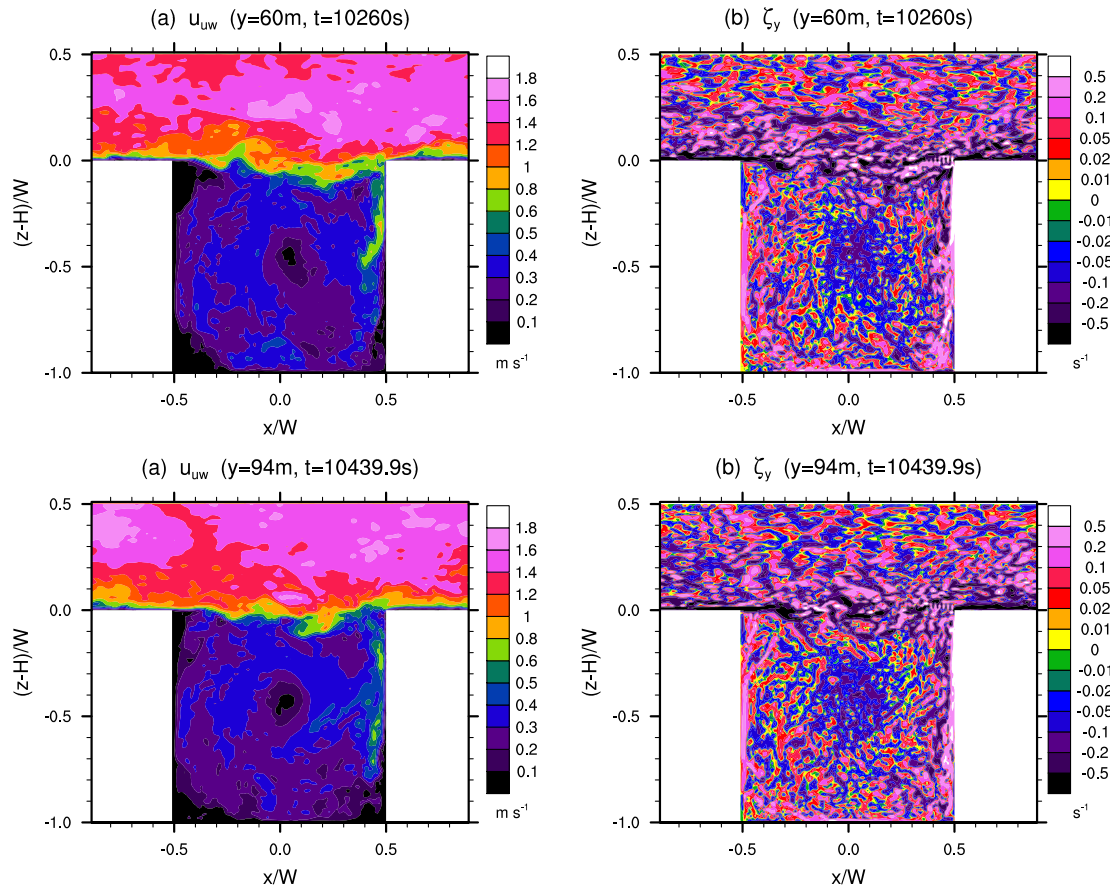
Figure 4.7: Flow snapshot cross-sections of (a,c) absolute velocity u_{uw} in the xz-plane and (b,d) corresponding spanwise vorticity ζ_y at selected output times and spanwise positions for case AR0100.

Lesieur, 1997; Wu et al., 2006). However, since a) shear in the weak shear layer is about an order of magnitude smaller than in the strong shear layer, since b) the weak shear layer is quite shallow, and since c) in high Reynolds number flows Kelvin-Helmholtz instabilities are easily "masked" by superposition of strong turbulence (Breuer, 2002), the plane wake may not be discernible in practice.

In fact, instantaneous velocity snapshots that do resemble Kelvin-Helmholtz waves were difficult to find. Figure 4.7a,c shows two such events. The corresponding spanwise vorticity in Fig. 4.7b,d is dominated by small-scale turbulence, however, a strong shear layer spanning the entire model domain at and just above roof level is still discernible (like in the DNS cube study of Coceal et al., 2006), as are the Kelvin-Helmholtz waves. This is the first LES study that could demonstrate the existence of Kelvin-Helmholtz instabilities atop an urban street canyon.

Kelvin-Helmholtz instabilities can also be found in the shear layer visualization by Caton et al. (2003, Fig. 2) using snapshots of passive particle concentration, although they did not explicitly identify them as such. Using wavelet analysis, Cui et al. (2004) attributed the dominant time scale in the shear layer to eddies that would typically be produced by Kelvin-Helmholtz instabilities. Note that a strong shear layer is also apparent in the laboratory water flume visualization experiments by Khan et al. (2005a,b, 2006). For a discussion on how the shear layer dynamics and orientation change with geometry (e.g. in shallow or deep canyons) refer to Harman et al. (2004) and Belcher (2005).

49

Case	$\bar{\zeta}_{y,\mathrm{min,W}}$	$\bar{\zeta}_{y,\mathrm{min,H}}$	Case	$\bar{\zeta}_{y,\mathrm{min,W}}$
AR0015	-0.02	-0.13	AR0290	-0.13
AR0025	-0.05	-0.20	AR0300	-0.14
AR0050	-0.12	-0.24	AR0310	-0.13
AR0060	-0.12	-0.20	AR0320	-0.14
AR0100	-0.21		AR0340	-0.14
AR0120	-0.19		AR0360	-0.14
AR0140	-0.17		AR0400	-0.14
AR0180	-0.15		AR1000	-0.14
AR0200	-0.15			

Table 4.6: Minimal streamfunction values of the upper canyon vortex for study 1 normalized by u_b and canyon width W or height H.

To conclude this section, there is now sufficient evidence to confirm the argument of Louka et al. (2000) that the conventional skimming flow picture of a steady canyon recirculation should be revised in a sense that the driving shear layer is unsteady due to shedding of Kelvin-Helmholtz waves, which renders also the canyon recirculation highly intermittent. Furthermore, the concept of a *cavity shear layer* was developed that inserts an extra region near the leeward canyon wall with two inflection points (Figure 4.4c ②) between the boundary layer over the building and the plane mixing layer further downstream.

4.5 Parameter study results

4.5.1 Mean flow topology

This subsection investigates possible dependencies of the mean street canyon flow topology on the parameters varied in studies 1–3: canyon aspect ratio H/W, grid resolution R, driving force F and local wall roughness $z_{0,\mathrm{loc}}$. As in Figure 4.2b on page 41 the cross-section of the streamfunction $\bar{\zeta}_y$, normalized with the bulk velocity u_b and the canyon width W, will be discussed in the following.

Figures 4.8 and 4.9 show the topology of mean street canyon flow for cases AR0015–AR1000 of the *aspect ratio parameter study 1* (Table 4.2). Skimming flow exists for all cases except AR0015 that shows wake interference flow. AR0015 has the lowest aspect ratio of all cases. The skimming flow regime with one canyon vortex (SF1) is observed for $H/W = 0.25 \ldots 2$; two vortices (SF2) are observed for $H/W = 2.9 \ldots 4$. The three-vortex regime (SF3) could not be observed; even case AR1000 with $H/W = 10$ (a generalization of the very deep canyons in the Hong Kong study in chapter 6) appears to belong to SF2 rather than to any other regime.

Judging from some RANS model results in Table 4.1 a transition from SF2 to SF3 could have been expected at $H/W \gtrsim 3$, which is why study 1 focussed on the aspect ratio range $H/W = 2.9 \ldots 4$. The water tank experiment of Baik et al. (2000) showed two vortices (SF2) for $H/W = 3$. Similarly, no third vortex could be identified in the wind tunnel experiment of Kovar-Panskus et al. (2002a) for $H/W = 3.3$ because the measured velocities in the lowest part of the cavity were too low. This suggests that the SF3 regime may be a numerical artefact of RANS models. So far no other LES or DNS have investigated such deep canyons, except for Leonardi et al. (2003) who did not investigate the number of vortices.

Table 4.6 lists the minimal streamfunction values $\bar{\zeta}_{y,\min}$ in the core of the upper canyon vortex for cases AR0015–AR1000. They are a measure of the strength of the clockwise recirculation. $\bar{\zeta}_{y,\min,W}$ is normalized by canyon width W as are the cross-sections in Figures 4.8 and 4.9. The recirculation is strongest in regular canyons (AR0100, AR0120) and drops to an almost constant value of -0.14 for deep canyons (AR0180–AR1000). In fact, subsection 4.5.2 will reveal that all these deep canyons share similar turbulence properties.

For aspect ratio $H/W < 1$, the canyon recirculation is limited in size by canyon height, so that H is a more suitable length scale for normalization, therefore Table 4.6 also lists the values of $\bar{\zeta}_{y,\min,H}$ for cases AR0015–AR0060. $\bar{\zeta}_{y,\min,H}$ values are comparable to $\bar{\zeta}_{y,\min,W}$ for $H/W = 1$. The only exception is case AR0015 that belongs to the wake interference regime.

As a summary of Table 4.6, cases AR0025–AR0140 and AR0180–AR1000, respectively, may be grouped together in terms of canyon recirculation strength.

Cases AR0050 and AR0100 agree qualitatively well with the LES study of Liu et al. (2004). However, $\bar{\zeta}_{y,\min,H}$ deviates from their peak streamfunction values, -0.16 (AR0050) and -0.097 (AR0100). Case AR0200 is on the border between SF1 and SF2[4], whereas Liu et al. (2004) clearly show two vertically aligned canyon vortices for this aspect ratio.

These differences may be partly due to differences in the flow configurations adopted. Liu et al. (2004) obtained the aspect ratios $H/W = 0.5$ (2.0) by doubling W (H) compared to case AR0100 and used a free-stream layer depth $\delta = 0.5 \min(H,W)$. This means that the free-stream layer depth is not consistent with the present study where W and $\delta = 0.5W$ were always kept constant and only H was varied. Also, Liu et al. (2004) used a wall-resolving LES with smooth walls contrary to the present study with modelled rough urban wall effects $(z_{0,\text{loc}} = 0.1 \text{ m})$.

Figures 4.10 and 4.11 show the topology of mean street canyon flow for cases DP8–DP100 and UB8–UB100 of the *resolution parameter study 2* (Table 4.3). Cases with low resolution R=8 can be excluded qualitatively because they fail to reproduce the lower vortex. Resolution convergence starts at DP32 and UB32 for the upper vortex and at DP80 for the lower vortex. For cases UB8–UB100 the circulation in the lower canyon half does not converge with resolution, possibly due to an insufficient averaging time. This suggests that a constant pressure gradient (DP8–DP100) is a more suitable driving mechanism for this problem than a constant volume flow (UB8–UB100). Studies 1 and 3 thus apply a constant pressure gradient and use a high resolution of R=100.

In order to test whether the flow topology depends on the magnitude of the driving force F one simulation with $F = D_1 = 0.002$ Pa m^{-1} has been performed where the bulk velocity was approximately double the value of all other cases ($u_b \approx 2$ m s^{-1}). The flow topology (not shown) agreed qualitatively and quantitatively very well with case DP100, which indicates that the flow is independent of u_b. This was expected because Meroney et al. (1996) and Pavageau and Schatzmann (1999) showed a *Reynolds number independence* for $Re_H = u_H \cdot H/\nu_m \gtrsim 3400$ – the slightly differently defined free-stream Reynolds number $Re_\delta = u_b \cdot \delta/\nu_m \approx 10^6$ in studies 1–3 of the present study is far off this critical limit.

Figure 4.12 shows the topology of mean street canyon flow for the "smooth" ("s": $z_{0,\text{loc}} = 0.01$ m) and "rougher" cases ("r": $z_{0,\text{loc}} = 0.05$ m) of the *local roughness parameter study 3* (Table 4.4). This is to be compared to "rough" cases with default roughness $z_{0,\text{loc}} = 0.1$ m in Figs. 4.8c,e, 4.9a and 4.10h. At first sight, there is surprisingly little difference between the different roughnesses. There is only a general tendency of a strengthening upper vortex recirculation with decreasing roughness, which is associated with smaller lower

---

[4]Only an intermittent, unstable second vortex could be observed (not shown) – like in the field observations of Eliasson et al. (2006) in an urban street canyon of aspect ratio 2.1.
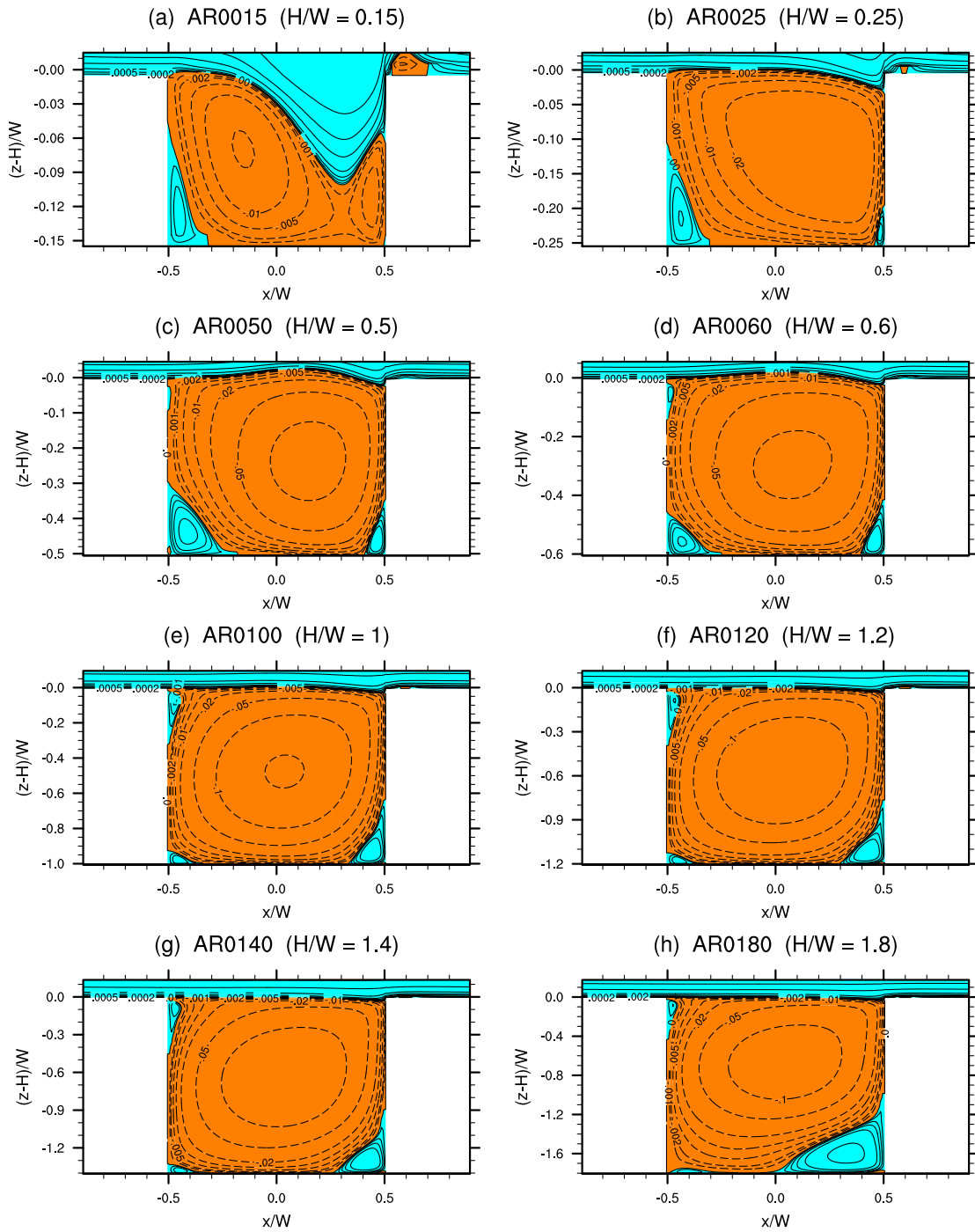
Figure 4.8: Mean flow topology for aspect ratio $H/W = 0.15 \dots 1.8$.
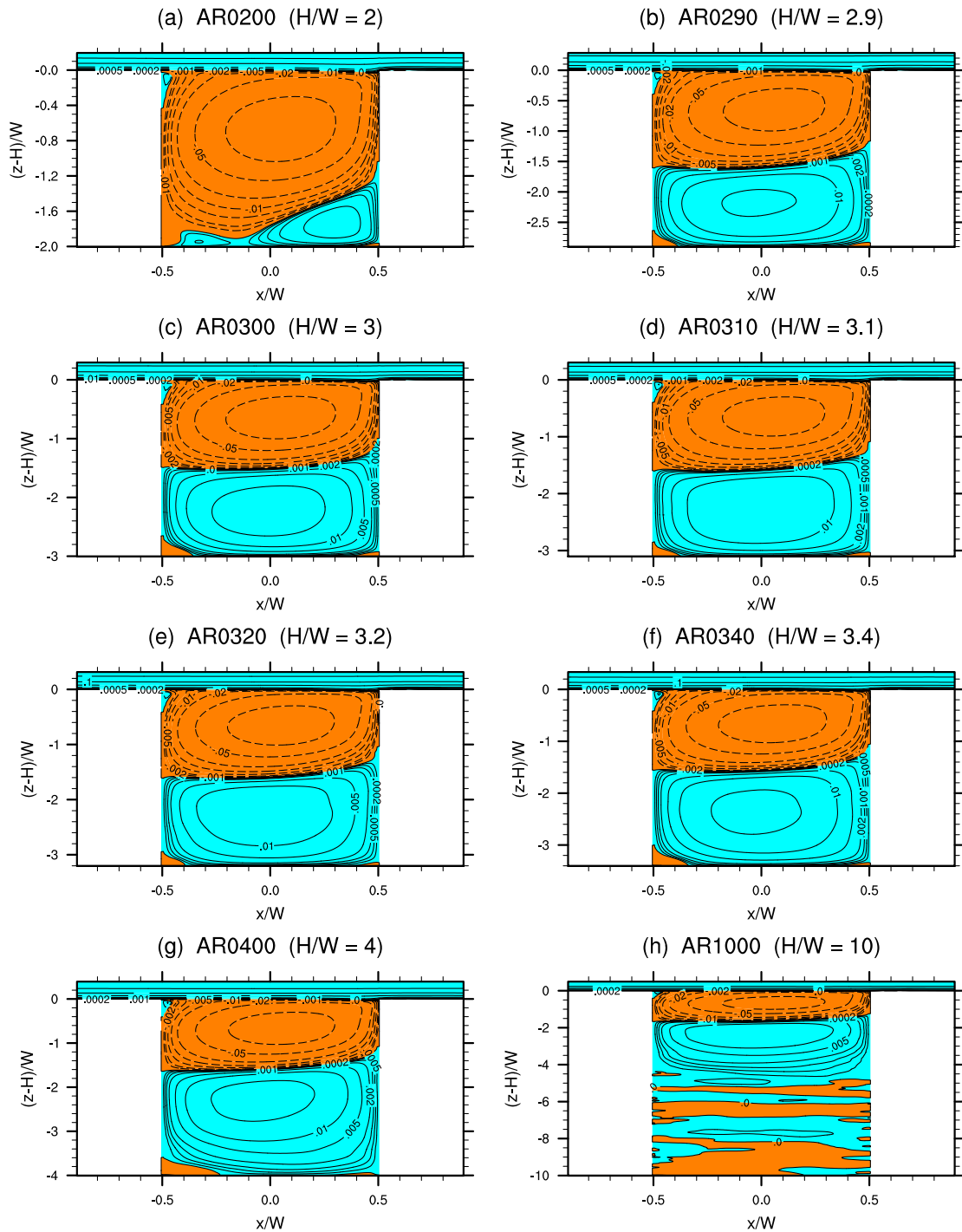
Figure 4.9: Mean flow topology for aspect ratio $H/W = 2.0 \ldots 10.0$.
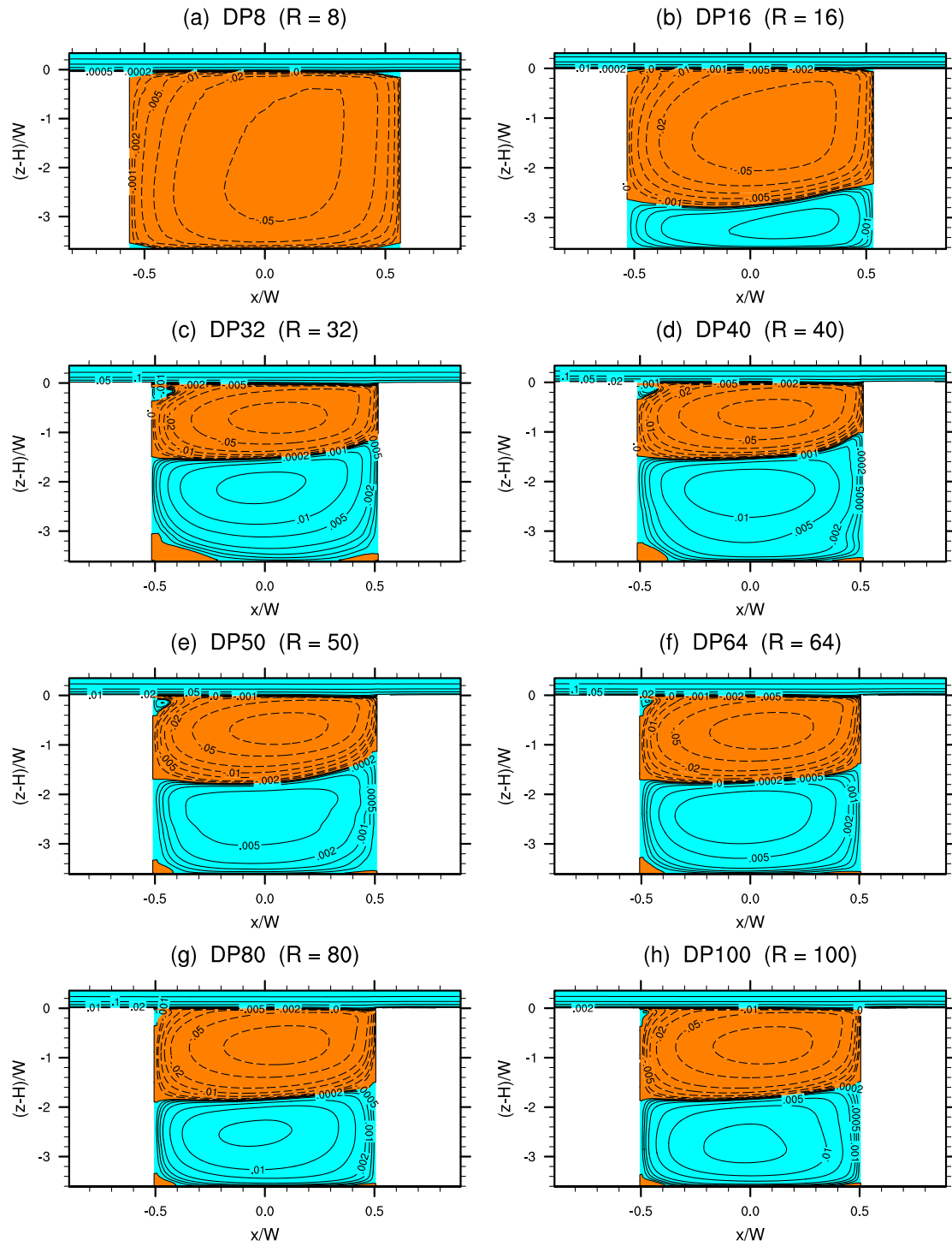
Figure 4.10: Mean flow topology for grid resolution $R = 8 \ldots 100$ driven by a constant pressure gradient.
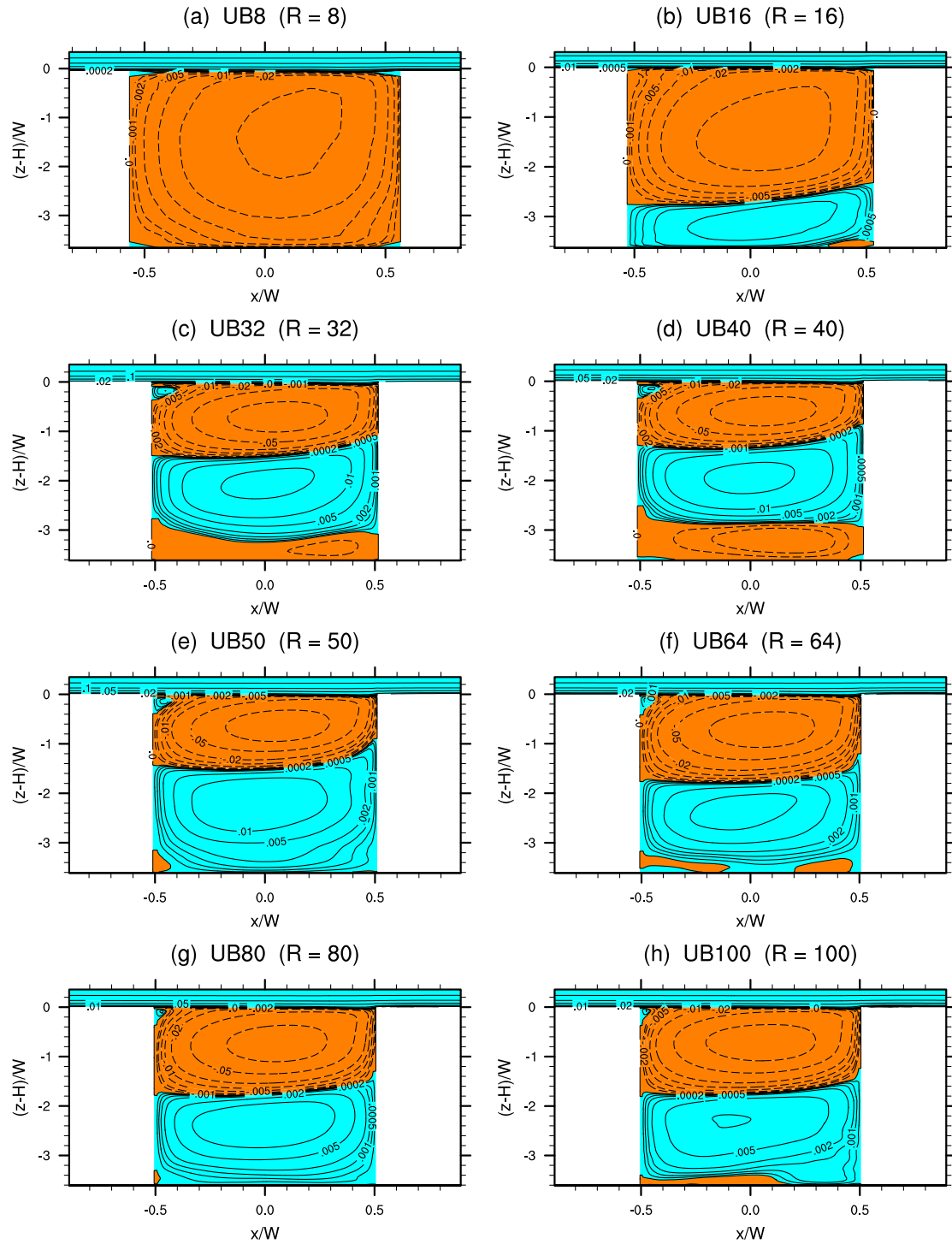
Figure 4.11: Mean flow topology for grid resolution $R = 8 \ldots 100$ driven by a constant volume flow.
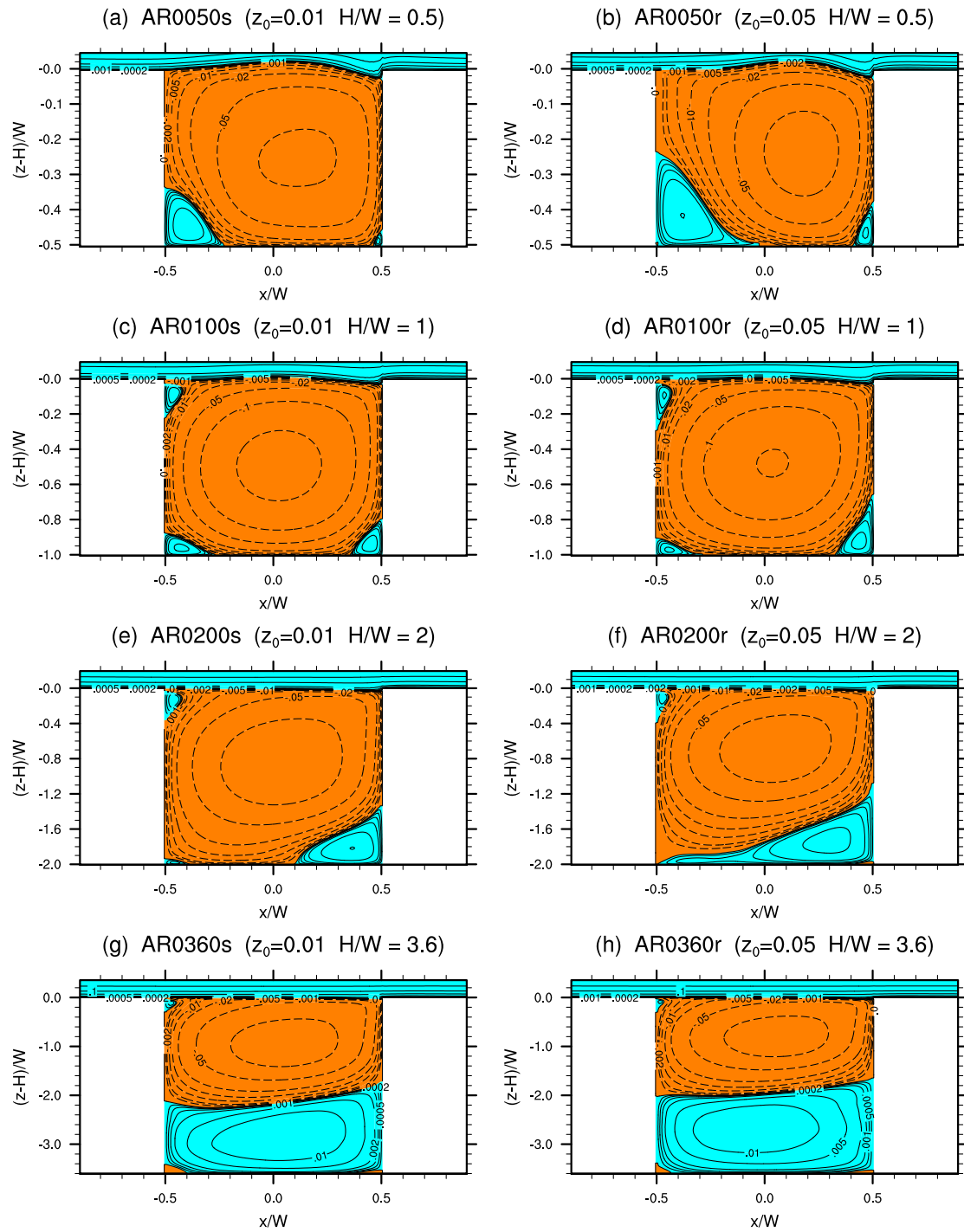
Figure 4.12: Mean flow topology for local wall roughness $z_{0,\mathrm{loc}}$=0.01…0.05 and canyon aspect ratio $H/W = 0.5…3.6$.

corner vortices; but even this tendency is not very clear for all aspect ratios. However, more subtle differences will become apparent in the following subsection.

4.5.2 Integral statistics

This subsection presents integral turbulence statistics and thus complements the previous subsection. It investigates possible dependencies of the integral statistics on the parameters varied in studies 1 and 3: canyon aspect ratio H/W and local wall roughness $z_{0,\text{loc}}$. Except for the following first two figures, the integral statistics will be averaged in both streamwise and spanwise direction, denoted by square brackets $[\,]$.

4.5.2.1 Mean wind

Figure 4.13 shows classical cavity profiles for different canyon aspect ratios: in red the vertical profile of normalized streamwise velocity $\langle \bar{u} \rangle / u_{\text{H}}$ at canyon center x/W $= 0$ and in blue the streamwise profile of normalized vertical velocity $\langle \bar{w} \rangle / u_{\text{H}}$ at canyon midheight $(z - H)/H = -0.5$. These two quantities are often plotted together like this in one panel in order to highlight basic asymmetries of the flow of regular cavities with aspect ratio H/W=1 (cf. Shankar and Deshpande, 2000).

This complex figure is now introduced step-by-step:

1. The *regular canyon* profiles (H/W=1) are shown as thick solid lines. $\langle \bar{u} \rangle$ is asymmetric about the canyon midheight; one can clearly see the influence of the shear layer atop the canyon and identify the second inflection point at (z-H)/H=-0.15 as postulated in section 4.4.
   $\langle \bar{w} \rangle$ is asymmetric about the streamwise canyon center; the downdraft locally intensifies in a narrow region close to the windward wall at x/W=0.35...0.5.
   These findings are in good agreement with Cui et al. (2004).

2. *Shallow canyon* profiles (H/W $\leq$ 0.6) of $\langle \bar{u} \rangle$ are roughly similar to the regular canyon but with reduced vertical shear. This is because their free-stream layer depth $\delta = 0.5W$ is now quite large compared to the canyon height H; in other words the dominant turbulent eddies are relatively large.

3. *Deep canyon* profiles ($H/W \geq 1.8$) of $\langle \bar{u} \rangle$ show a striking self-similarity in terms of both shape and magnitude of the velocity minimum. Only the vertical scaling with canyon height H appears inappropriate. Hence this study will try a scaling with canyon width W (see below) as suggested by Roth (2000).

4. $\langle \bar{w} \rangle$ profiles show various patterns and cannot easily be grouped. This is because the canyon midheight is not a characteristic level of w in deep canyons. Hence this study will evaluate $\langle \bar{w} \rangle$ profiles at different heights (see below).

The above discussion suggests that the classical cavity profiles are not well suited for non-regular canyons. Figure 4.14 shows this study's attempt to solve the problems just mentioned using modified cavity profiles of $\langle \bar{u} \rangle$ and $\langle \bar{w} \rangle$:

1. All $\langle \bar{u} \rangle$ profiles are now vertically scaled in units of canyon width W. For clarity, the profiles are only plotted to a maximal depth of $(z - H)/W = -4$. Now, profiles with aspect ratio $H/W \geq 2$ all collapse to a single profile. The other profiles show a similar shape but appear to scale with canyon height H.
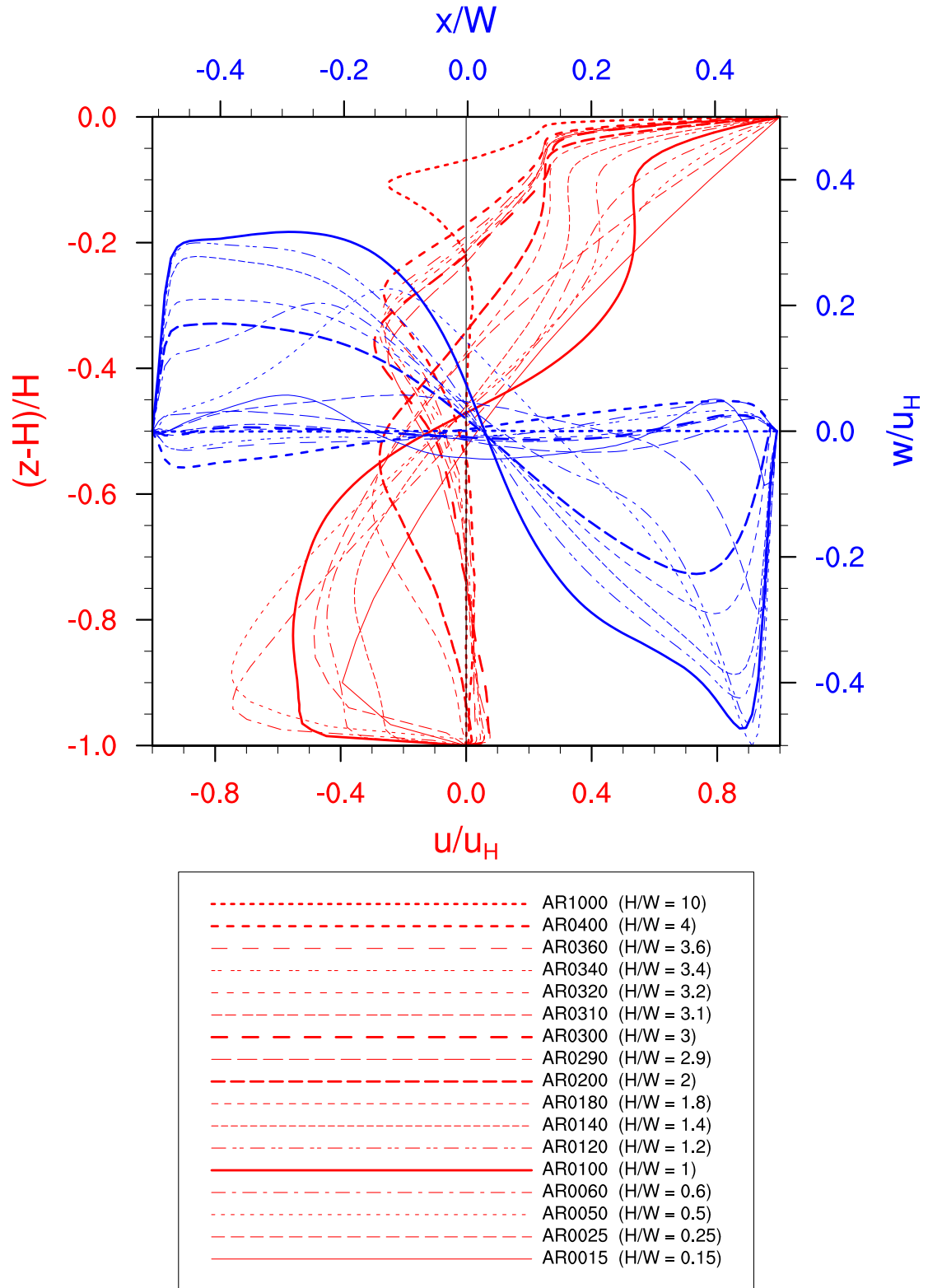
Figure 4.13: Classical cavity profiles for different canyon aspect ratios.
Red: vertical profile of streamwise velocity $\langle \bar{u} \rangle / u_H$ at canyon center $x/W = 0$; blue: streamwise profile of vertical velocity $\langle \bar{w} \rangle / u_H$ at canyon midheight $(z - H)/H = -0.5$. Both are normalized with the streamwise velocity at roof height H and at canyon center $x/W = 0$.
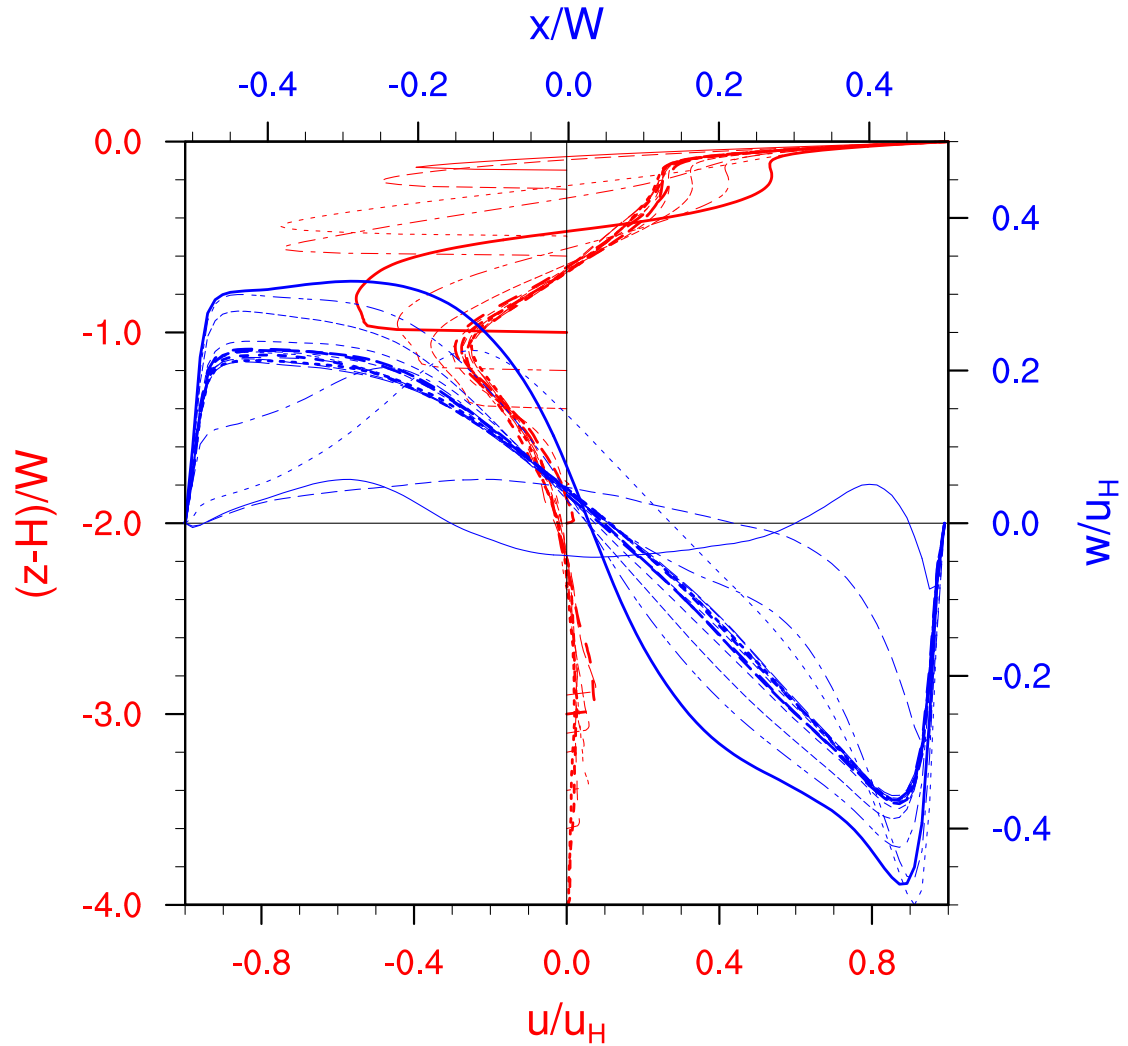
Figure 4.14: Modified cavity profiles for different canyon aspect ratios.
Red: vertical profile of streamwise velocity $\langle \bar{u} \rangle / u_{\mathrm{H}}$ at canyon center $x/W = 0$ *scaled with canyon width W*; blue: streamwise profile of vertical velocity $\langle \bar{w} \rangle / u_{\mathrm{H}}$ at height $z' = \max\left(\left(-\frac{H}{2}\right)/W, -0.7\right)$. Both are normalized with the streamwise velocity at roof height H. For line patterns refer to the legend of Fig. 4.13.

2. Going one step further, Figure 4.15 scales these profiles (shown in green) to a fictitious canyon height of $1.4\,H$ and thus achieves a good qualitative agreement among *all* profiles. Note that in Figure 4.15 the height where $[\bar{u}] = 0$ is either $z - H \approx -0.7\,W$ (red lines, $H/W \geq 1.4$) or $z - H = -\frac{H}{2}$ (green lines, $H/W < 1.4$).

3. For continuity reasons the height where $[\bar{u}] = 0$ is a suitable height for streamwise $\langle \bar{w} \rangle$ profiles; Figure 4.14 shows them in blue. For cases with aspect ratios $H/W \gtrsim 1.8$ all $\langle \bar{w} \rangle$ profiles collapse to a single profile that characterizes the clockwise rotating upper canyon vortex. Cases with aspect ratios $H/W = 1.0 \ldots 1.4$ are qualitatively similar. Case AR0015 clearly shows the two distinct updrafts associated with the wake interference regime. The remaining cases AR0025–AR0060 show a gradual transition between the two regimes.

Starting from Figure 4.15 integral turbulence statistics in the remainder of this subsection

are horizontally averaged, i.e. averaged in spanwise and streamwise direction, denoted by square brackets [ ]. Vertical profiles of horizontally averaged turbulence statistics provide useful information for urban parameterizations in larger-scale models.

It is worth noting that Fig. 4.15 shows the weak second inflection point in several $[\bar{u}]$-profiles – marked by an oval shape (cf. Fig. 4.4c ② on page 46). The fact that even this horizontal average shows the inflection point suggests that the second shear layer, though weak, is not negligible.

The analysis of the aspect ratio study 1 has shown that the vertical profile of streamwise velocity can be described by *one single vertical profile* in the deep canyon range $1.8 \lesssim H/W \lesssim 10$. It shall be called *deep canyon profile* for sake of argument. The good qualitative agreement in the range $1.0 \lesssim H/W \lesssim 1.4$ suggests that the deep canyon profile may still be applicable here – with a suitable multiplicative correction. For $H/W \lesssim 1.0$ there is still some qualitative agreement, but the $[\bar{u}]$ minimum moves towards the bottom, and the second inflection point below rooftop vanishes, which limits the applicability of the deep canyon profile.

This study suggests that geometry effects are responsible for this "one profile":

- H is the limiting length scale in canyons with $H/W < 1$, which is why they scale with H.

- W is the limiting length scale in canyons with $H/W > 1$, which is why they scale with W.

In fact, in study 1 the transition between these two scalings occurs at $H/W \approx 1.0 \ldots 1.4$. The observation that all canyons with $H/W \gtrsim 1.4$ collapse to the deep canyon profile with a distinct $[\bar{u}]$ minimum at an almost constant height of $(z-H)/W \approx -1.04 \ldots 1.08$ (Fig. 4.15) means that their upper canyon vortex is almost symmetric; the *upper canyon vortex aspect ratio* is

$$A := \frac{\text{vortex height}}{\text{vortex width}} \approx 1.04 \ldots 1.08 \quad . \tag{4.3}$$

This leads to the question whether A is universal, or, if it isn't, on which parameters it depends. The results of the local roughness parameter study 3 in Figure 4.16 indicate that A is not universal. The $[\bar{u}]$ minimum is displaced downwards for all "smooth" cases (AR0200s: $A = 1.36$, AR0360s: $A = 1.50$) and also for the "rougher" case AR0360r ($A = 1.26$). This would mean that a) A increases with decreasing local roughness and that b) A then also depends on the canyon aspect ratio.

Since study 3 covers only four canyon aspect ratios ($H/W = 0.5, 1, 2, 3.6$) and three local roughness lengths ($z_{0,\text{loc}} = 0.01, 0.05, 0.1\,\text{m}$), its parameter space is too coarse to draw further conclusions. An extension of the parameter space is beyond the scope of the present study; this is therefore suggested for further research.

Literature results also indicate that A does not have a universal value in deep canyons. The only scale model experiment on A in deep canyons is the water tank study of Baik et al. (2000); it gives $A \approx 1.2$ for $H/W = 2$ and an apparent convergence to $A \approx 1.5$ for canyon aspect ratios $H/W = 2.4, 3$, whereas their RANS model results show only little variation ($A \approx 1.2 \ldots 1.3$). Baik et al. (2000) discuss momentum transfer ratios, turbulence closure and wall friction effects as possible reasons for this discrepancy. Further RANS model aspect ratio studies give $A \approx 1.0 \ldots 1.1$ (Baik and Kim, 1999) and $A \approx 1.2 \ldots 1.3$ (Kim and Baik, 2001), $A \approx 1.2 \ldots 1.6$ (Jeong and Andrews, 2002) and $A \approx 1.4 \ldots 1.6$ (Sini et al., 1996). In agreement with the present study, the differences *between* these numerical
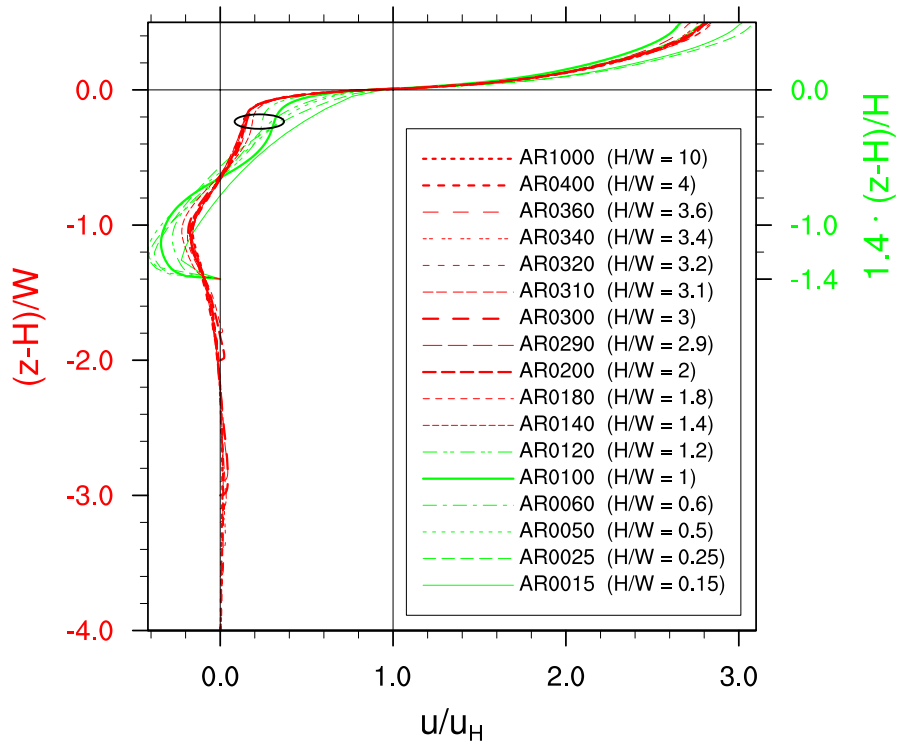
Figure 4.15: As in Figure 4.14, but horizontally averaged $[\bar{u}]$ profiles only, including the free stream layer. Green: $[\bar{u}]$ profiles with $H/W < 1.4$ scaled to a fictitious canyon height $1.4\,H$. The oval shape marks weak inflection points (see text for details).
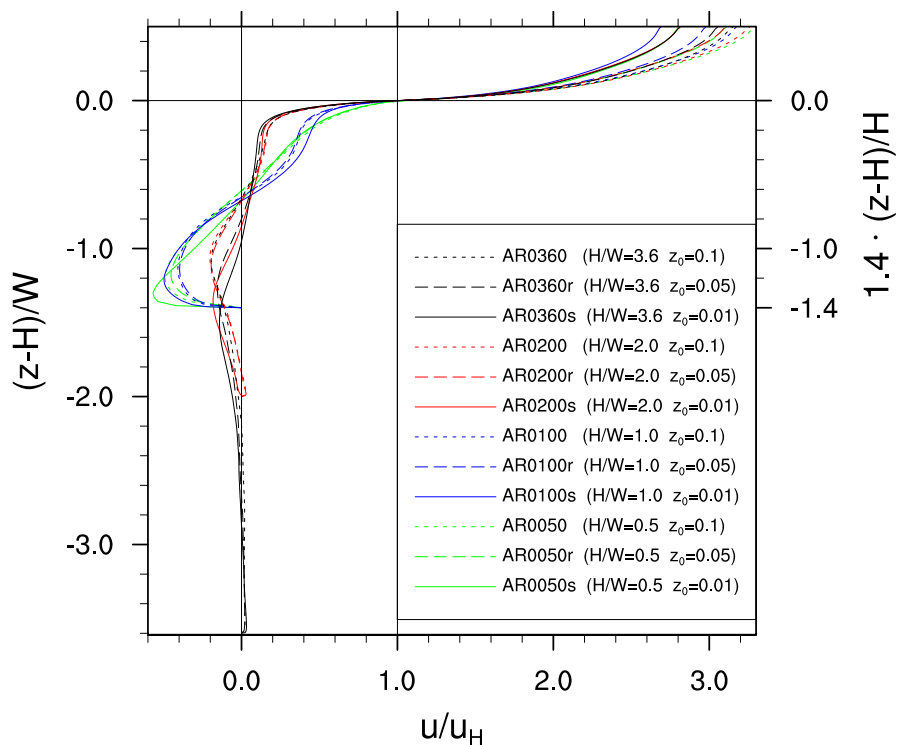
Figure 4.16: As in Figure 4.15, but for different local roughnesses $z_{0,\text{loc}}$. $[\bar{u}]$ profiles with $H/W < 1.4$ scaled to a fictitious canyon height $1.4\,H$.

studies are generally larger than the differences *within* each of these studies. The conclusion based on the numerical studies including the present one would be that the dependence of A on canyon aspect ratio H/W is weak, but its dependence on other parameters such as local wall roughness $z_{0,\mathrm{loc}}$ may be significant. Further experimental or LES/DNS studies are recommended to clarify this question.

4.5.2.2 Momentum fluxes

Following Kanda et al. (2004), the temporally averaged total momentum flux in the xz-plane is defined as

$$\overline{R} = \overline{u'w'} + \overline{u}\,\overline{w} - \overline{K_m\left(\partial_x w - \partial_z u\right)}, \tag{4.4}$$

where $\overline{u'w'}$ is resolved Reynolds stress, $\overline{u}\,\overline{w}$ is dispersive stress and $\overline{-K_m\left(\partial_x w - \partial_z u\right)}$ is SGS stress. Note that this definition neglects the contribution of spanwise stresses. However, for a real urban street canyon Christen et al. (2003) found that channeling can lead to a contribution of $\overline{v'w'}$ between 5% above and up to 20% within the urban canopy, which is not negligible. Hence the definition (4.4) is acceptable only for strictly perpendicular ambient flow without channeling. This is the case in the present study.

The partitioning of $\overline{R}$ into the different stresses gives information about the following:

1. The numerical quality of the simulation:

    a) For a sufficient grid resolution the SGS stress should be small compared to the total flux;

    b) For a sufficient averaging time the dispersive stress *above* the canyon should be small compared to the total flux (Coceal et al., 2006).

2. The relative importance of turbulent momentum transport (Reynolds stress) and the transport through spatially organized structures (dispersive stress).

Figure 4.17 shows vertical profiles of horizontally averaged momentum fluxes for the canyon aspect ratio study 1, using the special scaling developed in subsection 4.5.2.1. The above points can be answered as follows:

1. a) The grid resolution is sufficient because except at roof height the SGS stress is negligible. The SGS stress is largest in the first few grid layers just above the roof, which is why the horizontal average of SGS stress peaks just above the roof height.

    b) The averaging time is sufficient because the dispersive stress above the canyon is (almost) negligible.

2. *Above the canyon* dispersive stresses are small; turbulent transport dominates. This is in agreement with recent DNS over cubes (Coceal et al., 2006) and with experimental studies (Cheng and Castro, 2002; Poggi et al., 2004).

    Within the canyon one needs to distinguish three canyon aspect ratio ranges:

    a) $H/W \geq 1.0$: Dispersive stress is larger than Reynolds stress and dominates momentum transport, except very near the roof level. Only in this range total momentum flux, dispersive and Reynolds stress all change sign within the canopy at $(z-H)/W \approx -0.1$ because of the strong recirculation that is associated with the skimming flow regime.
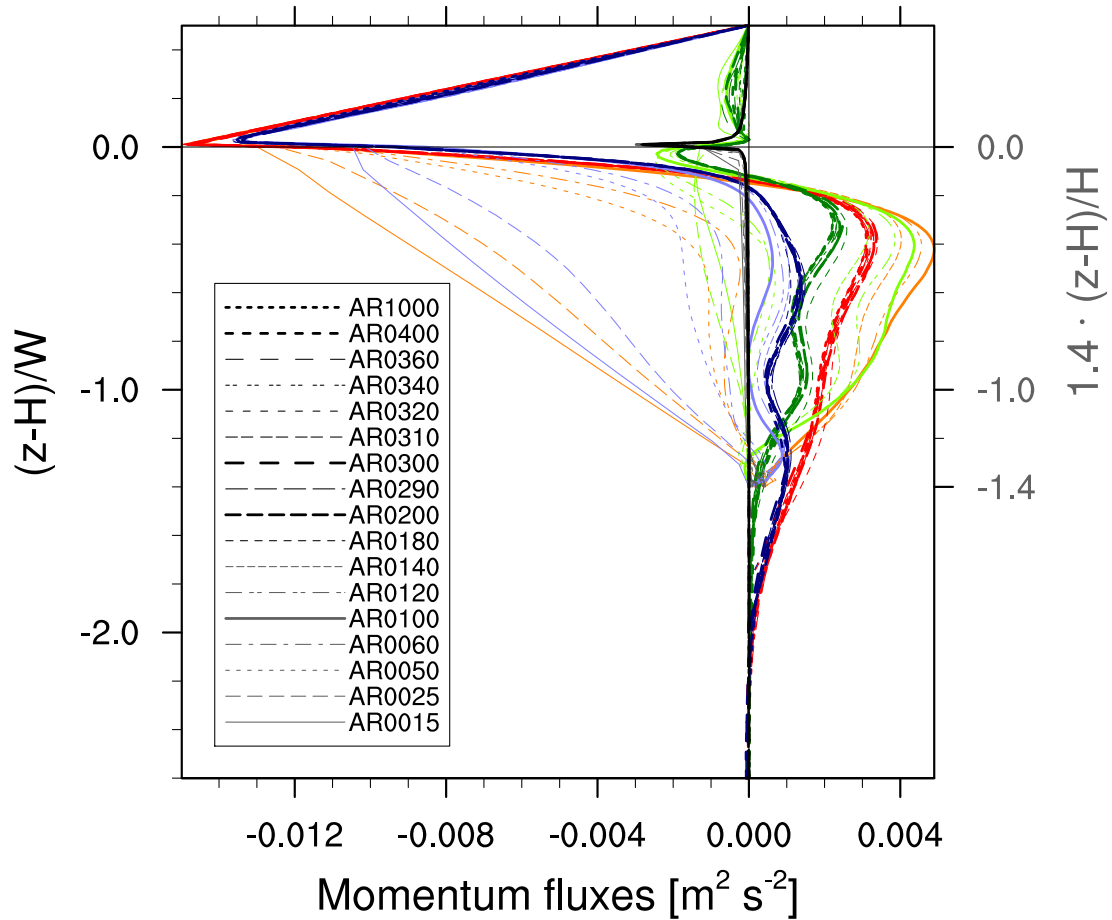
Figure 4.17: Horizontally averaged momentum flux profiles for canyon aspect ratio study 1. Line patterns refer to aspect ratio. Dark-coloured profiles are scaled with canyon width W; light-coloured profiles with $H/W < 1.4$ are scaled to a fictitious canyon height $1.4\,H$. Red (orange): total momentum flux $[\,\overline{R}\,]$; blue (light blue): resolved Reynolds stress $[\,\overline{u'w'}\,]$; black (grey): SGS stress $[\,-K_m\,(\partial_x w - \partial_z u)\,]$; green (light green): dispersive stress $[\,\overline{u}\,\overline{w}\,]$.

b) $H/W \le 0.25$: Reynolds stress is larger than dispersive stress and dominates momentum transport.

c) A transition range at $H/W \approx 0.5 \dots 0.6$.

The momentum fluxes differ qualitatively from the recent numerical cube studies of Kanda et al. (2004) and Coceal et al. (2006). This can be attributed to a fundamental geometry difference between cubes and canyons. Canyons allow the air two options only, recirculation within or flow over the canyon. However, cubes additionally allow some portion of the air to flow around them, which creates additional turbulence especially in the upper half of the cube canopy and thus reduces the dispersive stress there. In the canyon, the most turbulent region is the roof level shear layer, and indeed the dispersive stress is relatively small there.

It is worth noting that in deep canyons with $H/W \ge 2.0$ again all vertical profiles collapse to a *deep canyon profile*.

4.5.2.3 Standard deviations

The standard deviations

$$\sigma_u \cong \sqrt{\overline{u'^2}}, \quad \sigma_v \cong \sqrt{\overline{v'^2}}, \quad \sigma_w \cong \sqrt{\overline{w'^2}} \tag{4.5}$$

are important for urban dispersion modelling because the dispersion rate of a pollutant cloud is proportional to σ_{u_i} (Britter and Hanna, 2003). Note that the definition (4.5) uses the resolved-scale turbulent variances only, because in PALM the SGS variances are not known and would have to be parameterized (only SGS-TKE e is known; as a first approximation $\frac{1}{3}e$ could be used for each component).

Roth (2000) compiled reference values *over* cities that are quite similar to the reference values $\sigma_u/u_* = 2.39$, $\sigma_v/u_* = 1.92$, $\sigma_w/u_* = 1.25$ compiled by Panofsky and Dutton (1984) for flat, rural terrain. The focus of the present study is on the standard deviations *within* the urban canopy. There is a continuous debate on how to suitably scale urban turbulence statistics over and within the urban canopy (e.g., Roth, 2000; Cheng and Castro, 2002; Britter and Hanna, 2003; Kastner-Klein and Rotach, 2004; Eliasson et al., 2006; Moriwaki and Kanda, 2006).

Figures 4.18 and 4.19 present four of the more frequently used scaling methods for standard deviations following Roth (2000):

- scaling either with the mean wind $U = \sqrt{\overline{u_i}^2}$ (left-hand-side panels a,c,e) or with a friction velocity $u_* = \sqrt{|\overline{R}|}$ (right-hand-side panels b,d,f)...

- ...determined either locally ($U_{\text{loc}}, u_{*,\text{loc}}$ in Fig. 4.18) or at the roof height H of maximum shear stress ($U_H, u_{*,H}$ in Fig. 4.19).

Above the canyon $[\sigma_{u_i}]$ appear to scale with $u_{*,\text{loc}}$ (Fig. 4.18b,d,f). At first sight this agrees with theory (Panofsky and Dutton, 1984; Kaimal and Finnigan, 1994), measurements (e.g. Roth, 2000; Christen, 2005; Eliasson et al., 2006) and numerical simulations (e.g. Kanda et al., 2004). However, constant $[\sigma_{u_i}]$ values are normally not reached above the canopy top immediately but only well within the roughness sublayer or further above. In the present study the free-stream layer is too shallow to draw further conclusions.

The non-local rooftop scaling shows that $[\sigma_{u_i}]$ actually decrease linearly with height in the free-stream layer (Fig. 4.19).

Within the canyon the first observation is that all deep canyon profiles (red) collapse to one deep canyon profile, which again suggests that the chosen vertical scaling with canyon width W is appropriate for this study. Even some scaled green profiles show qualitative similarity. Under local scaling (Fig. 4.18), the deep canyon profiles are roughly constant in a layer $(z - H)/W = -0.2\ldots -1.0$ that corresponds well to the upper canyon vortex. Under rooftop scaling (Fig. 4.19), the deep canyon profiles show 1) a pronounced $[\sigma_{u_i}]$ peak at rooftop, 2) a quick exponential decrease just below, 3) a slow linear increase with depth in the upper vortex layer, and 4) a slow exponential decrease with depth further below. An exponential decrease is also apparent in Britter and Hanna (2003, Fig. 4). This study suggests the following interpretation:

1. The shear layer at roof level is thin and its height is well-defined by the roof; it is characterized by strong turbulence and thus peak $[\sigma_{u_i}]$ values;

2. $[\sigma_{u_i}]$ values are much lower in the upper canyon vortex that is characterized by spatially organized flow (cf. the discussion on dispersive fluxes in subsection 4.5.2.2);
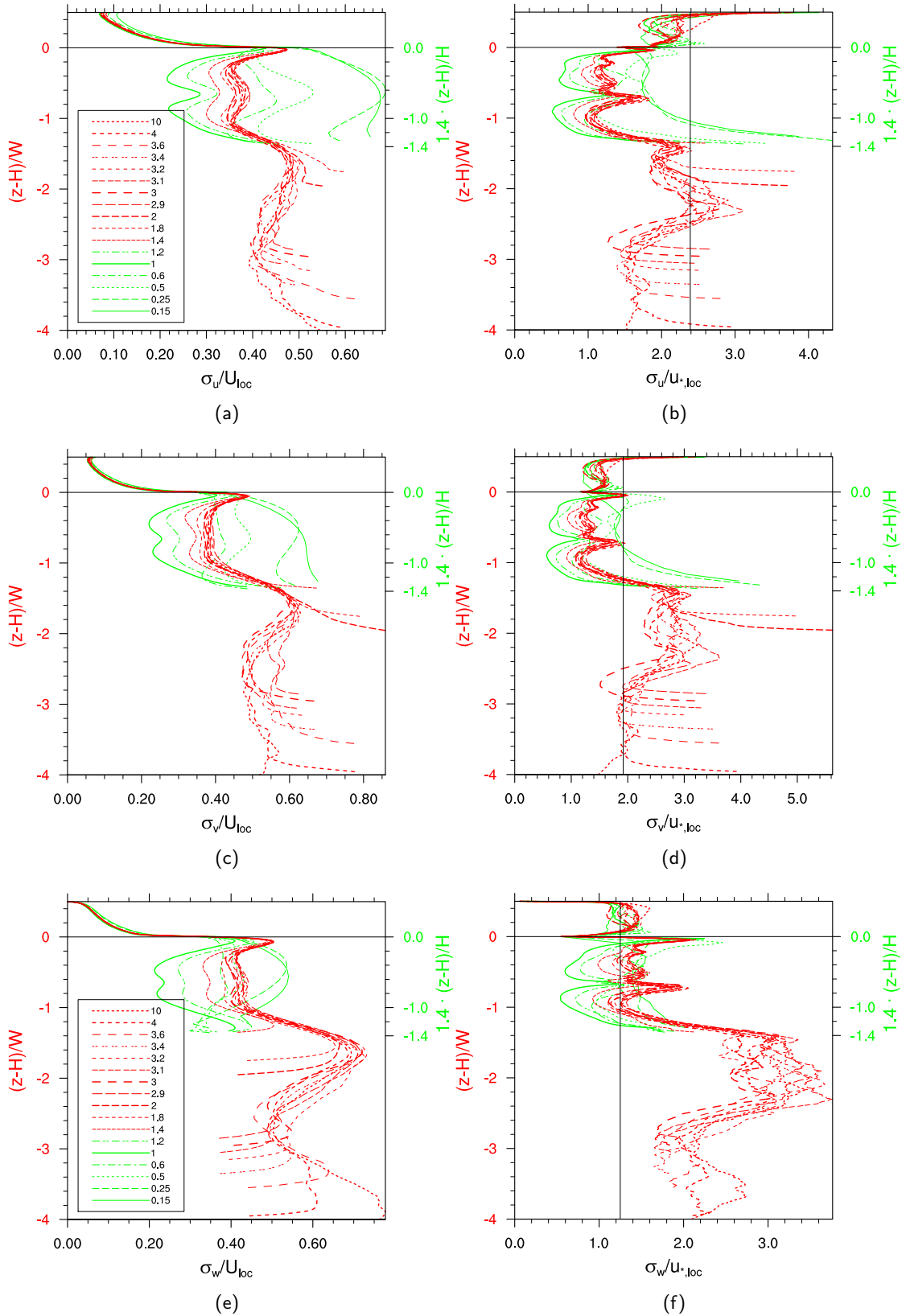
Figure 4.18: Horizontally averaged profiles of standard deviations (a-b) σ_u, (c-d) σ_v, (e-f) σ_w *locally scaled* with (a,c,e) mean wind speed U_{loc} and (b,d,f) friction velocity $u_{*,\text{loc}}$ for canyon aspect ratio study 1. Panels (b,d,f) contain reference lines for flat, rural terrain $\sigma_u/u_* = 2.39$, $\sigma_v/u_* = 1.92$, $\sigma_w/u_* = 1.25$ compiled by Panofsky and Dutton (1984, p. 160). Line patterns refer to aspect ratio. Green profiles with $H/W < 1.4$ are scaled to a fictitious canyon height $1.4\,H$.
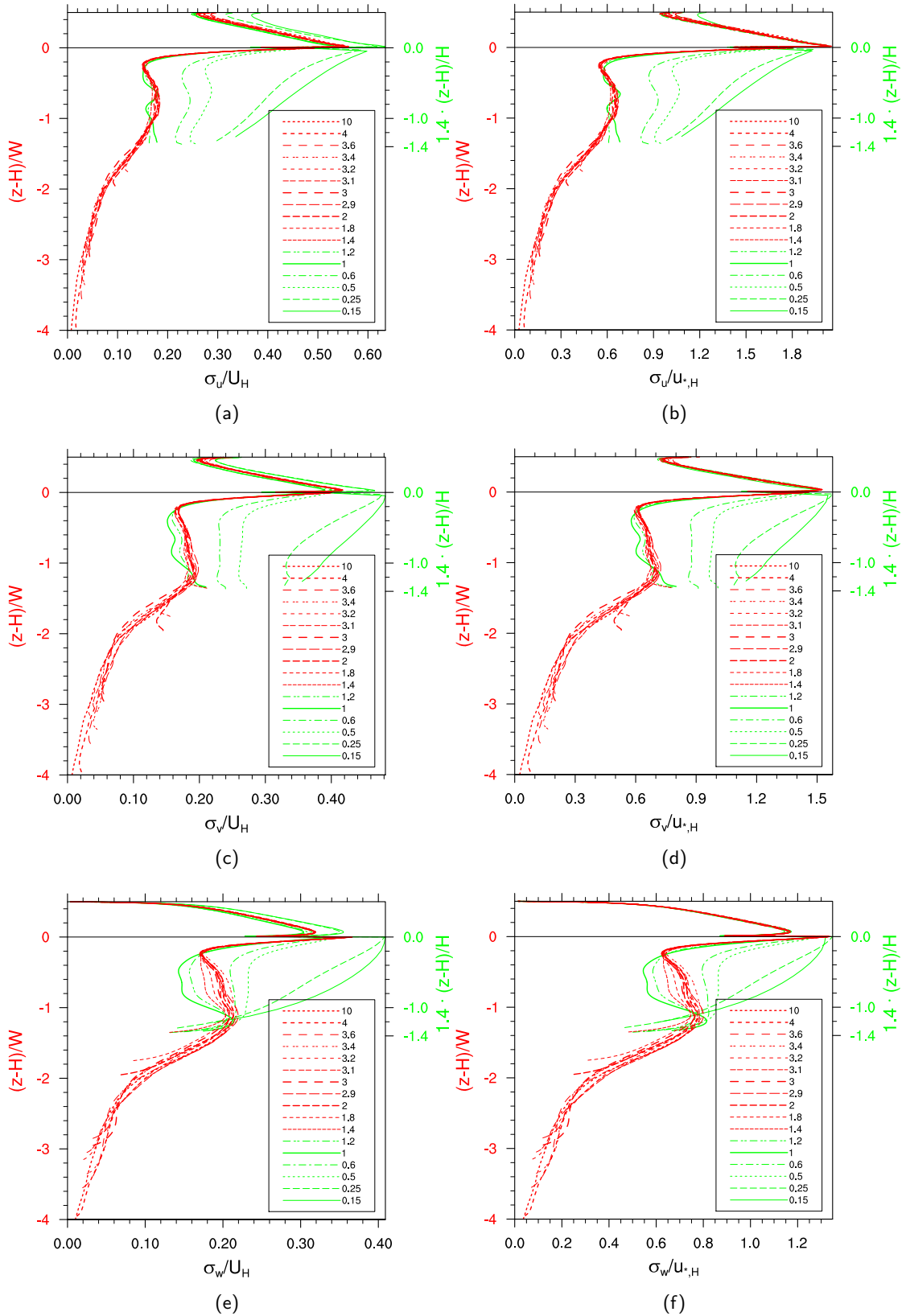
Figure 4.19: Horizontally averaged profiles of standard deviations (a-b) σ_u, (c-d) σ_v, (e-f) σ_w *scaled* with (a,c,e) mean wind speed U_H and (b,d,f) friction velocity $u_{*,H}$ *at roof height* H for canyon aspect ratio study 1. Line patterns refer to aspect ratio. Green profiles with $H/W < 1.4$ are scaled to a fictitious canyon height $1.4\,H$.

3. The upper vortex in turn drives a secondary recirculation further below, but because of its intermittency the height of the associated driving shear layer is less well-defined, which results in a less pronounced second peak of $[\sigma_{u_i}]$;

4. Further below, any canyon circulation is weak (cf. the low ψ values in Fig. 4.9 or the low $[\bar{u}]$ values in Fig. 4.15) and cannot maintain the upper $[\sigma_{u_i}]$ levels.

As suggested by several recent publications, within the urban canopy, non-local scaling such as the rooftop scaling in Fig. 4.19 is more appropriate than local scaling (Cheng and Castro, 2002; Kastner-Klein and Rotach, 2004; Moriwaki and Kanda, 2006). One reason for this is that local scaling can easily become ill-defined if the scaling parameter approaches zero but $[\sigma_{u_i}]$ do not (cf. Britter and Hanna, 2003). This is obviously the case for $u_{*,\mathrm{loc}}$ (Fig. 4.18b,d,f).

Eliasson et al. (2006) found significantly enhanced vertical mixing in the upper part of their real canyon ($\sigma_w/u_{*,\mathrm{loc}}$ up to 2), similar to magnitudes and patterns measured by Rotach (1995) and Christen et al. (2003). Figure 4.18f does not reproduce this. A likely explanation is that the present study lacks entrainment deep into the canyon (due to the shallow free-stream layer and the flat roofs).

To conclude, the non-local rooftop scaling has been shown superior to local scaling within the urban canopy. $[\sigma_{u_i}]$ profiles clearly reflect the roof level shear layer and the upper canyon vortex.

4.5.2.4 Length scales

The velocity length scales $[l_{u_i}]$ in Figure 4.20 are obtained from spectral peak wavelengths of wavenumber-weighted instantaneous velocity power spectra computed in streamwise (l_u, l_w) and spanwise (l_v) direction, respectively.[5] They approximately correspond to the size of the dominant turbulent structures of u, v, w respectively. Unfortunately, only ten instantaneous output times are available for calculation of $[l_{u_i}]$, which is why the horizontal averages $[l_{u_i}]$ show a large amount of scatter and should be regarded as tentative results only. Still, some first conclusions can be drawn.

Above the canyon $[l_w] \approx 0.25\,W$ is almost constant, with only a slight increase up to $(z - H)/W = 0.2$; $[l_v]$ is larger and increases with height up to $0.7\,W$. $[l_u]$ is largest, with a strong increase in the thin roof level shear layer, and roughly constant above ($0.6 \sim 0.8\,W$). Obviously the length scales in this study's shallow free-stream layer ($\delta = 0.5\,W$) are not comparable with the deep, real urban boundary layer (e.g. Roth, 2000; Christen, 2005), except for their relative order $[l_w] < [l_v] < [l_u]$.

Within the canyon several important observations can be made. In *deep canyons* $[l_w] \approx 0.3\,W$ is roughly constant with height except for the upper canyon vortex core region where it almost doubles ($[l_w] \approx 0.5\,W$). Here and down to about $(z - H)/W = -1.4$, $[l_u]$ is anticorrelated with $[l_w]$; $[l_u]$ has two local maxima of up to $0.6\,W$ at $(z - H)/W \approx -0.3, -1.1$; this is due to the strong recirculation in the upper canyon. Further below, $[l_u]$ decreases to the same level as $[l_w]$ and then also remains roughly constant.

In the past, 2D RANS/LES models were applied to 2D street canyons (Table 4.1) on the assumption that the flow is approximately 2D. If the flow in the 2D street canyon of

---

[5]Within the canyon streamwise spectra require tapering in order to reduce leakage due to the finite data. Tapering is a common data modification in spectral analysis of time series, where a large variety of tapers exists (cf. Båth, 1974; Kaimal and Finnigan, 1994; Bloomfield, 2000; Schlittgen and Streitberg, 2001, or Schönwiese, 2006). Here, the NCL built-in split-cosine-bell taper is used with a common taper width of 10% (cf. `http://www.ncl.ucar.edu/Document/Functions/Built-in/taper.shtml`).
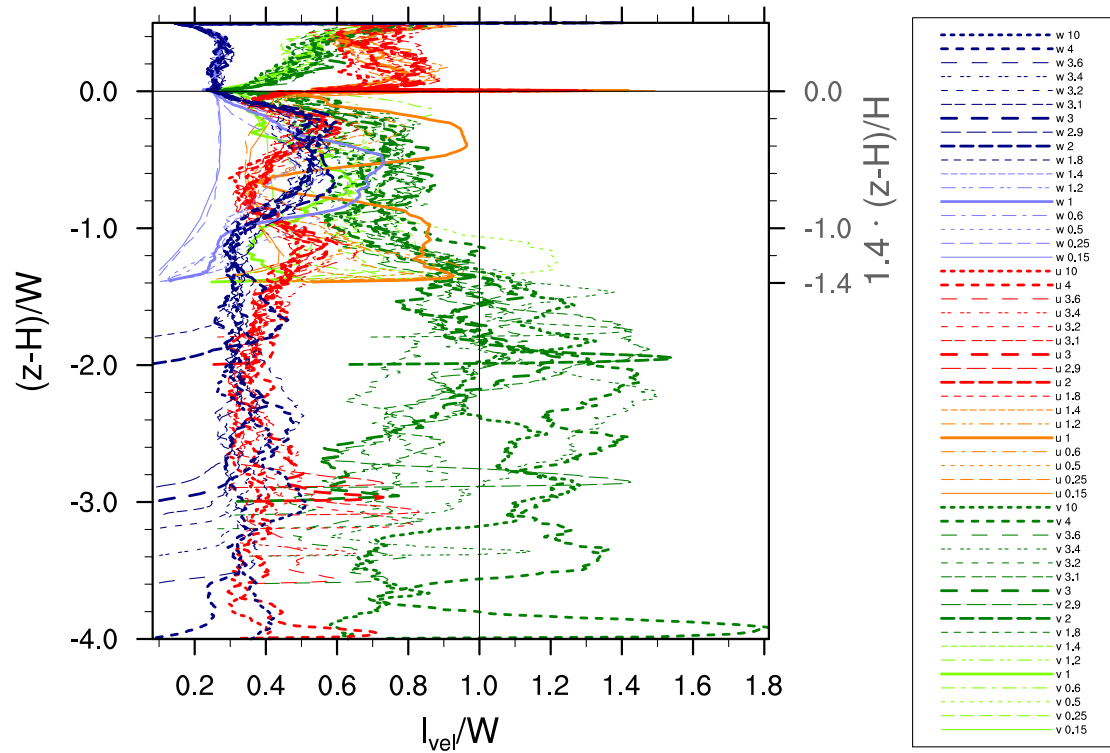
Figure 4.20: Length scales $[l_{u_i}]$ for canyon aspect ratio study 1.
Line patterns refer to aspect ratio. Dark-coloured profiles are scaled with canyon width W; light-coloured profiles with $H/W < 1.4$ are scaled to a fictitious canyon height $1.4\,H$. Blue (light blue): $[l_w]$; red (orange): $[l_u]$; green (light green): $[l_v]$.

the present study were exactly 2D, v would be constant in y-direction and thus no v-power spectrum would exist (Stull, 1988). An "approximately" 2D flow would imply that either $[l_v] \to \infty$ (if very low-frequency modes dominate the v-power spectrum) or $[l_v] \to 0$ (if very high-frequency modes dominate the v-power spectrum). Figure 4.20, however, shows that down to about $(z - H)/W = -1.4$, $[l_v]$ approaches neither limit but remains roughly constant at $0.6 \sim 0.8\,W$. This means that in the upper canyon the flow is fully 3D. Further below, $[l_v]$ increases to canyon width and beyond (where the spectral resolution is poor). In other words, the 2D assumption may be justified in the lower canyon only.

In the *regular canyon* $[l_w]$ and $[l_u]$ are somewhat larger but still qualitatively similar, while $[l_v]$ values are lower.

In the *shallow canyons* with $H/W = 0.15, 0.25$, $[l_w]$ retains its free-stream value and slowly decreases to zero with canyon depth. This reflects the change of flow regime (cf. Fig. 4.14). $[l_u]$ has weaker maxima (only up to $0.4\,W$) compared to regular or deep canyons, i.e. the dominant u structures are now smaller (see Fig. 4.8a).

Length scales deep within an urban canopy so far have been reported only by Christen (2005, Figs. 4.35a, 5.1l) as ensemble averages over all wind directions. They have been obtained from tower measurements in a real urban canyon with characteristic aspect ratio 1.3 (almost regular). There, $[l_{u_i}]$ retain their relative order $[l_w] < [l_v] < [l_u]$ within the canopy, without any sign of an anticorrelation between $[l_w]$ and $[l_u]$. Possible explanations for this are a) the ensemble average over all wind directions (in effect channeling flow dominates) and b) urban inhomogeneities such as pitched roofs, obstacles etc. (in effect the canyon recirculation is weakened). Further data are needed for a comparison (model data for an ensemble of wind

directions and/or measurement data for individual wind directions).

That aside, the most important conclusion from this subsection is that the flow in a 2D street canyon is fully 3D in shallow, regular, and at least in the upper part of deep canyons. It is therefore recommended that numerical street canyon models should also be 3D.

4.5.3 Convective feasibility study

Study 4 is a convective feasibility study with five different convective cases and one neutral reference case (see Table 4.5 on page 42). Its set-up (section 4.2) differs from studies 1–3 in several aspects: a) turbulence is not only generated dynamically but also by buoyancy; b) the Coriolis effect causes channeling in the street canyon; c) the canyon is now an isolated cavity because the horizontal domain size has been extended from $1.92\,W$ to $20\,W$; d) the boundary layer above the canyon is deeper ($\delta = 6.5 \sim 19\,W$ depending on canyon aspect ratio); e) less details can be resolved in the canyon due to the lower resolution ($R = 32$). This means that differences between the results of study 4 and studies 1–3 may not be directly attributable to one of these aspects. Still, a comparison shall be attempted. Study 4 is a tentative feasibility study because of the small number of cases computed and the limited data presented. The main goal of study 4 is to answer the "simple" question whether buoyancy effects can be important in street canyons or not.

Figure 4.21 shows the topology of mean street canyon flow in the xz-plane for study 4. First, the neutral reference case AR0050_H00 (Fig. 4.21a) is compared to its counterpart AR0050 of study 1 (Fig. 4.8c on page 52). Although the deep boundary layer ($\delta \approx 19\,W$) is now dominated by structures that are a few times larger than the canyon width, AR0050_H00 still features skimming flow, contrary to the wake-interference flow observed in some numerical studies (cf. Table 4.1 on page 39); this suggests that factors other than δ (e.g. inflow/upstream turbulence) also influence the transition between WIF and SF. Another possible reason may be that the grid resolution $R = 32$ that was just sufficient for case DP32 (Fig. 4.10c on page 54) may not be sufficient to resolve turbulence completely in the deeper boundary layer of case AR0050_H00. The canyon circulation (maximal streamfunction ψ) of case AR0050_H00, however, is weaker by about a factor of five; this may be caused by the enhanced turbulent mixing associated with the channeling flow. The lower corner vortex at the windward wall ($x/W = +0.5$) has practically disappeared.

A convective (AR0050_H01) and a strongly convective (AR0050_H04) case have been simulated for this canyon aspect ratio. In both cases the canyon circulation now extends above the roof level up to a height of $(z - H)/W = +0.2$, so that the convective boundary layer (CBL) flow above rooftop is diverted over the canyon (Fig. 4.21b,c). A tongue of warm air extends from the canyon floor along the leeward wall up to the roof level (not shown); buoyancy effects and canyon vortex act together to produce a canyon circulation that is up to twice as strong as for case AR0050_H00. The four times stronger surface heating for case AR0050_H04 produces a slightly stronger canyon circulation.

For case AR0100_H01 (Fig. 4.21d) both the flow diversion over the canyon and the canyon vortex speed-up are much weaker, and for cases AR0200_H01 and AR0350_H01 both are insignificant. The latter cases now have buoyancy-driven local updraughts at either wall and downdraughts in between (not shown), which is reflected in their modified streamfunction patterns (Fig. 4.21e,f).

For all convective cases the dominant turbulent structures in the CBL above rooftop are at least one order of magnitude larger than the canyon width.

Overall the results of Figure 4.21 indicate that a balance between dynamically driven and thermally driven canyon circulation occurs in a region of the parameter space (aspect ratio,
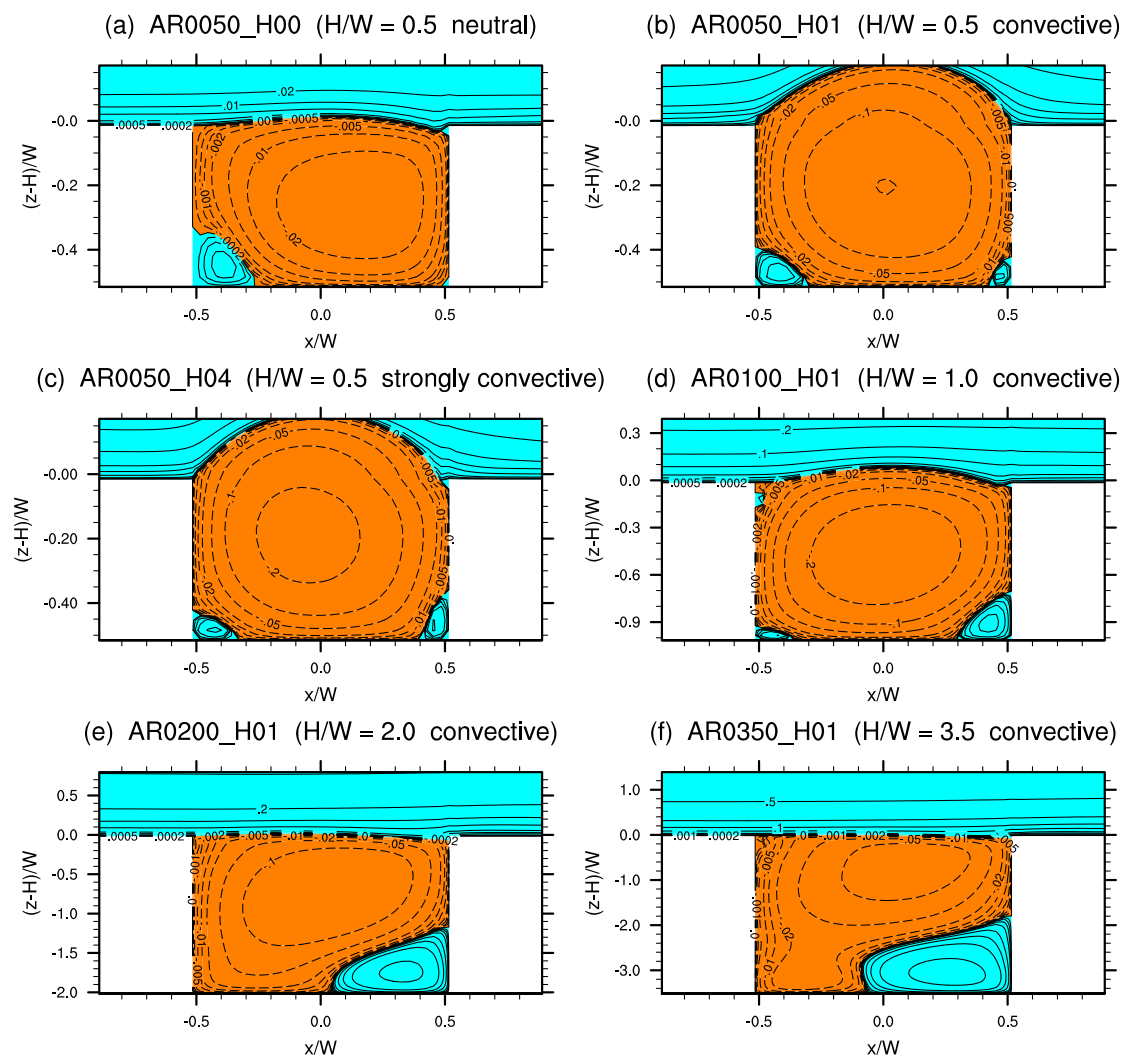
Figure 4.21: Mean flow topology for the convective feasibility study 4.

driving shear, driving surface heating) that can be reached in cities. In short, thermal effects in street canyons may not be negligible. In literature, no consensus has been reached yet on how important buoyancy effects really are (cf. the review by Li et al., 2006). Several numerical models produced significant buoyancy effects of heated canyon floor, windward or leeward wall at low perpendicular wind conditions (Sini et al., 1996; Kim and Baik, 1999, 2001; Bohnenstengel et al., 2004; Xie et al., 2006). However, the field experiment of Louka et al. (2002) showed that the 2D model CHENSI (used also by Sini et al.) overestimates the influence of windward wall heating, and the field measurements of Offerle et al. (2007) could not confirm the strength of thermal effects as produced by numerical models. On the other hand, wind tunnel studies of Uehara et al. (2000) and Kovar-Panskus et al. (2002b) could clearly identify thermal effects.

It should be noted that the experimental conditions of most above studies are not harmonized (the present study is no exception), which makes a comparison quite difficult and a unified picture of thermal effects hard to obtain. A joint effort of wind tunnel and numerical experiments, perhaps in combination with an urban field campaign could help not only to clarify the role of thermal effects, but also to identify potential weaknesses of each approach.
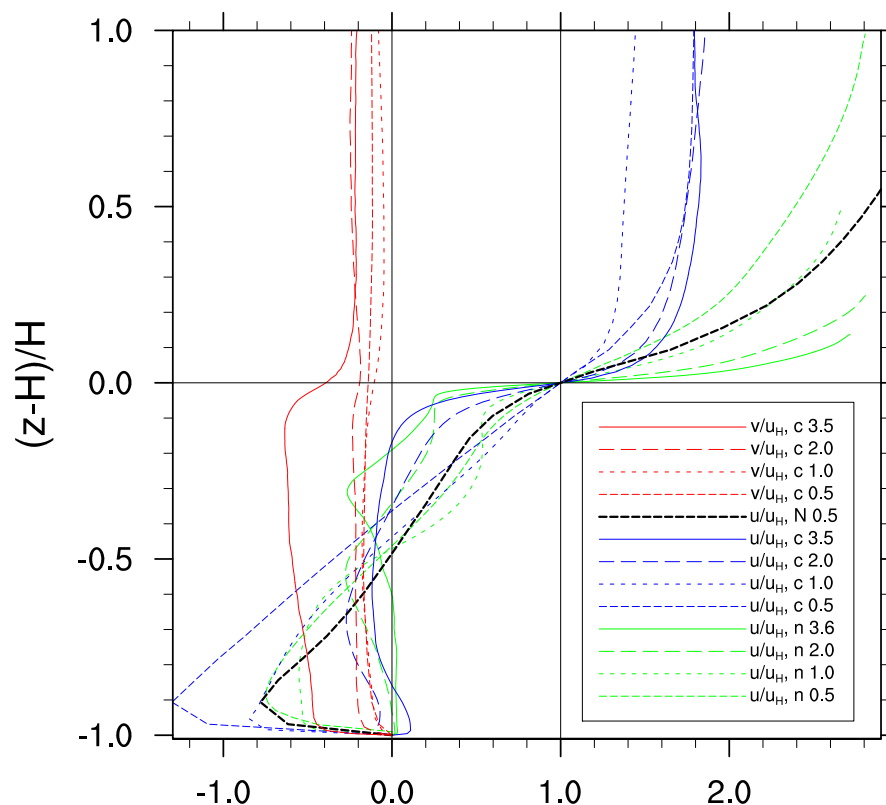
Figure 4.22: Vertical profiles of u and v velocity components at canyon center normalized by mean flow at roof level for cases AR0050/0100/0200/0350_H01 ("c") and the neutral reference case AR0050_H00 ("N") of study 4 as well as the corresponding cases AR0050/0100/0200/0360 ("n") of study 1. Line patterns refer to aspect ratio.

A similar intensification of canyon recirculation as for cases AR0050_H01/04 was reported by Kim and Baik (2001) for an isolated cavity of aspect ratio 0.6 and by Bohnenstengel et al. (2004) for an isolated canyon of aspect ratio 0.6. However, the deep canyon pattern of two narrow updraughts near each wall for cases AR0200_H01 and AR0350_H01 did not occur in the 2D simulations of Kim and Baik (1999, 2001). Real world measurements do exist, but of course the situation is more complex than in the models, making a comparison difficult. For example, the thermal distribution depends not only on canyon geometry but also on diurnal and seasonal changes (Kanda et al., 2005; Offerle et al., 2007), and a bottom-only heating is unrealistic because normally at least part of a wall is (also) heated, and even wall portions in the shadow may still be warm due to thermal inertia.

Concerning vertical scaling, Figure 4.22 indicates that under convective conditions, the characteristic vertical scaling is the canyon height H, not the canyon width W that was used in the previous subsections. Well above the canyon the velocity components are almost constant with height as expected in a convective mixed layer. v is non-zero especially within the canyon because of channeling. A comparison between convective and neutral runs confirms that the intensification of canyon recirculation is indeed strongest for case AR0050_H01 and weaker for case AR0100_H01, and that at least in the centerplane is confined to the lower part of the canyon. No intensification can be observed in deep canyons.

Integral turbulence statistics such as heat and momentum fluxes, standard deviations and length scales are beyond the scope of this feasibility study; at this stage, it shall suffice to

conclude that first test simulations have shown that buoyancy effects can play an important role in modifying recirculation in both shallow and deep canyons.

4.6 Discussion

Cui et al. (2004) criticized the experimental set-up of the Liu and Barth (2002) LES experiment for the shallow depth of the free-stream layer compared to the size of the street canyon. This set-up was subsequently also adopted by Liu et al. (2004); Li et al. (2005) and the present study. Indeed, in the present study $\delta = 0.5\,W$ limits the size of turbulent structures that could enter deep into the canyon and deepen the rooftop shear layer by entrainment. However, a comparison between cases AR0050 (shallow) and AR0050_H00 (deep) did not find significant differences in flow topology. This suggests that the choice of $\delta = 0.5\,W$ may be acceptable because the present study focusses on flow within the street canyon. The computational time saved by this compromise was "re-invested" in a high resolution of $R = 100$ grid points per canyon width for studies 1–3. Needless to say, the shallow free-stream layer itself is not representative of the deep urban boundary layer; analysis of this region is of limited value.

Since the free-stream layer is so shallow, the vertical shear is relatively large. This is (in a way) compensated by a comparably low absolute bulk velocity of only $u_b \approx 1$ m s^{-1}. Note that this is below the threshold value ($1.5 \sim 2$ m s^{-1}) for the onset of a canyon recirculation in real canyons that was observed by DePaul and Sheih (1986).

Another point to note is that the present study focussed on perpendicular wind only (with the exception of study 4), so the presented results do not allow to draw an "urban family plot" of integral statistics averaged over all wind directions like the one by Christen (2005). Perpendicular wind is about the only condition under which channeling does not occur. Field and wind tunnel experiments (Brown et al., 2004; Kono and Kusunoki, 2004, 2005) observed channeling in street canyons of finite length L even for only small deviations of wind direction from the perpendicular direction; also, the channeling flow interacted with the canyon end vortices.

Christen (2005) and Eliasson et al. (2006) pointed at the difficulty to determine the effective canyon/roof height H_{eff} at complex real urban sites. H_{eff} is also important for the vertical scaling used in the present study because H_{eff} is its reference height. Since the canyon width W was an equally important scaling parameter in the present study, a similar difficulty would arise to determine an effective canyon width W_{eff} at urban sites.

Roof geometry effects such as pitched roofs or asymmetric canyons (step up/down) have not been addressed here. Rafailidis (1997, 2000); Louka et al. (1998); Kastner-Klein et al. (2004) and Barlow and Pascheke (2006) demonstrated a significant influence of roof geometry on canyon circulation and the associated integral statistics.

4.7 Conclusions

Street canyon parameter studies have been performed with perpendicular wind with the following main conclusions:

1. The neutral flow within the canyon is shear-driven by Kelvin-Helmholtz instabilities from the rooftop shear layer. These instabilities are intermittent, and so is the canyon recirculation;

2. In deep canyons the upper canyon vortex drives a weaker, even more intermittent counterrotating recirculation further below;

3. Even in a street canyon whose geometry is homogeneous in spanwise direction (2D canyon), the flow is fully 3D in shallow, regular, and at least in the upper part of deep canyons;

4. Skimming flow occurs in regular and deep canyons, but no more than two vertically aligned counterrotating canyon vortices are observed;

   a) Integral statistics of deep canyons vertically scale with canyon width (starting from the rooftop level downwards);

   b) Regular canyons can be scaled to a fictitious canyon depth of $1.4\,H$ to qualitatively match the deep canyon profiles;

5. The wake interference regime associated with shallow canyons yields qualitatively different integral statistics;

6. In the convective boundary layer the vertical scale is the canyon height. Tentative results suggest that realistic combinations of urban conditions can give situations where buoyancy-driven canyon circulation balances or dominates shear driven flow.

This has important implications e.g. for air pollution modelling using RANS models:

1. Only 3D RANS models should be used, if dispersive fluxes in spanwise direction are not negligible, for the flow is fully 3D;

2. The intermittency of the canyon circulation can enhance removal of pollutants released at pedestrian level even under perpendicular ambient wind conditions. This contradicts the image of pollutant trapping within RANS-generated "steady" canyon vortices: these vortices are not steady;

3. Standard deviations of velocity components within the canyon should not be treated as constant for perpendicular ambient wind conditions. This agrees with recent field observations by Christen et al. (2003) and Eliasson et al. (2006);

4. Instead, standard deviations and other parameters may be parameterized conveniently based on a vertical scaling with characteristic canyon width W in deep canyons.

The discussion in section 4.6 identified potential weaknesses of the present study as well as possible areas of further research. It is proposed to extend this research to

- realistic boundary layer depths,

- inflow-outflow boundary conditions with turbulent inflow,

- an ensemble of different approaching wind directions,

- different roof geometries.

A further goal could be the inclusion of more relevant processes such as anthropogenic heat, solar radiation and dispersion of pollutants.

5 Turbulence visualization

The complex urban fabric causes urban flow to be turbulent and fully 3D, yet 4D if its time dependence is considered as a fourth dimension. Data presented so far in this study were either 0D (e.g. characteristic length scales), 1D (e.g. vertical profiles), or 2D (e.g. cross-sections) – and mostly time-averaged. However, even the simple geometry validation case of chapter 3, the surface-mounted cube, exhibits instantaneous flow phenomena that deviate considerably from the 3D topology of the time-averaged flow given in Figure 3.2 on page 23 (e.g. Shah and Ferziger, 1997; Breuer, 2002). This is characteristic of turbulent flow where the turbulent fluctuations can easily reach the same order of magnitude as the temporally or spatially averaged mean.

The necessity to generalize and abstract the data that are required to describe turbulent flow for scientific analysis and discussion (e.g. by dimension reduction, temporal/spatial averaging, definition of characteristic properties, statistical analysis etc.) is of course beyond question. This task is one of the driving questions of turbulence research (Lesieur, 1997; Pope, 2000).

However, there are good reasons also to look into the "raw", time-dependent, instantaneous 3D turbulent flow structures (i.e. the full 4D flow data) by means of turbulence visualization: 1) mainly for the scientific investigators themselves to gain a first, qualitative insight into the physical processes that make for – or may be "masked" by – the generalization/abstraction, 2) for intuitive presentations in an interdisciplinary community or towards the general public, and 3) as an add-on to scientific publications. Nowadays non-profit organizations such as IWF Knowledge and Media[1] in Göttingen, Germany, offer to host scientific media publications a) for use in public education and b) as external material of peer-reviewed publications in conventional "paper journals".

Visualization of scientific data is a science of its own; this chapter covers only those aspects that are relevant to this study. It is important to realize that, due to its very nature, the numerical visualization of turbulence involves a huge amount of data with an enormous demand of hardware resources (harddisk speed and capacity, network speed, graphics card, to name but a few). This requires sophisticated hard- and software solutions. The following sections show the challenges of turbulence visualization (section 5.1), the merits and limitations of the solution used in PALM (section 5.2) and an example using the urban PALM version (section 5.3).

5.1 Visualization pipeline

The visualization process can be conceptionally decomposed into the following steps of the abstract *visualization pipeline* (Haber and McNabb, 1979; Olbrich et al., 2001; Jensen et al., 2002)[2]:

1. Data source
   Generation of raw data by a scientific application (e.g. by a CFD simulation)

---

[1] See `http://www.iwf.de` or `http://www.dyvis.org` for details.
[2] Gaus (2006) is acknowledged for providing the examples.

2. Filtering (raw data → data extract)
   Selection and modification of relevant data (e.g. smoothing, resampling, interpolation, derivation of further quantities)

3. Mapping (data extract → 3D)
   Mapping the extracted data into geometric 3D objects (e.g. streamlines, isosurfaces, coloured slicers, attributes)

4. Rendering (3D → 2D)
   Transformation of illuminated 3D scenes into 2D pixel images (e.g. Z-buffer, OpenGL/ Direct3D, raytracing, radiosity)

5. Display
   Monitor / projection (e.g. stereoscopic projection, holobench, CAVE)

In practise, at each step of the visualization pipeline the data volume is reduced. The steps of the pipeline are consecutively assigned to a *data generator* producing the data (e.g. a CFD simulation running on a parallel supercomputer) and a *dedicated visualization computer* displaying the visualization (a visualization supercomputer or a workstation/notebook). Four scenarios are possible:[3]

(A)   Data generator: step 1 — dedicated visualization supercomputer: steps 2-5

(B)   Data generator: steps 1-2 — dedicated visualization supercomputer: steps 3-5

(C)   Data generator: steps 1-3 — dedicated visualization computer (workstation/ notebook): steps 4-5

(D)   Data generator: steps 1-4 — dedicated visualization computer (workstation/ notebook): step 5

Consider a typical PALM simulation with $O(10^8)$ grid points and $O(10^4)$ time steps that in total produces $O(\text{TB})$ data per variable (~ 30 variables)[4]. Supercomputers principally do offer the necessary hardware to store and analyse such huge datasets, but until today visualization is typically done on a separate workstation or a dedicated facility and not on the supercomputer itself. However, the efficiency and flexibility of existing visualization soft- and hardware are insufficient. Possible bottlenecks include the insufficient computing speed of (non-parallel) commercial visualization software and their machine memory requirements.

   All CFD models traditionally follow approaches (A) or (B) to store and transfer their raw or filtered simulation data and to visualize them on a dedicated postprocessing system after the simulation has finished. (One reason for doing so is that the stored data are often required for further numerical analysis that cannot be performed during the simulation if it requires data spanning the entire simulation length. The visualization option is then a by-product.) Approach (B) is a standard option also in PALM, however, it produces a huge amount of data.

   It was therefore highly desirable to use an alternative visualization technique that significantly improves computational efficiency. A technique that follows approach (C) has been implemented into PALM. It is introduced in the following section.

---

[3] The following discussion closely follows Olbrich et al. (2001) and Chmielewski and Jensen (2006).

[4] By analogy with the formal mathematical definition, this chapter uses $O(\dots)$ as a short notation to indicate the order of magnitude or the scaling power of a quantity.

5.2 Distributed Simulation and Virtual Reality Environment (DSVR)

The Distributed Simulation and Virtual Reality Environment (DSVR) developed at RRZN/ L3S[5] since 1997 and since recently also at ZIM[6] follows approach (C). DSVR was coupled with PALM during the joint research projects "Tele-Immersion"[7] and "EVITA"[8] (Olbrich et al., 2001; Jensen et al., 2002). The philosophy of DSVR is to make maximal use of the power of the data generator supercomputer during the visualization process (for example by parallel data extraction using the same domain decomposition as the simulation).

On the *data generator* side, during the PALM simulation, DSVR maps the extracted data into 3D geometric objects (coloured slicers, isosurfaces, streamlines, particles) and stores only them – in the specially designed, compact DVR binary format. On parallel computers DSVR uses parallel data extraction via MPI based on PALM's domain decomposition (cf. section 2.5). If a network is available, these data are simultaneously transferred to an external DVR streaming server to host the data.

On the *dedicated visualization computer* side, these data can be retrieved from the streaming server and visualized *on-the-fly* (or anytime later) by the DSVR Viewer. The DSVR Viewer is an internet-browser plugin for fully interactive navigation and animation of 3D DSVR scenes in a virtual reality environment. It uses OpenGL for rendering. PALM results can thus easily be visualized using standard internet technology and commodity graphics hardware.

DSVR (`http://www.rrzn.uni-hannover.de/dsvr.html`) as well as the implementation into PALM (Olbrich et al., 2001; Jensen et al., 2002) using its DVRP C and Fortran library interface (Chmielewski and Jensen, 2006) are already documented; a further description of is beyond the scope of this text. Here, the focus is on its main features, merits and limitations when applied to urban PALM simulations.

Urban applications push LES and turbulence visualization to their limits with $O(10^8)$ or even more grid points because they demand a) a large domain and b) a fine resolution. a) The large eddies above the urban fabric drive the circulation within, hence the domain must be large enough to capture these large eddies. b) If the flow within the urban canopy layer is of interest (e.g. pedestrian level conditions in street canyons like in chapter 6), the grid size must be small enough to explicitly resolve the *local* "large eddies" – limited in size by canyon width and height. Taking a) and b) together yields a very large total number of grid points, currently typically $O(10^8)$, increasing to $O(10^9 \sim 10^{10})$ in the near future.

This is where DSVR has one of its key strengths in PALM, because DSVR reduces graphic data volume by several orders of magnitude. With increasing number of grid points n per dimension, the data volume required for DSVR visualization of 3D geometric objects such as coloured isosurfaces and streamlines scales just with $O(n^2)$ and $O(n)$, respectively, in contrast to $O(n^3)$ for approaches (A) and (B) (Olbrich et al., 2001). An example with $n = 10^3$ (10^9 grid points) and $t = 10^4$ time steps illustrates the difference in resulting data volumes for scalar variables and vector fields:

---

[5]S. Olbrich, K. Chmielewski, N. Jensen, G. Gaus

[6]S. Olbrich, S. Manten

[7]"Anwendung der Tele-Immersion in Weitverkehrsnetzen" (Application of tele-immersion in long-distance networks), a joint project of RRZN, ZIB and IMUK, funded by BMBF, 2001-2003.

[8]"Untersuchung effizienter Methoden zur visuellen und haptischen tele-immersiven Exploration komplexer Volumen- und Strömungsdaten aus parallelisierten, dynamischen 3D-Simulationen" (Efficient Methods for Visualization in Tele-Immersive Applications), a joint project of RRZN, L3S, ZIM and IMUK, funded by DFG, 2005-2007.

	Approaches (A), (B)	DSVR isosurfaces slicers	DSVR streamlines
n	$O(n^3 \cdot t)$	$O(n^2 \cdot t)$	$O(n \cdot t)$
$n = 10^3$	$O(10^{13})$	$O(10^{10})$	$O(10^7)$
$\times 4$ B per scalar variable	$O(10\,\text{TB})$	$O(10\,\text{GB})$	$O(10\,\text{MB})$
$\times 12$ B per vector field	$O(100\,\text{TB})$	$O(10\,\text{GB})$	$O(10\,\text{MB})$

In practice, data output is often not required at *every* simulation time step but only at a fraction of the steps calculated, which further reduces the data volume. Even so, graphical processing of say $O(1 \sim 10\,\text{TB})$ following the standard approaches (A) or (B) would be beyond the computational capabilities of most installations; further compromises would be needed to reduce the data volume to a reasonable level. With DSVR, a mere rendering of $O(1\,\text{MB} \sim 1\,\text{GB})$ with well-equipped graphic hardware is still feasible in real-time; for $O(10^9 \sim 10^{10})$ grid points, however, even the performance of DSVR currently reaches its limits.

This means that for urban PALM simulations some types of visualization, especially fully 4D (animations), are currently only possible using DSVR.

DSVR does imply one important conceptual restriction to visualization. The pre-produced 3D DSVR scenes can be interactively visualized and navigated, but the *content* of the visualization cannot be changed – this would require a simulation re-run. Successful DSVR visualization therefore relies on *a priori* knowledge about the value range of the simulation output data. This is not required for the conventional approaches (A) and (B).

Another restriction of DSVR is that it focusses on qualitative analysis; quantitative statements for scientific analysis are difficult.

For urban applications of PALM the isosurface mode of DSVR has been extended to include the building shapes. An example is given in the following section.

5.3 Visualization example: Tokyo Shinjuku

One important application of urban LES is dispersion modelling. PALM contains the Lagrangian particle model of Weil et al. (2004) (for a general introduction see Helbig et al., 1999, chapter 11.2.2.3) that can be used both to simulate pollutant dispersion and simply to visualize the turbulent flow. For the visualization of unsteady turbulent flows using passive particle dispersion, particle heads (small spheres) and particle tails are passed on to DSVR as isosurfaces and streamlines, respectively. It is worth noting that the Lagrangian model and DSVR fit together well since they require almost the same *a priori* knowledge about the simulation, i.e. DSVR implies no additional conceptual restrictions compared to the Lagrangian model, nor vice versa.

Using urban Geographic information system (GIS) data for Shinjuku[9], a part of downtown Tokyo well-known for its high-rise office towers, a feasibility study was performed to demonstrate that it is possible to visualize large PALM data sets efficiently with DSVR. Figure 5.1 shows a snapshot of a simulation where passive particles with limited lifetime were released at regular intervals from four vertical line sources. The model covers an area of $1\,\text{km}^2$ with a resolution of $5\,\text{m}$. The model is initialized with a 1D pre-run and is then driven with $1\,\text{m s}^{-1}$ westerly wind applied at the domain top (Couette-type flow); the Coriolis force is switched off for simplicity. The simulation time is $3\,\text{h}$; DSVR particle data are output every $3.5\,\text{s}$.

---

[9]M. Kanda and CADCENTER Tokyo are acknowledged for providing the GIS data.
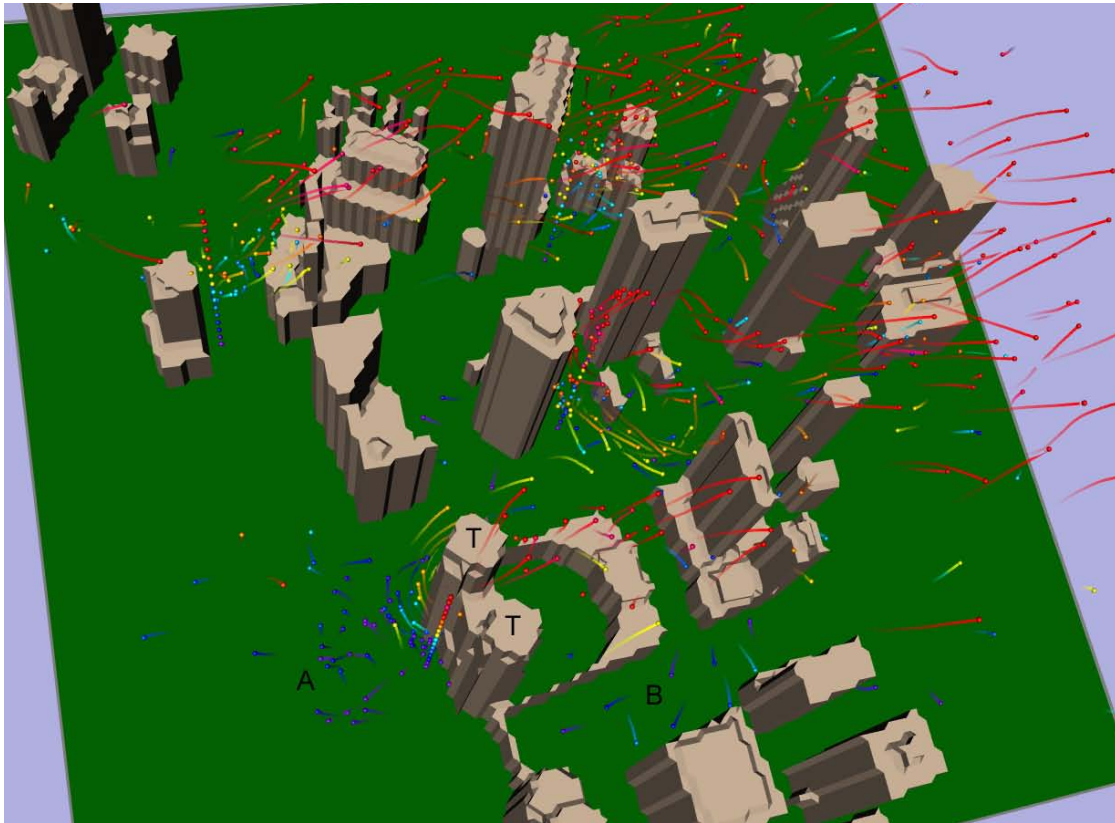
Figure 5.1: Instantaneous flow snap-shot of Tokyo Shinjuku in total view at $t =$1 h 54 min. For labels A, B and T see text.

Apart from the usual and expected vortex generation and channelling effects, this snapshot reveals two interesting points. The first point is the fairly large number of blue (= low-level) particles in the bottom left quadrant (labelled "A") upstream of the twin towers ("T"). These have all been released from the line source just before the twin towers. They have travelled far upstream. The second point is the WSW-ENE street canyon ("B") just south of the twin towers, where several blue (= low-level) particles travel upstream. In the course of the simulation, the flow in this particular street canyon is intermittent: periods of low-level upstream flow (Fig. 5.1) alternate with periods of low-level downstream flow (not shown). Intermittency is frequently observed in real street canyons (Christen, 2005; Dobre et al., 2005; Eliasson et al., 2006) and in wind tunnel studies (Meroney et al., 1996; Pavageau and Schatzmann, 1999; Louka et al., 2000). Both points illustrate the capabilities of urban LES: to reproduce unsteady or intermittent, i.e. time-dependent flow. Urban LES has the potential to improve pollution forecasts through instantaneous and peak concentration forecasts.

A close-up look at the wake region behind one of the tall buildings (Figure 5.2) reveals how different the instantaneous wake flow features can be from one time to another. Figure 5.2b is chosen to demonstrate that helical vortex structures such as those sketched by Robins and Macdonald (2001, Figs. 2.1 and 2.5 therein) are visible indeed in the instantaneous plots. However, they are rare, possible reasons being a) that they exist but are not picked up by the particle distribution, b) that they exist but are broken up or "masked" by superimposed stronger eddies or c) that they seldom exist in complex geometry flows.

In cooperation with IWF Knowledge and Media, Letzel et al. (2007) produced an animation of the 3 h simulation from three perspectives to give a more intuitive impression of the

(a) Large vortex structure at $t = 1\,\text{h}\,56\,\text{min}$

(b) Small helical vortex structure (yellow particle tails) at $t = 2\,\text{h}\,05\,\text{min}$
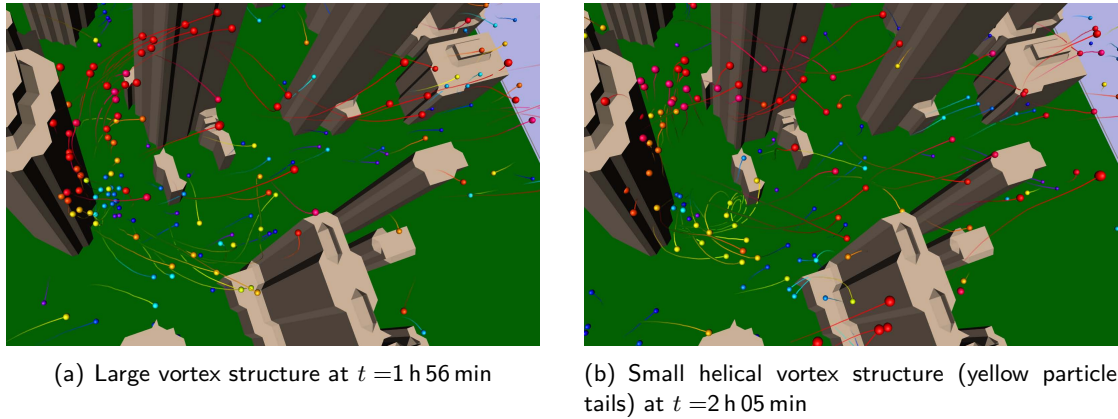
Figure 5.2: Instantaneous vortex structures in the wake of the Shinjuku Sumitomo building, close-up snap-shots taken from Letzel et al. (2007).

turbulent flow features and to show some of the capabilities of DSVR. The individual frames of the animation were produced by Letzel et al. (2007) using DSVR with high graphical resolution and were converted into a standard video stream by IWF that is downloadable from the IWF homepage.

Here, the Shinjuku GIS dataset has been used for a flow visualization feasibility test. Kataoka et al. (2007) used a larger version of this dataset for a comparison of the far-field wake effect between LES, RANS and a wind tunnel experiment. They showed that RANS overestimates the length and strength of the Shinjuku wake region, whereas LES correctly reproduces wind tunnel measurements. This is consistent with the findings of chapter 3 for the recirculation zone behind the single cube.

Further visualization feasibility tests have been performed with a high-resolution DEM dataset obtained from laser-scans for different city quarters of Hannover (not shown).

6 Application example: Hong Kong

This chapter is a revised and edited version of Letzel (2007). It is included here in order to demonstrate a) how the knowledge and techniques from the previous chapters can be combined and applied to answer practical urban climate questions and b) that today's supercomputers already provide the necessary computational power.

6.1 Introduction

The urban environment of Hong Kong suffers from two critical problems that are both harmful to its inhabitants: thermal discomfort and pollution. Responding to the outbreak of the Severe Acute Respiratory Syndrome (SARS) in 2003, based on the recommendations of Team Clean (2003) and in agreement with the objectives of the "First Sustainable Development Strategy for Hong Kong" promulgated in 2005, the Planning Department (PlanD) of The Government of the Hong Kong Special Administrative Region (HKSAR) commissioned the "Feasibility Study for Establishment of Air Ventilation Assessment System" (AVAS) and subsequently the current Feasibility Study "Urban Climatic Map and Standards for Wind Environment" (UCMap) to develop measures for improving the urban environment in Hong Kong.

The Urban Climatic Map is a tool for assisting planners and architects to understand and evaluate the effects of urban climate such as ventilation, thermal comfort and the urban heat island (cf. Helbig et al., 1999). It can be described as a "climatope" or "synthetic climate function maps". Different areas called climatopes are displayed, which are regarded to reveal distinct local climates. The idea behind this approach is that different urban structures like downtown or suburban areas, but also parks or larger water surfaces interact characteristically and distinctively with the urban atmosphere. Because the Urban Climatic Map relies mainly on GIS data (such as buildings and land-use), it needs to be calibrated for each city using wind tunnel benchmarking studies.

The AVAS executive summary (ES), UCMap inception report (IR) and UCMap working paper WP2A (Dpt of Arch; Chin Univ of Hong Kong, 2005, 2006a,b) form the background of the contractor's UCMap subproject "Large-Eddy Simulation Feasibility Study of Tsim Sha Tsui, Kowloon". The task of this project was to perform an LES using PALM for Tsim Sha Tsui (WP2A site 4) and report the velocity ratio as a measure of pedestrian level ventilation. The project belongs to the benchmarking studies (IR task 2). Due to the comparably high computational cost of LES, only one selected wind direction was to be simulated; hence the contribution of this project should not be viewed as a full benchmark but rather as a feasibility study. The main question behind is whether urban LES as an example of "advanced urban CFD" is already up and ready as an alternative technique to classical wind tunnel experiments for the analysis of wind environment (or thermal comfort) at pedestrian level (cf. the review by Mochida and Lun, 2006).

Section 6.2 describes the site selection and the set-up of the simulation performed. The results section 6.3 is divided in velocity ratio (6.3.1), tall building effects (6.3.2) and a brief comparison with other data (6.3.3), followed by discussion (6.4) and conclusions (6.5).
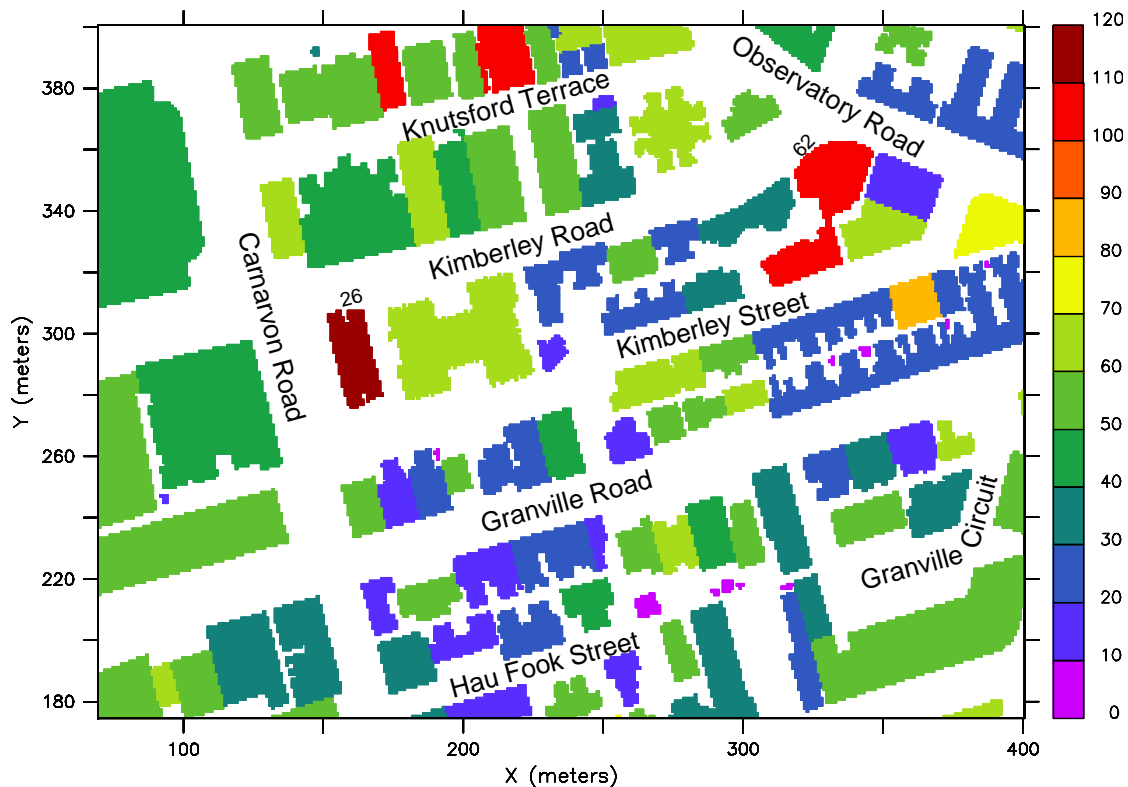
Figure 6.1: Assessment area of Tsim Sha Tsui (WP2A site 4) used in PALM. The rooftop heights given in m above ground were rastered with a horizontal resolution of $\Delta_h = 1$ m and a vertical resolution of $\Delta_z = 0.8$ m.

6.2 Site selection and simulation set-up

Leading members of the UCMap project team (Prof. Edward Ng, Prof. Lutz Katzschner) carefully selected Tsim Sha Tsui (WP2A site 4) for this LES feasibility study in consultation with the contractor with two main aspects in mind:

- Site 4 is a very high density city. For extremely large aspect ratios of up to $H/W = 10$ perpendicular flow gives a very poor pedestrian level ventilation (cf. case AR1000, Fig. 4.9h on page 53). Here LES operates at its limits. How can LES cope with these extreme conditions? Can LES deliver valuable results for AVAS under these conditions?

- Site 4 is almost flat. At the initial stage an LES feasibility study should concentrate on pure urban fabric effects and avoid possible interaction with non-flat topography. Therefore site 4 is suitable for this study.
  Once this LES feasibility study has been proven successful and useful for AVAS, more complicated test sites and/or the combination with non-flat topography may be selected for further investigations of the LES potential.

Hong Kong DEM data provided by PlanD were used for this study. AVAS methodology demands a model domain with a diameter of at least $4\,H$ that allows assessments within the inner assessment area with a diameter of $2\,H$, where H is the height of the tallest building on site (ES). The tallest building of site 4 located at 26 Kimberley Road has $H = 111.5$ m. With a rectangular model domain of $768\,\text{m} \times 512\,\text{m}$ and an assessment area of $330\,\text{m} \times 225\,\text{m}$

($3\,H \times 2\,H$, shown in Figure 6.1) the AVAS criteria are satisfied. Although the actual building heights are clustered at 10 m intervals for a better overview, Figure 6.1 still gives a good indication of the level of detail of the DEM building information. The available ground surface height data, however, were much less detailed and very coarse. At this stage the site was therefore considered as flat for the purpose of this LES feasibility study as outlined above.

However, a careful site inspection in October 2006 – after the PALM simulation was performed – revealed that this site has a range of ground topography features that should better not be approximated as flat: rather steep slopes parallel or perpendicular to streets as well as terraces. Also, a low building was detected attached to the tallest building on site, 26 Kimberley Road, that is not included in the DEM data. Any further LES should therefore try to include the topography and to obtain an updated DEM dataset. Also, there was a considerable amount of vegetation to the West, North and East of Tsim Sha Tsui; since the urban heat island effect can be mitigated e.g. by parks, any future simulations aiming at thermal issues should include such vegetation effects.

The AVAS methodology requires simulations for the 16 main wind directions for a full benchmark test and then calculates the site's wind velocity ratio as an average weighted by the annual frequency of these wind directions (ES). The resources available to this study allowed to perform only a single LES calculation so that as a first-order approximation the site's predominant wind direction had to be chosen. Data from the Hong Kong Observatory Tsim Sha Tsui station 42 m above ground and an MM5 simulation for the same location 450 m above ground (not shown) agree reasonably well with about 50-60% frequency of wind coming from the Eastern sector (45°-135°). Hence East wind (90°) was chosen for this study, and for this reason the model domain is extended in the East-West direction as mentioned above. For this wind direction the flow is continuously slightly uphill, hence the error of approximating the ground topography as flat is considered small.

The model domain size was $768\,\text{m} \times 512\,\text{m} \times 400\,\text{m}$ with a constant horizontal grid length of $\Delta_h = 1\,\text{m}$ and a constant vertical grid length of $\Delta_z = 0.8\,\text{m}$ up to $z = 200\,\text{m}$ stretched by 9% up to a maximum of $\Delta_{z,\text{max}} = 3.0$ m. This yields a more than fair horizontal resolution even for rather narrow streets like Kimberley Road and Kimberley Street according to Tseng et al. (2006), but smaller spaces such as the backyards in between Kimberley Street and Granville Road cannot be resolved well. The vertical resolution was chosen so that the velocity measurements at $z = 2$ m were at the third level of the staggered grid where the contribution of the SGS model is already small (less than 5% of the total momentum flux). Since LES results had to be produced quickly to be presented at the UCMap Workshop in October 2006, any desirable even finer resolution was out of question. On the workshop it turned out that with a total number of 10^8 grid points the present contribution was two orders of magnitude above other numerical contributions (10^6).

PALM simulated a neutral urban boundary layer without Coriolis effect driven by a direct body force $F = D_1 = -10^{-4}$ Pa m^{-1} and initialized with a suitable analytic velocity profile based on *a priori* information (cf. subsection 2.4.2 on page 18). The blocking effect of the site's dominant horizontal and vertical projections was accounted for. All results shown in this chapter are averaged over the last one hour of the 3 h simulation.
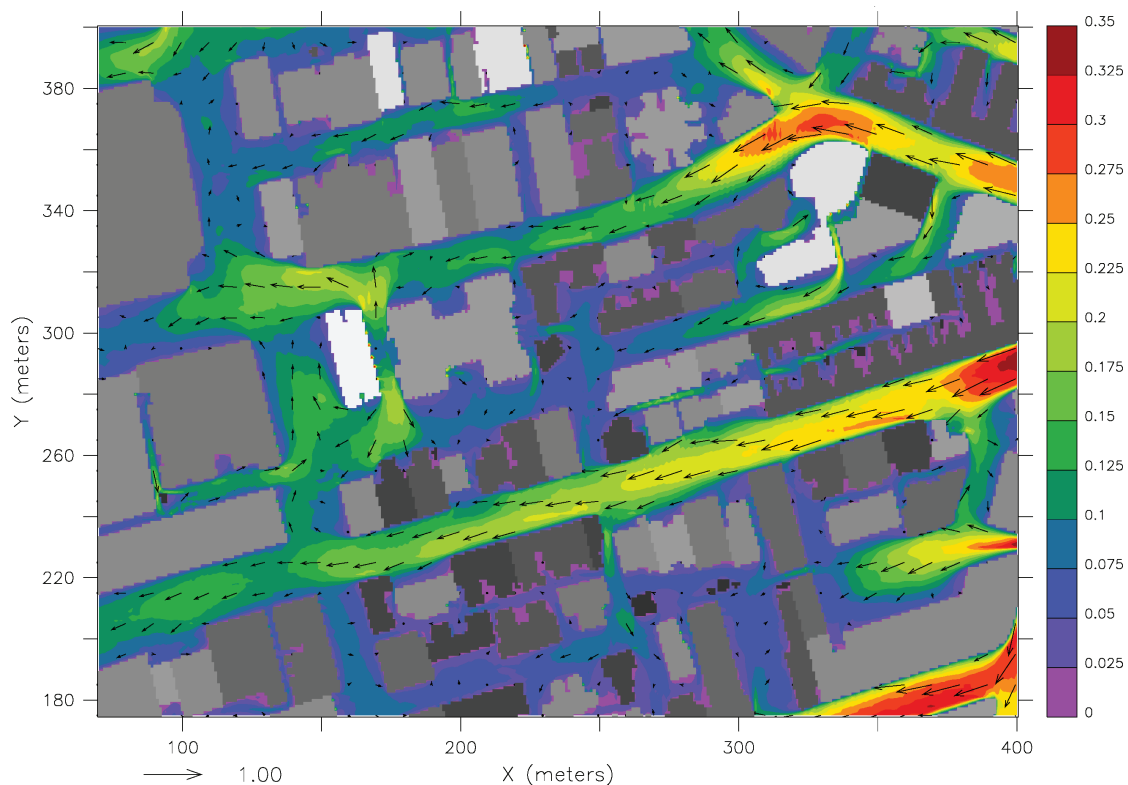
Figure 6.2: Velocity ratio map for Tsim Sha Tsui (WP2A site 4) for the East wind case as simulated by PALM. The building information of Fig. 6.1 is overlaid as greyscale here. Horizontal wind vectors at $z = 2\,$m are plotted at every 10th grid point, the reference arrow shows the length for a horizontal velocity of $1\,\text{m s}^{-1}$.

6.3 Results

6.3.1 Velocity ratio

ES defines the velocity ratio (for a single wind direction) as the ratio of absolute velocity at pedestrian height ($z = 2$ m) and absolute velocity well above the urban fabric where the wind is no more affected by urban roughness (here: top of the model domain at $z = 400$ m).

Figure 6.2 shows a velocity ratio map for Tsim Sha Tsui (WP2A site 4) for the East wind case as simulated by PALM where all model grid points at 2 m level were used for velocity ratio measurements. The superimposed horizontal wind vectors give additional information about the flow features at $z = 2$ m, especially the wind direction. The following features can be observed:

1. Long streets with (roughly) an E-W orientation benefit from a velocity ratio between 0.1 and 0.35 whereas values below 0.1 are typical of most other areas.

2. Streets that have a direct air path connecting to Chatham Road South (not shown, forms the Eastern boundary of this site's high-density area, lies just East of the assessment area) enjoy a high velocity ratio.

3. Their velocity ratio drops down rapidly once the air path is blocked (e.g. Granville Circuit) or slowly decreases further downstream.

83

4. The five tallest buildings (shown in white and very light grey) are associated with increased velocity ratios in their neighbourhood. Some upstream flow occurs.

5. Parts of the central axis of the narrow backyards in between Kimberley Street and Granville Road have velocity ratios between 0.1 and 0.2.

The above features allow the following conclusions and hypotheses:

1. Channeling is the dominant effect. This is good news because it occurs although none of the streets is directly aligned in the direction of the background wind.

2. Downstream penetration effect: Channeling does not prevent the velocity ratio from decreasing further downstream. Since Fig. 6.2 shows little evidence of increased mixing in spanwise direction, vertical mixing should be increased for continuity reasons.

3. Tall buildings, especially "isolated" ones, have the potential to cause first order effects – first order in a sense that they may cause local upstream flow and/or account for most of the locally measured velocity ratio.
   The tall buildings at 26 and 62 Kimberley Road, for example, cause a pronounced yet different flow field modification in their respective vicinity. This will be further discussed in subsection 6.3.2.

4. Despite of the model's very poor resolution in the narrow backyards in between Kimberley Street and Granville Road (down to as few as 3 grid points across) PALM does not predict velocity ratios too close to zero there. The narrow but moderately long fetch does seem to allow some channeling that is still picked up by PALM there.
   However, it is likely that PALM is over-diffusive and causes laminarized flow here; hence these velocity ratios should be interpreted with care here.

6.3.2 Flow modification potential of "isolated" tall buildings

Early papers (e.g. for Tokyo: Murakami et al., 1979; Sanada et al., 1980) already clearly show the potential of "sufficiently isolated" tall buildings to amplify the velocity ratio in their vicinity. Such effects are undesired in many cities, but in the densely built-up urban fabric of Hong Kong they may be very welcome.

   Two such tall buildings of the Tsim Sha Tsui LES shall now be briefly discussed. Figure 6.3a shows a W-E vertical cross-section of vertical velocity at y = 290 m through 26 Kimberley Street, the tallest building on site. This building is "sufficiently isolated": it shows typical features of classical flow around a single tall building:

1. Downwash of upstream air.

2. Footprints of side vortices (Fig. 6.2).

3. Amplification of vertical dispersion downstream.

Figure 6.3b shows the same cross-section at y = 350 m through 62 Kimberley Street. This tall building is not isolated enough: although the features of flow around this building are similar further aloft, for the East wind case their effects don't extend down to the pedestrian level because they are blocked by the almost directly attached lower houses upstream and downstream (cf. Figs. 6.1 and 6.2).

(a) $y = 290\,\mathrm{m}$ (b) $y = 350\,\mathrm{m}$
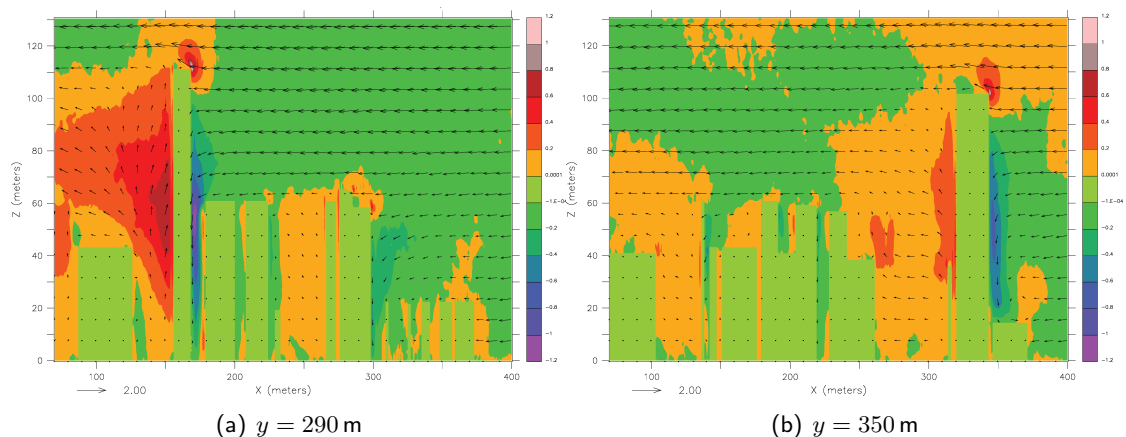
Figure 6.3: xz-cross sections of vertical velocity in m s^{-1} through the tall buildings of (a) 26 and (b) 62 Kimberley Road. Wind vectors in the xz-plane are plotted at every 10th grid point, the reference arrows show the length for a velocity of 2 m s^{-1}.

The amplification of vertical dispersion just downstream of the "sufficiently isolated" tall building at 26 Kimberley Street is also clearly demonstrated by a video of a 3D animation of passive Lagrangian particles released during this simulation (Letzel and Gaus, 2007, cf. chapter 5). Snapshots from four different perspectives from that animation 1:35h after simulation start are presented in Figures 6.4 and 6.5.

The observed amplification of vertical dispersion downstream of 26 Kimberley Road is consistent with a recent wind tunnel dispersion experiment by Barlow (2007) who found that single tall buildings serve as an elevated source of pollution (released at ground level) above the average UCL height. This implies that single tall buildings in an urban canopy of lower average height enhance vertical dispersion in their wake. The downside of the potential beneficial *local* effects of tall buildings is a reduced wind availability near the ground *further downstream* (e.g. Kataoka et al., 2007).

6.3.3 Comparison with other data

This LES feasibility study did not systematically explore the parameter space and hence allows no quantitative comparison with other data. Nevertheless a qualitative comparison shall be attempted here to show possible approaches.

Despite of the limited resources of this LES feasibility study it was decided to perform one comparative LES for Tokyo Shinjuku for the following reasons:

- Experience from some previous LES calculations of Shinjuku (Letzel et al., 2006, 2007) let one expect a much better velocity ratio.

- Tsim Sha Tsui together with Shinjuku would form two essentially different LES prototype simulations that could then be compared with the classification into "mid-to-high-rise apartment houses" versus "low-rise detached houses" suggested by Kubota and Miura (2002).

- DEM data of Shinjuku were already available.

Figure 6.6 shows velocity ratio frequency distibutions for Hong Kong Tsim Sha Tsui (gross buildings coverage ratio: 45.7%) versus Tokyo Shinjuku (24.8%) obtained from PALM East
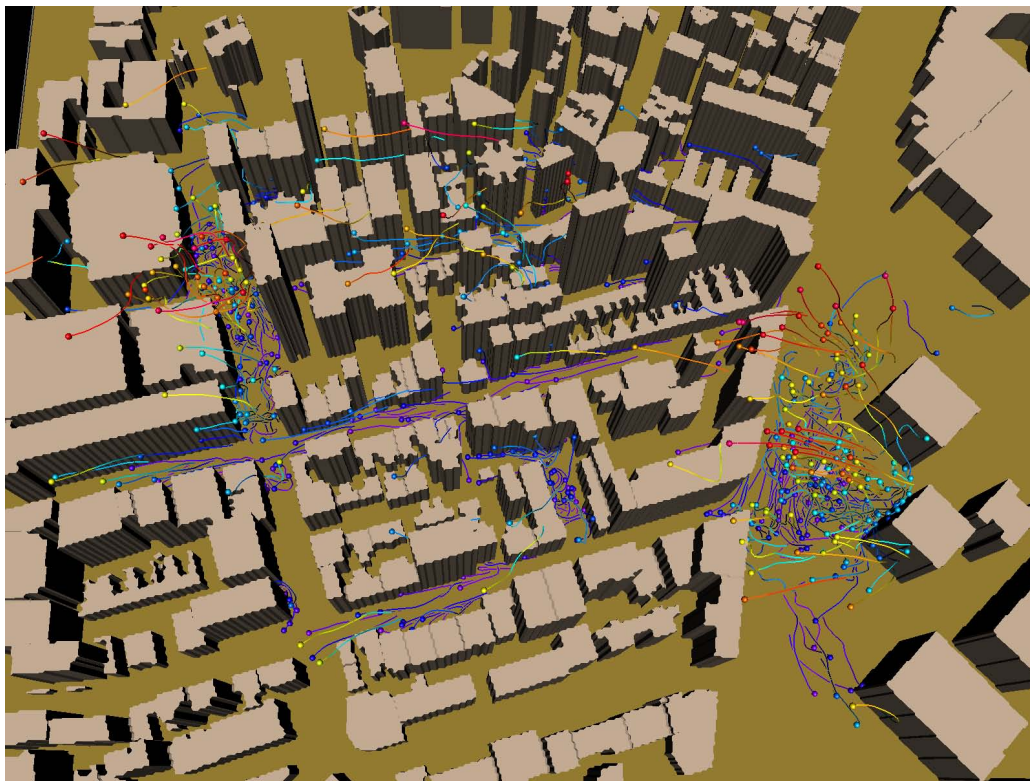
(a)
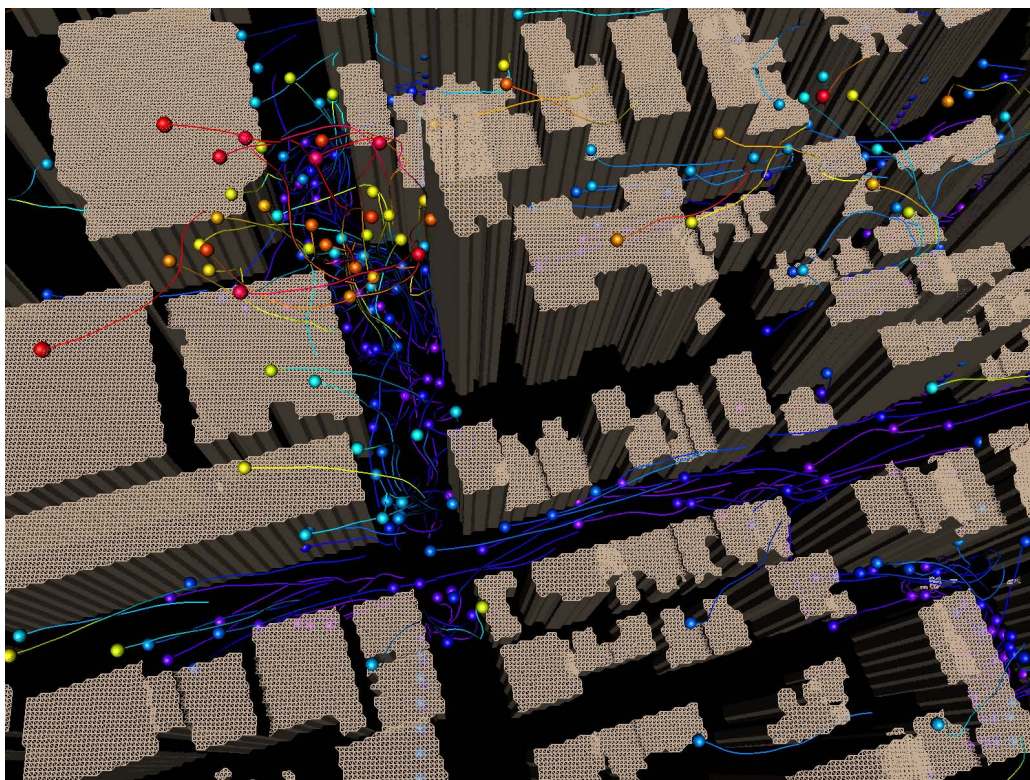
(b)

Figure 6.4: Snapshots of the Tsim Sha Tsui East wind PALM simulation from two different perspectives 1:35 h after simulation start. Lagrangian particle dispersion is used for flow visualization. Massless particles with limited lifetime are being released at selected locations at regular intervals. Colour indicates current particle height, tail length indicates speed. Taken from Letzel and Gaus (2007).
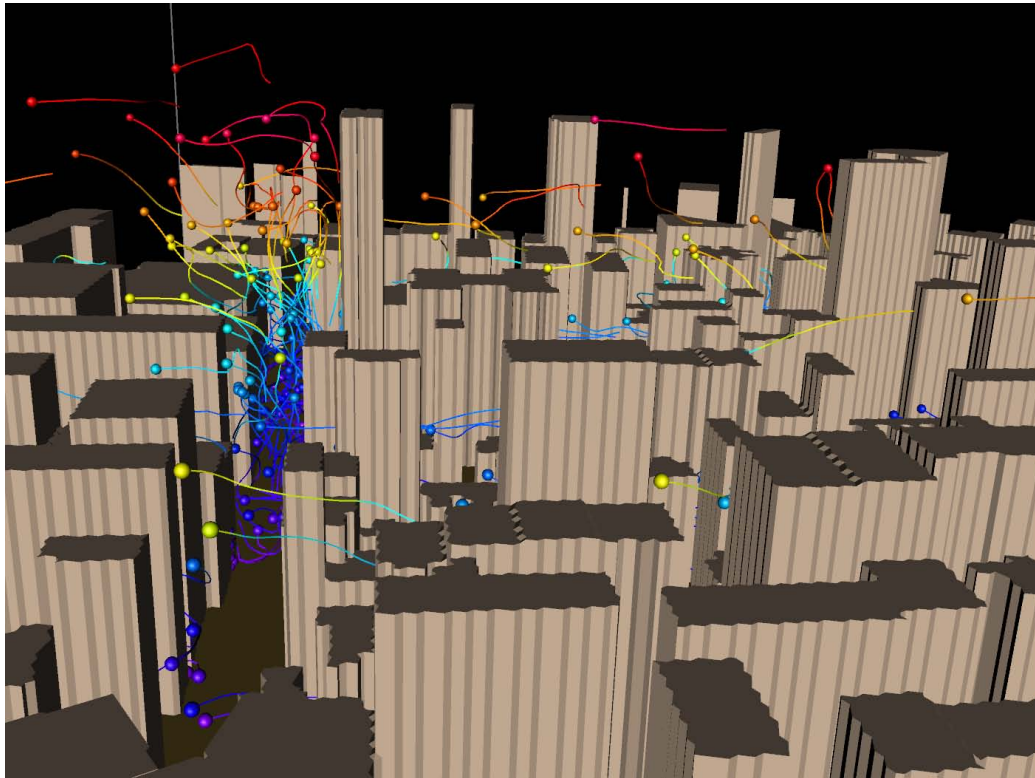
(a)
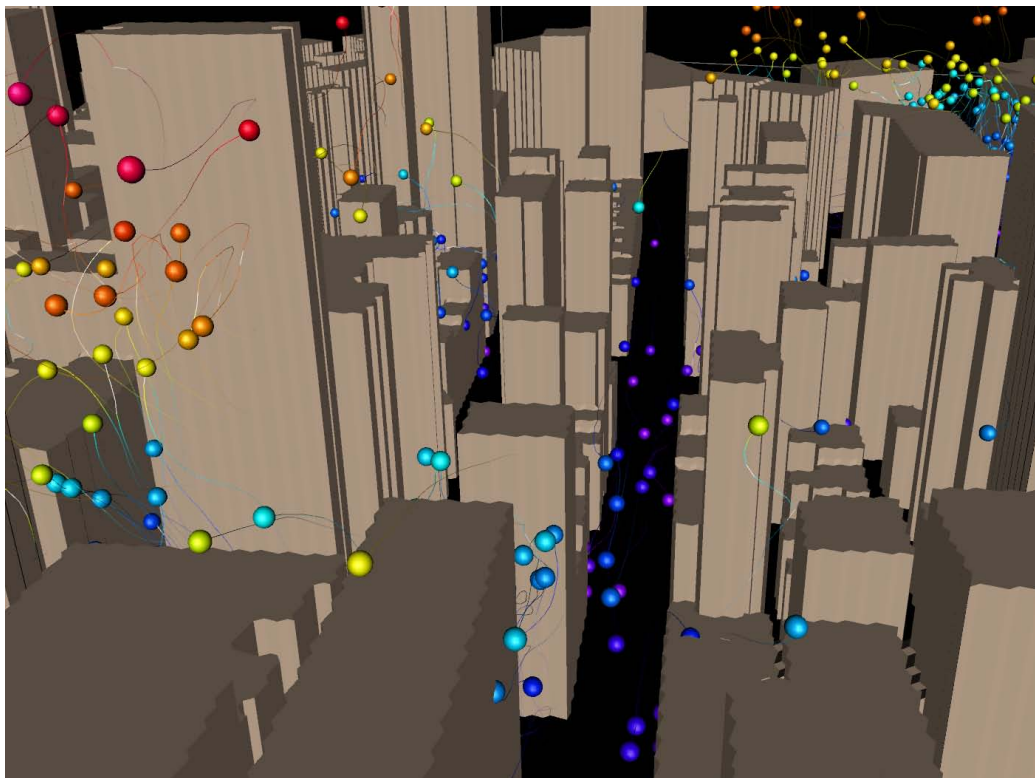
(b)

Figure 6.5: Snapshots of the Tsim Sha Tsui East wind PALM simulation from two further different perspectives 1:35 h after simulation start. For details refer to Fig. 6.4. Taken from Letzel and Gaus (2007).
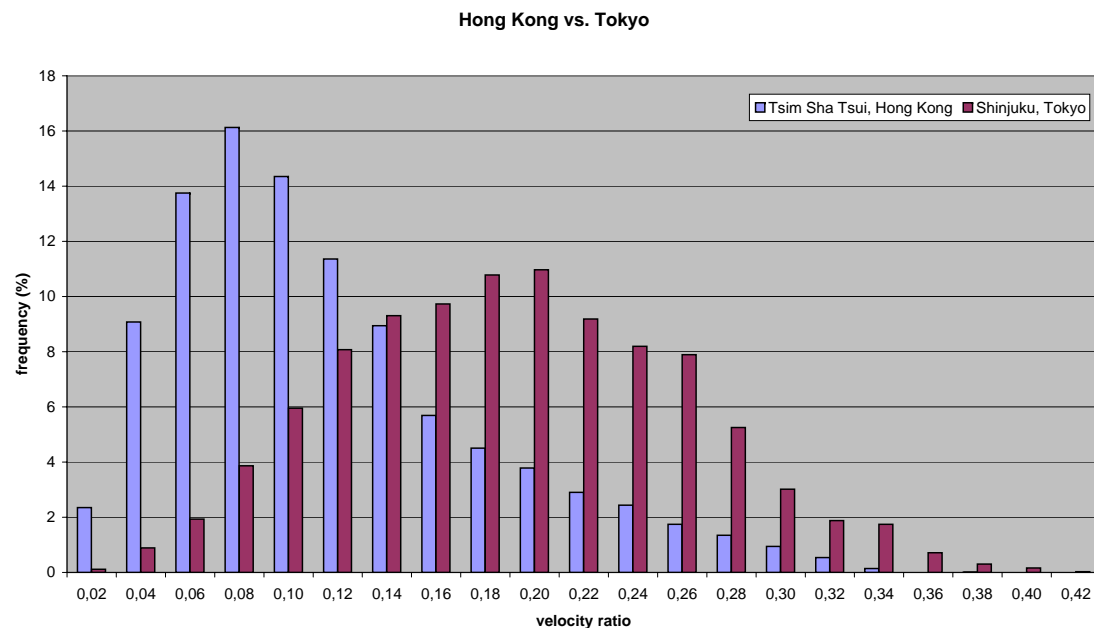
Hong Kong vs. Tokyo

Figure 6.6: Velocity ratio frequency distributions for Hong Kong Tsim Sha Tsui versus Tokyo Shinjuku obtained from the East wind simulations of PALM. Note the abszissa labelling "0.02" should be read as "0 to 0.02", "0.04" as "0.02 to 0.04" and so forth.

wind simulations. Again all model grid points at 2 m level outside buildings are used for velocity ratio measurements (over 40,000 samples). The site-averaged velocity ratios of Tsim Sha Tsui and Shinjuku are 0.1066 and 0.1818, respectively. The distribution for Tsim Sha Tsui is markedly right-skewed, whereas the distribution for Shinjuku is more symmetric and wider.

These findings agree qualitatively well with the wind tunnel study by Kubota and Miura (2002), although they define (wind) velocity ratio differently as wind velocity measured at 1.5 m (instead of 2 m) divided by wind velocity at the same height in a flat model without buildings (instead of undisturbed wind velocity aloft), which means that absolute figures are not comparable.

6.4 Discussion

The applicability of PALM for application of AVAS methodology to the complex urban fabric of Hong Kong cannot be ultimately proven on the basis of this study alone without suitable validation data. PALM does, however, produce correct qualitative differences between Tsim Sha Tsui and Tokyo Shinjuku – a site with a more open building morphology and smaller gross buildings coverage ratio – and shows qualitative agreement with the results of Kubota and Miura (2002), which indicates a good quality of the PALM results. IR demands "blinded", i.e. independent CFD and wind tunnel studies. Hence the results of Letzel (2007) were presented to the UCMap project team for comparison with wind tunnel data at their discretion following IR.

There are questions that deserve special attention when comparing PALM with wind tunnel data:

- The constant horizontal resolution of 1 m in PALM is a compromise and very small

narrow streets or very small courtyards cannot be well resolved. Can the wind tunnel do quality measurements at such critical locations to show how well or how badly PALM performs there (e.g. narrow backyards in between Kimberley Street and Granville Road)?

- PALM accounted for blocking effects of subgrid scale structures (e.g. horizontal and vertical projections typical of Tsim Sha Tsui). Can the wind tunnel directly model and quantify these effects?

Any answers to these questions would gratefully appreciated since they may help to improve PALM quality.

Cost-benefit analysis   Jiménez (2003) asks whether numerical simulations will ever replace experiments in high Reynolds number turbulence and suggests that, despite of some still unsolved problems, they eventually will. Hanjalic (2005) deals with a possible "follow-up" question whether RANS will survive LES and discusses the merits, shortcomings and potantial pitfalls of RANS, LES and their respective derivates (URANS, TRANS; VLES).

The PALM simulation for Tsim Sha Tsui lasted 3 ¼ days net on 128 CPUs of the parallel supercomputer IBM Regatta p690 series of the North German Supercomputing Center (HLRN) and had a net market value of 44 k€ according to `http://www.hlrn.de/org/Entgeltordnung.html`. The comparative simulation for Tokyo Shinjuku lasted only 21 hours net also on 128 CPUs of the HLRN and had a net market value of 3 k€. A full wind velocity ratio LES study for all 16 main wind directions would thus be on the order of 700 k€ or 50 k€ net respectively, whereas ES quotes an equivalent of 40 k€ for a full wind tunnel study of a 2-hectare site that takes about 1 to 3 months to conduct.

Once more it should be noted that both Tsim Sha Tsui and Shinjuku LES were feasibility studies and limited resources did not allow to explore the parameter space, which means that their respective costs may only be viewed as an approximate guidance.

The main reason for the striking cost difference between these simulations is the difference in site characteristics. Sites with coarsely spaced buildings allow a coarser horizontal resolution (e.g. $\Delta_h = 2$ m for Tokyo Shinjuku) than sites with very narrow street canyons (e.g. $\Delta_h = 1$ m or less for Tsim Sha Tsui).

One the one hand, the cost of PALM can be reduced to achieve a better competitiveness with wind tunnel studies. Possible strategies for a *short-term cost reduction* include a reduction of the total number of grid points or iterations. The implementation of a dynamic SGS model could allow a reduction of grid resolution without sacrificing model accuracy. Horizontal grid stretching or adaptive grids could also be used, but they don't alleviate the timestep problem. Another strategy could be to use special LES-based or hybrid RANS-LES modelling approaches (DES, MILES, VLES). The rising computational power itself will bring about a *mid-term cost reduction* that is expected to be sufficient within only a few years. The LES community has long recognized the demand for and the prospects of application of LES to practical urban research (e.g. Murakami, 1997; Murakami et al., 1999; Letzel et al., 2005; Hanna et al., 2006; Mochida and Lun, 2006; Tseng et al., 2006; Kataoka et al., 2007; Letzel, 2007).

On the other hand, it should be realized that PALM has two extra benefits compared to wind tunnel studies: 1) PALM can easily be used for extensive parameter studies (simulations for different cases can run simultaneously, which gives a speed-up compared to the wind tunnel where only one case at a time can be investigated), 2) PALM can provide fully 4D data at no extra cost (in other words, time series at each grid point of the 3D model domain),

whereas wind tunnel cost scales with the number of measurements. This means that the above figures should also be interpreted in view of the quantity of measurements that can be delivered at a given cost by wind tunnel and LES studies, respectively.

Experience from other industries such as the aircraft construction or automobile industries suggests that urban LES will find its due place in the coming years given a further rising computational power. Needless to say, urban LES models will always require a proper validation that is best done with wind tunnel reference experiments, and LES also always requires careful sensitivity studies (e.g. on grid resolution) to ensure quality results.

6.5 Conclusions

With the delivery of the velocity ratio for the East wind case the goal of this subproject has been accomplished. There remain, however, open questions that were returned to the UCMap project team for further investigation at their discretion.

The wind velocity ratio situation of Tsim Sha Tsui is severe based on the PALM East wind simulation. Easterly winds prevail at this site, but despite considerable channeling the site's average velocity ratio for East wind is only 0.1066. 55% of the assessment area have a local velocity ratio below 0.1. The situation would be even worse if the site's relatively sparse very tall buildings did not exist: the more uniform building height would cause more skimming flow.

Recommended planning suggestions for enhanced Tsim Sha Tsui East wind comfort include broadening and, if possible, a connection of effective air paths. For example, a larger cross-section of the presently very narrow connection between Granville Circuit and Chatham Road South would allow more air to enter the site. Ideally, this air could then be given the chance to penetrate further by establishing a connection with Hau Fook Street.

Another possible planning suggestion already suggested by ES is to change the design of the projections from horizontal into vertical – this should prevent velocity ratios from dropping down too quickly along streets with channeling.

7 Summary and Conclusions

Within the framework of the present study, the parallel large-eddy simulation model PALM has been extended to explicitly resolve flow around solid obstacles in the neutral and thermally stratified boundary layer. This work forms the basis of future applications for example in the fields of wind engineering and urban climate research. The latter was the subject of this thesis. A commissioned, applied urban LES study for an interdisciplinary research project in Hong Kong was also part of this thesis.

Since urban LES involves a huge number of grid points, the obstacle code had to be implemented in a way to ensure optimal performance on the various architectures of today's supercomputers. This has successfully been achieved by a modification of the conventional mask method using terrain-following lower loop indices.

The urban PALM code was successfully validated with a large LES and RANS model inter-comparison based on a well-documented wind tunnel reference experiment. The experiment featured a single cube in a shallow, fully turbulent, neutral channel flow. The validation showed that with increasing grid resolution the PALM results converged to a solution that is as good as other LES models, comparable to the wind tunnel reference measurements and superior to RANS models. The urban PALM version is not yet validated for thermally stratified flow.

Properly validated LES models can complement wind tunnel studies in two main ways, if they are run at sufficiently high grid resolution: 1) LES can easily be used for extensive parameter studies (simulations for different cases can run simultaneously, which gives a speed-up compared to the wind tunnel where only one case at a time can be investigated), 2) LES can provide fully 4D data at no extra cost (in other words, time series at each grid point of the 3D model domain), whereas wind tunnel cost scales with the number of measurements. This means that LES is also well-suited to serve as an additional source of reference data for validation of RANS models.

> "The urban wind field is rarely simple" (Landsberg, 1981) —

as expected, this experience was a common thread running through all chapters.

Already the single cube of the validation experiment exhibited a complex 3D flow topology, even in the time-average.

The flow was also found to be fully 3D in the limit of an infinitely long (2D) urban street canyon. A parameter study of the turbulence characteristics of the urban street canyon circulation driven by perpendicular wind for neutral and convective boundary layers constituted the main part of this thesis. The most important results are: 1) A new concept of a "cavity shear layer" was developed that complements classical free shear layer concepts. 2) For the first time in urban LES Kelvin-Helmholtz instabilities were identified at the top of the urban street canyon. This is important for modelling urban dispersion e.g. using RANS models, because it means that the canyon circulation is more intermittent than the apparently "steady" RANS results might suggest. 3) Integral turbulence profiles in deep canyons were found to vertically scale with canyon depth. This is relevant for urban canopy parameterizations in larger-scale meteorological models; it is hoped that the findings of

the present study can contribute to the further development of such parameterizations. The main implications are that 3D models should always be used to simulate turbulent even in apparently 2D geometries, and the intermittency of turbulent flow should not be underestimated, because the steady canyon vortex is mainly a result of the time-averaging process in LES or the RANS approach as such, respectively.

PALM includes a built-in, parellel, on-the-fly turbulent flow visualization technique that uses the Distributed Simulation and Virtual Reality Environment DSVR together with PALM's integrated Lagrangian passive particle dispersion model. This visualization technique was extended and applied to visualize the turbulent flow within a real urban canopy. Visualization feasibility studies showed the complex, instantaneous turbulent flow structures for various city quarters of Tokyo, Hong Kong and Hannover.

Within the framework of this study PALM was also used for a commissioned, applied urban LES study for an interdisciplinary research project in Hong Kong. The requirement to report local scale pedestrian-level ventilation in the dense urban fabric of Tsim Sha Tsui, Kowloon, downtown Hong Kong, implied a fine grid resolution resulting in a large number of 10^8 grid points. The velocity ratio in Tsim Sha Tsui was found to be very low, even compared to other dense cities such as Shinjuku, downtown Tokyo. However, it could be shown that isolated tall buildings have the potential to locally improve ground-level ventilation.

Further research For further research, it is proposed to extend this study to realistic boundary layer depths, inflow-outflow boundary conditions with turbulent inflow, an ensemble of different approaching wind directions, and different roof geometries.

Further goals could be the inclusion of more relevant urban processes such as anthropogenic heat, solar radiation and dispersion of pollutants.

A representation of different roof geometries or, generally speaking, non-vertical walls could be achieved by making use of the full potential of immersed boundary methods (Mittal and Iaccarino, 2005), for example using the ABMAC (Viecelli, 1971) or FAVOR (Hirt, 1993) approach as suggested by Mochida (2006).

An ensemble of different wind direction implies also off-perpendicular and off-parallel flow (e.g. 45° approaching ambient wind direction). The studies of Becker (1996); Becker et al. (2002); Robins and Macdonald (2001); Thomas and Williams (1999); Kono and Kusunoki (2005) and Eliasson et al. (2006) offer additional data for validation of such cases. Ideally a validation should also be done for complex urban geometries using reference data sources such as the planned urban version of the CEDVAL database (VDI/DIN Kommission Reinhaltung der Luft, 2005) or the set of wind tunnel benchmarks tests for the urban CFD guideline of the Architectural Institute of Japan (e.g. Tominaga et al., 2005).

Overall, this study clearly demonstrated the promising potential of urban large-eddy simulation for both fundamental and applied urban research. Given the ever rising computational power, properly validated urban LES could mature to a powerful research tool within the next few years.

Bibliography

The end of each entry lists the page number(s) where the citation occurs.

Ahmad, K., Khare, M. and Chaudhry, K. K. (**2005**): Wind tunnel simulation studies on dispersion at urban street canyons and intersections – a review. *J. Wind Eng. Ind. Aerodyn.*, **93**, 697–717. 37, 38

Albrecht, F. and Grunow, J. (**1935**): Ein Beitrag zur Frage der vertikalen Luftzirkulation in der Großstadt. *Meteorol. Z.*, **52**, 103–108. 37

Arakawa, A. and Lamb, V. R. (**1977**): Computational design of the basic dynamical processes of the UCLA general circulation model. In: **J. Chang** (ed.), *General circulation models of the atmosphere*, Academic Press, *Methods in Computational Physics*, vol. 17. pp. 173–265. 10

Arnfield, A. J. (**2003**): Two decades of urban climate research: A review of turbulence, exchanges of energy and water, and the urban heat island. *Int. J. Climatol.*, **23**, 1–26. 1

Asselin, R. (**1972**): Frequency filter for time integrations. *Mon. Wea. Rev.*, **100**, 487–490. 14

Baik, J.-J. and Kim, J.-J. (**1999**): A numerical study of flow and pollutant dispersion characteristics in urban street canyons. *J. Appl. Meteor.*, **38**, 1576–1589. 39, 46, 60

Baik, J.-J., Park, R.-S., Chun, H.-Y. and Kim, J.-J. (**2000**): A laboratory model of urban street-canyon flows. *J. Appl. Meteor.*, **39**, 1592–1600. 44, 50, 60

Barlow, J. F. (**2007**): Personal communication. 85

Barlow, J. F. and Pascheke, F. (**2006**): The effect of varying roof morphology on urban canopy ventilation. In: *Sixth Intl. Conf. on Urban Climate (ICUC-6)*. Göteborg, Sweden. 44, 72

Batchvarova, E. and Gryning, S.-E. (**2006**): Progress in urban dispersion studies. *Theor. Appl. Climatol.*, **84**, 57–67. 1, 40

Båth, M. (**1974**): *Spectral Analysis in Geophysics*. Developments in Solid Earth Geophysics. Elsevier Scientific Publishing Company, Amsterdam, 563 pp. 67

Becker, S. (**1996**): *Umströmung von dreidimensionalen Hindernissen in Wandgrenzschichten*. Ph.D. thesis, Technische Universität Dresden, Fakultät für Maschinenwesen. 92

Becker, S., Lienhart, H. and Durst, F. (**2002**): Flow around three-dimensional obstacles in boundary layers. *J. Wind Eng. Ind. Aerodyn.*, **90**, 265–279. 92

Belcher, S. E. (**2005**): Mixing and transport in urban areas. *Phil. Trans. R. Soc. A*, **363**, 2947–2968. 1, 3, 40, 49

Best, M. J. (**2006**): Progress towards better weather forecasts for city dwellers: from short range to climate change. *Theor. Appl. Climatol.*, **84**, 47–55. 3

Bloomfield, P. (**2000**): *Fourier Analysis of Time Series*. Wiley, 2nd edn., 261 pp. 67

Bohnenstengel, S., Schlünzen, K. H. and Grawe, D. (**2004**): Influence of thermal effects on street canyon circulations. *Meteorol. Z.*, **13**, 381–386. 44, 70, 71

Boussinesq, J. (**1903**): *Theorie Analytique de Chaleur*, Gauthier-Villars, Paris, vol. 2. pp. 154–176. 8

Breuer, M. (**2002**): *Direkte Numerische Simulation und Large-Eddy Simulation turbulenter Strömungen auf Hochleistungsrechnern*. Shaker Verlag, Aachen. ISBN 3-8265-9958-6, 433 pp. 4, 8, 9, 14, 15, 16, 18, 19, 21, 24, 26, 28, 30, 31, 32, 34, 35, 49, 74

Breuer, M., Lakehal, D. and Rodi, W. (**1996**): Flow around surface mounted cubical obstacle: comparison of LES and RANS results. In: **M. Deville, S. Gavrilakis and I. L. Rhyming** (eds.), *Computation of Three-Dimensional Flows*, Vieweg, Braunschweig, *Notes on Numerical Fluid Mechanics*, vol. 53. pp. 22–29. Proceedings of the IMACS-COST conference, Lausanne, Sept. 1995. 19, 21

Briscolini, M. and Santangelo, P. (**1989**): Development of the mask method for incompressible unsteady flows. *J. Comput. Phys.*, **84**, 57–75. 7, 10

Britter, R. E. and Hanna, S. R. (**2003**): Flow and dispersion in urban areas. *Ann. Rev. Fluid Mech.*, **35**, 469–496. 1, 3, 40, 64, 67

Brown, M. J., Boswell, D., Streit, G., Nelson, M., McPherson, T., Hilton, T., Pardyjak, E. R., Pol, S., Ramamurthy, P., Hansen, B., Kastner-Klein, P., Clark, J., Moore, A., Walker, D., Felton, N., Strickland, D., Brook, D., Princevac, M., Zajic, D., Wayson, R., MacDonald, J., Fleming, G. and Storwold, D. (**2004**): Joint URBAN 2003 street canyon experiment. In: *AMS Annual Meeting Symposium on Planning, Nowcasting, and Forecasting in the Urban Zone*. Seattle WA, J7.3. 72

Brown, M. J., Lawson, R. E., Jr., DeCroix, D. S. and Lee, R. L. (**2000**): Mean flow and turbulence measurements around a 2-D array of buildings in a wind tunnel. In: *11th Joint AMS/AWMA Conference on the Application of Air Pollution Meteorology, Long Beach, CA, January 2000.* 4A.2. Also available as LA-UR-99-5395, Los Alamos National Laboratory, Los Alamos, New Mexico 87545. 40, 44, 45

Burgers, J. M. (**1948**): A mathematical model illustrating the theory of turbulence. In: **R. von Mises and T. von Kármán** (eds.), *Advances in Applied Mechanics*, Academic Press, New York. pp. 171–199. 14

Businger, J. A., Wyngaard, J. C., Izumi, Y. and Bradley, E. F. (**1971**): Flux-profile relationships in the atmospheric surface layer. *J. Atmos. Sci.*, **28**, 181–189. 16

Ca, V. T., Asaeda, T., Ito, M. and Armfield, S. (**1995**): Characteristics of wind field in a street canyon. *J. Wind Eng. Ind. Aerodyn.*, **57**, 63–80. 39

Cabot, W. and Moin, P. (**1999**): Approximate wall boundary conditions in the large-eddy simulation of high Reynolds number flows. *Flow, Turbulence and Combustion*, **63**, 269–291. 16

Cai, X. (**2006**): Personal communication. 17

Castro, I. P., Cheng, H. and Reynolds, R. (**2006**): Turbulence over urban-type roughness: Deductions from wind-tunnel measurements. *Boundary-Layer Meteorol.*, **118**, 109–131. 36

Caton, F., Britter, R. E. and Dalziel, S. (**2003**): Dispersion mechanisms in a street canyon. *Atmos. Environment*, **37**, 693–702. 44, 45, 46, 47, 49

Chabni, A., Le Quéré, P., Tenaud, C. and Laatar, H. (**1998**): Modelling of pollutant dispersion in urban street canyons by means of a large-eddy simulation approach. *Int. J. Vehicle Des.*, **20**, 88–95. 39

Chan, T. L., Dong, G., Leung, C. W., Cheung, C. S. and Hung, W. T. (**2002**): Validation of a two-dimensional pollutant dispersion model in an isolated street canyon. *Atmos. Environment*, **36**, 861–872. 39

Cheng, H. and Castro, I. (**2002**): Near wall flow over urban-like roughness. *Boundary-Layer Meteorol.*, **104**, 229–259. 62, 64, 67

Chlond, A. (**1994**): Locally modified version of Bott's advection scheme. *Mon. Wea. Rev.*, **122**, 111–125. 14

Chmielewski, K. and Jensen, N. (**2006**): *DVRP Library Documentation – A Parallel Library to Support 3D-Visualization and Computational Steering*. RRZN Leibniz Universität Hannover, 69 pp. URL http://www.rrzn.uni-hannover.de/libdvrp.html. 75, 76

Chorin, A. J. (**1968**): Numerical solution of the Navier-Stokes equations. *Math. Comp.*, **22**, 745–762. 14

Chorin, A. J. (**1969**): On the convergence of discrete approximations to the Navier-Stokes equations. *Math. Comp.*, **23**, 341–353. 14

Christen, A. (**2005**): *Atmospheric Turbulence and Surface Energy Exchange in Urban Environments – Results from the Basel Urban Boundary Layer Experiment (BUBBLE)*. Ph.D. thesis, University of Basel. 3, 4, 40, 44, 64, 67, 68, 72, 78

Christen, A., Vogt, R. and Rotach, M. W. (**2003**): Profile measurements of selected turbulence parameters over different urban surfaces. In: *Fourth International Conference on Urban Air Quality*. Prague, pp. 408–411. 40, 62, 67, 73

Coceal, O., Thomas, T. G., Castro, I. P. and Belcher, S. E. (**2006**): Mean flow and turbulence statistics over groups of urban-like cubical obstacles. *Boundary-Layer Meteorol.*, **121**, 491–519. 36, 40, 49, 62, 63

Collier, G. (**2006**): The impact of urban areas on weather. *Quart. J. R. Meteorol. Soc.*, **132**, 1–25. 1

Cui, Z., Cai, X. and Baker, C. J. (**2004**): Large-eddy simulation of turbulent flow in a street canyon. *Quart. J. R. Meteorol. Soc.*, **130**, 1373–1394. 39, 40, 44, 47, 49, 57, 72

Dabberdt, W. F., Ludwig, F. L. and Johnson, W. B., Jr. (**1973**): Validation and applications of an urban diffusion model for vehicular pollutants. *Atmos. Environment*, **7**, 603–618. 38

Deardorff, J. W. (**1980**): Stratocumulus-capped mixed layers derived from a three-dimensional model. *Boundary-Layer Meteorol.*, **18**, 495–527. 15

DePaul, F. T. and Sheih, C. M. (**1985**): A tracer study of dispersion in an urban street canyon. *Atmos. Environment*, **19**, 555–559. 38

DePaul, F. T. and Sheih, C. M. (**1986**): Measurements of wind velocities in a street canyon. *Atmos. Environment*, **30**, 455–459. 38, 72

Dobre, A., Arnold, S. J., Smalley, R. J., Boddy, J. W. D., Barlow, J. F., Tomlin, A. S. and Belcher, S. E. (**2005**): Flow field measurements in the proximity of an urban intersection in London, UK. *Atmos. Environment*, **39**, 4647–4657. 78

Dpt of Arch; Chin Univ of Hong Kong (**2005**): *Feasibility Study for Establishment of Air Ventilation Assessment System – Executive Summary*. Tech. rep., Planning Department, The Government of the Hong Kong Special Administrative Region. 44pp. 80

Dpt of Arch; Chin Univ of Hong Kong (**2006**a): *Urban Climatic Map and Standards for Wind Environment – Feasibility Study – Inception Report*. Tech. rep., Planning Department, The Government of the Hong Kong Special Administrative Region. 45pp. 80

Dpt of Arch; Chin Univ of Hong Kong (**2006**b): *Urban Climatic Map and Standards for Wind Environment – Feasibility Study – Working Paper 2A: Methodologies of Area Selection for Benchmarking. Tech. rep.*, Planning Department, The Government of the Hong Kong Special Administrative Region. 60pp. 80

Dutton, J. A. and Fichtl, G. H. (**1969**): Approximate equations of motion for gases and liquids. *J. Atmos. Sci.*, **23**, 241–254. 8

Eliasson, I., Offerle, B., Grimmond, C. S. B. and Lindqvist, S. (**2006**): Wind fields and turbulence statistics in an urban street canyon. *Atmos. Environment*, **40**, 1–16. 40, 44, 47, 51, 64, 67, 72, 73, 78, 92

Etling, D. (**1996**): *Theoretische Meteorologie. Eine Einführung*. Vieweg & Sohn Verlagsgesellschaft, Braunschweig/Wiesbaden, 1st edn., 318 pp. 8

Etling, D. (**2002**): *Theoretische Meteorologie. Eine Einführung*. Springer, Berlin/Heidelberg/New York, 2nd edn., 354 pp. 8, 16, 18

Fernando, H. J. S., Lee, S. M., Anderson, J., Princevac, M., Pardyjak, E. and Grossman-Clarke, S. (**2001**): Urban fluid mechanics: Air circulation and contaminant dispersion in cities. *Env. Fluid Mech.*, **1**, 107–164. 1

Ferziger, J. H. and Perić, M. (**2002**): *Computational Methods for Fluid Dynamics*. Springer, 3rd edn., 423 pp. 4, 14

Finnigan, J. (**2000**): Turbulence in plant canopies. *Ann. Rev. Fluid Mech.*, **32**, 519–571. 45

Foken, T. (**2006**): 50 years of the Monin-Obukhov Similarity Theory. *Boundary-Layer Meteorol.*, **119**, 431–447. 16

Fröhlich, J. (**2006**): *Large Eddy Simulation turbulenter Strömungen*. Teubner, Wiesbaden. ISBN 3-8351-0104-8, 416 pp. 4, 8, 9, 10, 14, 15, 16, 17, 18

Garratt, J. R. (**1992**): *The atmospheric boundary layer*. Cambridge University Press, Cambridge, 316 pp. 16

Gaus, G. (**2006**): Personal communication. 74

Germano, M., Piomelli, U., Moin, P. and Cabot, W. H. (**1991**): A dynamic subgrid-scale eddy viscosity model. *Phys. Fluids A*, **3**, 1760–1765. 24

Ghia, U., Ghia, K. N. and Shin, C. T. (**1982**): High-Re solutions for incompressible flow using the Navier-Stokes equations and a multigrid method. *J. Comput. Phys.*, **48**, 387–411. 39

Grimmond, C. S. B. (**2006**): Progress in measuring and observing the urban atmosphere. *Theor. Appl. Climatol.*, **84**, 3–22. 40

Gropp, W., Lusk, E. and Skjellum, A. (**1999**): *Using MPI. Portable parallel programming with the Message-Passing Interface*. MIT Press, Cambridge, Mass., 2nd edn., 371 pp. 18

Gryschka, M. and Raasch, S. (**2005**): Roll convection during a cold air outbreak: A large eddy simulation with stationary model domain. *Geophys. Res. Lett.*, **32 (L14805,doi:10.1029/2005GL022872)**, 1–5. 10

Haber, R. B. and McNabb, D. A. (**1979**): Visualization idioms: A conceptual model for scientific visualization systems. In: **B. B. Schriver, G. M. Nielson and L. J. Rosenblum** (eds.), *Visualization in Scientific Computing*, IEEE Computer Society Press, Los Alamitos. pp. 74–93. 74

Hanjalic, K. (**2005**): Will RANS survive LES? A view of perspectives. *J. Fluids Eng.*, **127**, 831–839. 89

Hanna, S. R., Brown, M. J., Camelli, F. E., Chan, S. T., Coirier, W. J., Hansen, O. R., Huber, A. H., Kim, S. and Reynolds, R. M. (**2006**): Detailed simulations of atmospheric flow and dispersion in downtown Manhattan. *Bull. Am. Meteorol. Soc.*, **87**. 89

Hanna, S. R., Tehranian, S., Carissimo, B., MacDonald, R. W. and Lohner, R. (**2002**): Comparisons of model simulations with observations of mean flow and turbulence within simple obstacle arrays. *Atmos. Environment*, **36**, 5067–5079. 36

Harlow, F. H. and Welch, J. E. (**1965**): Numerical calculation of time-dependent viscous incompressible flow with free surface. *Phys. Fluids*, **8**, 2182–2189. 10

Harman, I. N., Barlow, J. F. and Belcher, S. E. (**2004**): Scalar transport from urban surfaces. Part II. Model. *Boundary-Layer Meteorol.*, **113**, 387–409. 49

Hassan, A. A. and Crowther, J. M. (**1998**): Modelling of fluid flow and pollutant dispersion in a street canyon. *Environmental Monitoring and Assessment*, **52**, 281–297. 39

Helbig, A., Baumüller, J. and Kerschgens, M. J. (eds.) (**1999**): *Stadtklima und Luftreinhaltung*. Springer, Berlin, 2nd edn. ISBN 3-540-64206-4, 467 pp. 1, 77, 80

Hellsten, A. and Rautaheimo, P. (eds.) (**1999**): *Proceedings 8th ERCOFTAC/IAHR/COST Workshop on Refined Turbulence Modelling*. Helsinki University of Technology. 127. 36

Hirt, C. W. (**1993**): Volume-fraction techniques: powerful tools for wind engineering. *J. Wind Eng. Ind. Aerodyn.*, **46 & 47**, 327–338. 92

Holton, J. (**2004**): *An introduction to dynamic meteorology*, *International Geophysics Series*, vol. 88. Elsevier, 4th edn., 535 pp. 8, 41

Howard, L. (**1818**-**1820**): *The Climate of London deduced from meteorological observations*, vol. 1-2. Harvey & Darton, London, 1st edn. 1

Howard, L. (**1833**): *The Climate of London deduced from meteorological observations*, vol. 1-3. Harvey & Darton, London, 2nd edn. 1

Hoydysh, W. G. and Dabberdt, W. F. (**1988**): Kinematics and dispersion characteristics of flows in asymmetric street canyons. *Atmos. Environment*, **22**, 2677–2689. 38

Huang, H., Akutsu, Y., Arai, M. and Tamura, M. (**2000**): A two-dimensional air quality model in an urban street canyon: evaluation and sensitivity analysis. *Atmos. Environment*, **34**, 689–698. 39

Hunt, J. C. R., Carruthers, D. J., Britter, R. E. and Daish, N. C. (**2004**): *Dispersion from Accidental Releases in Urban Areas*. Atmospheric Dispersion Modelling Liaison Committee Report ADMLC/2002/3, 106 pp. 1, 40

Ichinose, T., Harada, I., Kataoka, K. and Lee, L.-T. (**2006**): Mitigation on atmospheric environment by a large restoration of inner-city river (Cheong-gye stream in Seoul) (in Japanese). *Proc. Annual Meeting of Environmental Systems Research*, **34**, 317–323. 1

Inagaki, A., Letzel, M. O., Raasch, S. and Kanda, M. (**2006**): Impact of surface heterogeneity on energy imbalance: a study using LES. *J. Meteor. Soc. Japan*, **84**, 187–198. 10

IPCC WGII (**2007**): *Climate Change 2007: Climate Change Impacts, Adaptation and Vulnerability. Fourth Assessment Report, Summary for Policymakers*. 23 pp. URL `http://www.ipcc.ch/SPM13apr07.pdf`. 1

Jansen, H. (**2004**): *Das Zeitschrittverfahren in PALM*. 28 pp. URL `http://www.muk.uni-hannover.de/~raasch/PALM_group/doc/tec/numerik.heiko/zeitschrittverfahren.pdf`. 14

Jensen, N., Olbrich, S., Pralle, H. and Raasch, S. (**2002**): An efficient system for collaboration in tele-immersive environments. In: **D. Bartz, X. Pueyo and E. Reinhard** (eds.), *Fourth Eurographics/ACM SIGGRAPH Workshop on Parallel Graphics and Visualization*. Blaubeuren, Germany, pp. 123–131. 74, 76

Jeong, S. J. and Andrews, M. J. (**2002**): Application of the k-ϵ turbulence model to the high Reynolds number skimming flow field of an urban street canyon. *Atmos. Environment*, **36**, 1137–1145. 39, 60

Jiménez, J. (**2003**): Computing high-Reynolds-number turbulence: will simulations ever replace experiments? *J. Turb.*, **4**, 1–14. 89

Jiménez, J. (**2004**): Turbulent flow over rough walls. *Ann. Rev. Fluid Mech.*, **36**, 173–196. 37

Johnson, G. T. and Hunter, L. J. (**1995**): A numerical study of dispersion of passive scalars in city canyons. *Boundary-Layer Meteorol.*, **75**, 235–262. 39

Kaimal, J. C. and Finnigan, J. J. (**1994**): *Atmospheric Boundary Layer Flows. Their Structure and Measurements.* Oxford University Press, New York-Oxford, 289 pp. 2, 64, 67

Kanda, M. (**2004**): Personal communication. 15

Kanda, M. (**2006**): Progress in the scale modeling of urban climate: Review. *Theor. Appl. Climatol.*, **84**, 23–33. 1, 38, 40

Kanda, M., Moriwaki, R. and Kasamatsu, F. (**2004**): Large eddy simulation of turbulent organized structures within and above explicitly resolved cube arrays. *Boundary-Layer Meteorol.*, **112**, 343–368. 7, 10, 15, 36, 40, 62, 63, 64

Kanda, M., Moriwaki, R. and Kimoto, Y. (**2005**): Temperature profiles within and above an urban canopy. *Boundary-Layer Meteorol.*, **115**, 499–506. 71

Kastner-Klein, P., Berkowicz, R. and Britter, R. (**2004**): The influence of street architecture on flow and dispersion in street canyons. *Meteorol. Atmos. Phys.*, **87**, 121–131. 40, 44, 72

Kastner-Klein, P., Fedorovich, E. and Rotach, M. W. (**2001**): A wind tunnel study of organised and turbulent air motions in urban street canyons. *J. Wind Eng. Ind. Aerodyn.*, **89**, 849–861. 40, 44

Kastner-Klein, P. and Rotach, M. W. (**2004**): Mean flow and turbulence characteristics in an urban roughness sublayer. *Boundary-Layer Meteorol.*, **111**, 54–84. 64, 67

Kataoka, H., Tamura, T., Okuda, Y. and Ohashi, M. (**2007**): Numerical evaluation of the wake field behind high-rise buildings by RANS and LES – Cross comparison among computed and wind-tunnel experimental results. In: *Twelfth International Conference on Wind Engineering, Caims, Australia.* 79, 85, 89

Kato, M. and Launder, B. E. (**1993**): The modelling of turbulent flow around stationary and vibrating square cylinders. In: *Proc. of the 9th Symp. on Turbulent Shear Flows*. 10-4-1. xviii, 21

Kawamura, T. (**1996**): *Ryūtai kaiseki I (Fluid mechanical analysis I, in Japanese)*. Asakura Shōten, Tōkyō. ISBN 4-254-11402-8, 173 pp. 15

Ketelsen, K. (**2002**): *Das Modell PALM auf IBM p690 Systemen. Portierung und Laufzeitoptimierung*. 12 pp. Unpublished Technical Report for HLRN. 18

Khan, I. M., Simons, R. R. and Grass, A. J. (**2005**a): Effect on turbulence production due to sudden change in flow regimes. *J. Hydr. Res.*, **43**, 549–555. 49

Khan, I. M., Simons, R. R. and Grass, A. J. (**2005**b): Upstream turbulence effect on pollution dispersion. *Env. Fluid Mech.*, **5**, 393–413.   49

Khan, M. I., Simons, R. R. and Grass, A. J. (**2006**): Influence of cavity flow regimes on turbulence diffusion coefficient. *J. Visualization*, **9**, 57–68.   49

Kim, H.-J., Noh, Y. and Raasch, S. (**2004**): Interaction between wind and temperature fields under the heterogeneous heat flux in the planetary boundary layer. *Boundary-Layer Meteorol.*, **111**, 225–246. Accepted.   10

Kim, J. and Moin, P. (**1985**): Application of a fractional-step method to incompressible Navier-Stokes equations. *J. Comput. Phys.*, **59**, 308–323.   14

Kim, J.-J. and Baik, J.-J. (**1999**): A numerical study of thermal effects on flow and pollutants dispersion in urban street canyons. *J. Appl. Meteor.*, **38**, 1249–1261.   70, 71

Kim, J.-J. and Baik, J.-J. (**2001**): Urban street-canyon flows with bottom heating. *Atmos. Environment*, **35**, 3395–3404.   39, 47, 60, 70, 71

Kim, J.-J. and Baik, J.-J. (**2003**): Effects of inflow turbulence intensity on flow and pollutant dispersion in an urban street canyon. *J. Wind Eng. Ind. Aerodyn.*, **91**, 309–329.   46

Kono, H. and Kusunoki, K. (**2004**): 3-D stream and vortexes in an urban canopy layer and transport of motor vehicle exhaust gas – wind tunnel experiment. In: *9th Int. Conf. on Harmonization within Atmospheric Dispersion Modelling for Regulatory Purposes*.   72

Kono, H. and Kusunoki, K. (**2005**): 3D stream and vortexes in the urban canopy layer and transport of motor vehicles exhaust gas. *Int. J. Environment and Pollution*, **25**, 177–190.   72, 92

Kovar-Panskus, A., Louka, P., Sini, J.-F., Savory, E., Czech, M., Abdelqari, A., Mestayer, P. G. and Toy, N. (**2002**a): Influence of geometry on the mean flow within urban street canyons – A comparison of wind tunnel experiments and numerical simulations. *Water, Air, and Soil Pollut. Focus*, **2**, 365–380.   39, 47, 50

Kovar-Panskus, A., Moulinneuf, L., Savory, E., Abdelqari, A., Sini, J.-F., Rosant, J.-M., Robins, A. and Toy, N. (**2002**b): A wind tunnel investigation of the influence of solar-induced wall-heating on the flow regime within a simulated urban street canyon. *Water, Air, and Soil Pollut. Focus*, **2**, 555–571.   44, 70

Krajnović, S. and Davidson, L. (**2002**): Large-eddy simulation of the flow around a bluff body. *AIAA Journal*, **40**, 927–936.   19, 36

Kratzer, A. (**1937**): *Das Stadtklima*. Vieweg, Braunschweig, 1st edn., 143 pp.   1

Kratzer, A. (**1956**): *Das Stadtklima*. Vieweg, Braunschweig, 2nd edn., 184 pp.   1

Kubota, T. and Miura, M. (**2002**): *A Study on the Planning Method of Residential Area in Consideration of Wind Flow for a Sustainable City - Wind tunnel tests on the wind flow in the residential areas of Tokyo*. *Tech. rep.*, Shibaura Institute of Technology, 307 Fukasaku, Saitama 330-8570, JAPAN. 14 pp.   85, 88

Lakehal, D. and Rodi, W. (**1997**): Calculation of the flow past a surface-mounted cube with two-layer turbulence models. *J. Wind Eng. Ind. Aerodyn.*, **67 & 68**, 65–78.   19, 21

Landsberg, H. E. (**1956**): The climate of towns. In: **W. L. Thomas, jr.** (ed.), *Man's role in changing the face of the Earth*, University of Chicago Press. pp. 584–603.   1

Landsberg, H. E. (**1981**): *The Urban Climate*, *International Geophysics Series*, vol. 28. Academic Press, 277 pp.   1, 5, 91

Launder, B. E. and Sharma, B. I. (**1974**): Application of the energy-dissipation model of turbulence to the calculation of flow near a spinning disc. *Lett. in Heat and Mass Transfer*, **1**, 131–138. xviii, 21

Launder, B. E. and Spalding, D. B. (**1974**): The numerical computation of turbulent flows. *Comput. Meth. Appl. Mech. Eng.*, **3**, 269–289. xviii, 21

Lee, I. Y. and Park, H. M. (**1994**): Parameterization of the pollutant transport and dispersion in urban street canyons. *Atmos. Environment*, **28**, 2343–2349. 39

Leonard, A. (**1974**): Energy cascade in large eddy simulation of turbulent fluid flows. *Adv. Geophys.*, **18 A**, 237–248. 9

Leonardi, S., Orlandi, P., Smalley, R. J., Djenidi, L. and Antonia, R. A. (**2003**): Direct numerical simulations of turbulent channel flow with transverse square bars on one wall. *J. Fluid. Mech.*, **491**, 229–238. 39, 50

Lesieur, M. (**1997**): *Turbulence in Fluids*. Kluwer Academic Publishers, Dordrecht, 3rd edn., 520 pp. 49, 74

Letzel, M. O. (**1999**): *Polynomial advection schemes for LES models*. MSc dissertation, Department of Meteorology, University of Reading, 80 pp. 14

Letzel, M. O. (**2001**): *Large-Eddy Simulations of Thermally-Induced Circulations in the Convective Boundary Layer*. Diplomarbeit, Institut für Meteorologie und Klimatologie, Universität Hannover, 86 pp. 4

Letzel, M. O. (**2007**): *"Large-Eddy Simulation Feasibility Study of Tsim Sha Tsui, Kowloon", Project Report for "Urban Climatic Map and Standards for Wind Environment – Feasibility Study"*. Tech. rep., Planning Department, The Government of the Hong Kong Special Administrative Region. 14 pp. 80, 88, 89

Letzel, M. O. and Gaus, G. (**2007**): Turbulent flow in a densely built-up area in Kowloon, downtown Hong Kong. *Dynamic Visualization in Science*. URL `http://www.dyvis.org/DyVis?Sig=13118`. Submitted. 85, 86, 87

Letzel, M. O., Gaus, G., Raasch, S. and Jensen, N. (**2007**): Turbulent flow around high-rise office buildings in downtown Tokyo. *Dynamic Visualization in Science*. URL `http://www.dyvis.org/DyVis?Sig=13100`. Submitted. 78, 79, 85

Letzel, M. O., Kanda, M. and Raasch, S. (**2005**): A new dimension of urban climate modelling with parallel large-eddy simulation. In: *Climate Analysis for Urban Planning: The 4th Japanese – German Meeting on Urban Climatology, 30 November - 2 December 2005 - Tsukuba, Japan*. 89

Letzel, M. O., Kanda, M. and Raasch, S. (**2006**): A new dimension of urban climate modelling with parallel large-eddy simulation. In: *Sixth Intl. Conf. on Urban Climate (ICUC-6)*. Göteborg, Sweden, pp. 296–299. 85

Letzel, M. O. and Raasch, S. (**2003**): Large-eddy simulations of thermally induced oscillations in the convective boundary layer. *J. Atmos. Sci.*, **60**, 2328–2341. 10

LeVeque, R. J. (**1992**): *Numerical methods for conservation laws*. Birkhäuser, Basel, 214 pp. 14

Li, X.-X., Liu, C.-H. and Leung, D. Y. C. (**2005**): Development of a k-ϵ model for the determination of air exchange rates for street canyons. *Atmos. Environment*, **39**, 7285–7296. 39, 46, 72

Li, X.-X., Liu, C.-H. and Leung, K. M., Dennis Y. C. Lam (**2006**): Recent progress in CFD modelling of wind field and pollutant transport in street canyons. *Atmos. Environment*, **40**, 5640–5658. 38, 40, 70

Liu, C.-H. and Barth, M. C. (**2002**): Large-eddy simulation of flow and transport in a modeled street canyon. *J. Appl. Meteor.*, **41**, 660–673. 46, 47, 72

Liu, C.-H., Barth, M. C. and Leung, D. Y. C. (**2004**): Large-eddy simulation of flow and pollutant transport in street canyons of different building-height-to-street-width ratios. *J. Appl. Meteor.*, **43**, 1410–1424. 39, 40, 44, 51, 72

Louis, J.-F. (**1979**): A parametric model of vertical eddy fluxes in the atmosphere. *Boundary-Layer Meteorol.*, **17**, 187–202. 17

Louka, P., Belcher, S. E. and Harrison, R. G. (**1998**): Modified street canyon flow. *J. Wind Eng. Ind. Aerodyn.*, **74-76**, 485–493. 44, 72

Louka, P., Belcher, S. E. and Harrison, R. G. (**2000**): Coupling between air flow in streets and the well-developed boundary layer aloft. *Atmos. Environment*, **34**, 2613–2621. 44, 45, 47, 50, 78

Louka, P., Vachon, G., Sini, J.-F., Mestayer, P. G. and Rosant, J.-M. (**2002**): Thermal effects on the airflow in a street canyon – Nantes'99 experimental results and model simulations. *Water, Air, and Soil Pollution: Focus*, **2**, 351–364. 70

Lugt, H. J. (**1983**): *Vortex Flow in Nature and Technology*. Wiley, 297 pp. 3, 47

Mahrer, Y. and Pielke, R. A. (**1978**): A test of an upstream spline interpolation technique for the advective terms in a numerical mesoscale model. *Mon. Wea. Rev.*, **106**, 818–830. 14

Mahrt, L. (**1986**): On the shallow motion approximations. *J. Atmos. Sci.*, **43**, 1036–1044. 8

Martinuzzi, R. (**1992**): *Experimentelle Untersuchung der Umströmung wandgebundener, rechteckiger, prismatischer Hindernisse*. Ph.D. thesis, Technische Fakultät, Universität Erlangen-Nürnberg. 19, 21, 23, 25, 30

Martinuzzi, R. and Tropea, C. (**1993**): The flow around a surface-mounted, prismatic obstacle placed in a fully developed channel flow. *J. Fluids Eng.*, **115**, 85–92. 19, 23, 25

Masson, V. (**2006**): Urban surface modeling and the meso-scale impact of cities. *Theor. Appl. Climatol.*, **84**, 35–45. 4, 40

Meneveau, C. and Katz, J. (**2000**): Scale-invariance and turbulence models fore large-eddy simulation. *Annu. Rev. Fluid Mech.*, **32**, 1–32. 15

Meroney, R. N., Pavageau, M., Rafailidis, S. and Schatzmann, M. (**1996**): Study of line source characteristics for 2-D physical modelling of pollutant dispersion in street canyons. *J. Wind Eng. Ind. Aerodyn.*, **62**, 37–56. 39, 44, 45, 51, 78

Mestayer, P. G. and Anquetin, S. (**1995**): Climatology of cities. In: **A. Gyr and F.-S. Rys** (eds.), *Diffusion and Transport of Pollutants in Atmospheric Mesoscale Flow Fields*, Kluwer, chap. VII. pp. 165–189. 1, 2

Mittal, R. and Iaccarino, G. (**2005**): Immersed boundary methods. *Ann. Rev. Fluid Mech.*, **37**, 239–261. 10, 92

Mochida, A. (**2006**): Personal communication. 92

Mochida, A. and Lun, Y. F. (**2006**): Prediction of wind environment and thermal comfort at pedestrian level in urban area. In: *Fourth Intl. Symp. on Computational Wind Engineering, CWE2006*. Yokohama, pp. 33–60. 80, 89

Moeng, C.-H. and Wyngaard, J. C. (**1988**): Spectral analysis of large-eddy simulations of the convective boundary layer. *J. Atmos. Sci.*, **45**, 3573–3587. 16

Moffatt, H. K. (1964): Viscous and resistive eddies near a sharp corner. *J. Fluid. Mech.*, **18**, 1–18. 44

Monin, A. S. and Obukhov, A. M. (1954): Osnovnye zakonomernosti turbulentnogo peremeshiv-anija v prizemnom sloe atmosfery (Basic laws of turbulent mixing in the atmosphere near the ground, in Russian). *Trudy geofiz. inst. AN SSSR*, **24 (151)**, 1963–1987. 16

Moriwaki, R. and Kanda, M. (2006): Flux-gradient profiles for momentum and heat over an urban surface. *Theor. Appl. Climatol.*, **84**, 127–135. 64, 67

Murakami, S. (1997): Current status and future trends in computational wind engineering. *J. Wind Eng. Ind. Aerodyn.*, **67 & 68**, 3–34. 89

Murakami, S., Ooka, R., Mochida, A., Yoshida, S. and Kim, S. (1999): CDF analysis of wind climate from human scale to urban scale. *J. Wind Eng. Ind. Aerodyn.*, **81**, 57–81. 89

Murakami, S., Uehara, K. and Komine, H. (1979): Amplification of wind speed at ground level due to construction of high-rise building in urban area. *J. Wind Eng. Ind. Aerodyn.*, **4**, 343–370. 84

Nakamura, Y. and Oke, T. R. (1988): Wind, temperature and stability conditions in an east-west oriented urban canyon. *Atmos. Environment*, **22**, 2691–2700. 38

Offerle, B., Eliasson, I., Grimmond, C. S. B. and Holmer, B. (2007): Surface heating in relation to air temperature, wind and turbulence in an urban street canyon. *Boundary-Layer Meteorol.*, **122**, 273–292. 70, 71

Oke, T. R. (1987): *Boundary layer climates*. Routledge, London, 2nd edn., 435 pp. 2

Oke, T. R. (1988): Street design and urban canopy layer climate. *Energy and Buildings*, **11**, 103–113. 37, 38

Oke, T. R. (1995): The heat island of the urban boundary layer: Characteristics, causes and effects. In: **J. E. Cermak, A. G. Davenport, E. J. Plate and D. X. Viegas** (eds.), *Wind Climate in Cities*, Kluwer Academic Publishers, Dordrecht, *NATO ASI Series E: Applied Sciences*, vol. 277. pp. 81–107. 1

Oke, T. R. (2006): Towards better scientific communication in urban climate. *Theor. Appl. Climatol.*, **84**, 179–190. 1

Olbrich, S., Pralle, H. and Raasch, S. (2001): Using streaming and parallelization techniques for 3D visualization in a high-performance computing and networking environment. *Lecture Notes in Computer Science*, **2110**, 231–240. 74, 75, 76

Panofsky, H. A. and Dutton, J. A. (1984): *Atmospheric turbulence. Models and methods for engineering applications*. John Wiley & Sons, New York, 397 pp. 64, 65

Patrinos, A. A. N. and Kistler, A. L. (1977): A numerical study of the Chicago lake breeze. *Boundary-Layer Meteorol.*, **12**, 93–123. 14

Pavageau, M. and Schatzmann, M. (1999): Wind tunnel measurements of concentration fluctu-ations in an urban street canyon. *Atmos. Environment*, **33**, 3961–3971. 51, 78

Perry, A. E., Schofield, W. H. and Joubert, P. N. (1969): Rough wall turbulent boundary layers. *J. Fluid. Mech.*, **37**, 383–413. 37

Piacsek, S. A. and Williams, G. P. (1970): Conservation properties of convection difference schemes. *J. Comput. Phys.*, **6**, 392–405. 11, 14

Pielke, R. A. (**2002**): *Mesoscale meteorological modeling, International Geophysics Series*, vol. 78. Academic Press, San Diego. 3, 10

Piomelli, U. and Balaras, E. (**2002**): Wall-layer models for large-eddy simulations. *Ann. Rev. Fluid Mech.*, **34**, 349–374. 16

Poggi, D., Katul, G. G. and Albertson, J. D. (**2004**): A note on the contribution of dispersive fluxes to momentum transfer within canopies. *Boundary-Layer Meteorol.*, **111**, 615–621. 62

Pope, S. B. (**2000**): *Turbulent flows*. Cambridge University Press, Cambridge, 771 pp. 45, 46, 47, 74

Price, G. V. and MacPherson, A. K. (**1973**): A numerical weather forcasting method using cubic splines on a variable grid. *Mon. Wea. Rev.*, **12**, 1102–1113. 11

Raabe, A., Arnold, K., Ziemann, A., Beyrich, F., Leps, J.-P., Bange, J., Zittel, P., Spieß, T., Foken, T., Göckede, M., Schröter, M. and Raasch, S. (**2005**): STINHO – Structure of turbulent transport under inhomogeneous surface conditions – part 1: The micro-α scale field experiment. *Meteorol. Z.*, **14**, 315–327. 10

Raasch, S. and Etling, D. (**1991**): Numerical simulation of rotating turbulent thermal convection. *Beitr. Phys. Atmosph.*, **64**, 185–199. 7, 8

Raasch, S. and Etling, D. (**1998**): Modeling deep ocean convection: Large eddy simulation in comparison with laboratory experiments. *J. Phys. Oceanog.*, **28**, 1786–1802. 7

Raasch, S. and Harbusch, G. (**2001**): An analysis of secondary circulations and their effects caused by small-scale surface inhomogeneities using large-eddy simulation. *Boundary-Layer Meteorol.*, **101**, 31–59. 10

Raasch, S. and Schröter, M. (**2001**): PALM – A large-eddy simulation model performing on massively parallel computers. *Meteorol. Z.*, **10**, 363–372. 7, 15, 18

Rafailidis, S. (**1997**): Influence of building areal density and roof shape on the wind characteristics above a town. *Boundary-Layer Meteorol.*, **85**, 255–271. 44, 72

Rafailidis, S. (**2000**): Nearfield geometry effects on urban street canyon measurements for model validation. *Int. J. Environment and Pollution*, **14**, 538–546. 44, 72

Ratti, C., Di Sabatino, S. and Britter, R. (**2006**): Urban texture analysis with image processing techniques: winds and dispersion. *Theor. Appl. Climatol.*, **84**, 77–90. 11

Raupach, M. R., Finnigan, J. J. and Brunet, Y. (**1996**): Coherent eddies and turbulence in vegetation canopies: The mixing-layer analogy. *Boundary-Layer Meteorol.*, **78**, 351–382. 45

Reynolds, O. (**1895**): On the dynamical theory of incompressible viscous fluids and the determination of the criterion. *Phil. Trans. Roy. Soc. London*, **A186**, 123–164. 9

Robins, A. (**2003**): Wind tunnel dispersion modelling some recent and not so recent achievements. *J. Wind Eng. Ind. Aerodyn.*, **91**, 1777–1790. 1

Robins, A. and Macdonald, R. W. (**2001**): *Review of flow and dispersion in the vicinity of groups of buildings*, Atmospheric Dispersion Modelling Liaison Committee Report No. NRPB-R322 Annex B. ISBN 0-85951-454-4, pp. 53–158. 1, 40, 78, 92

Rodi, W. (**1991**): Experience with two-layer models combining the k-ϵ model with a one-equation model near the wall. *AIAA Paper*, 91–0216. xviii, 21

Rodi, W. (**1997**): Comparison or LES and RANS calculations of the flow around bluff bodies. *J. Wind Eng. Ind. Aerodyn.*, **69-71**, 55–75. 19

Rodi, W. (**1998**): Large-eddy simulations of the flow past bluff bodies: State-of-the-art. *JSME Int. J. Ser. B*, **41**, 361–374. 19

Rodi, W., Ferziger, J. H., Breuer, M. and Pourquié, M. (eds.) (**1995**): *Workshop on Large Eddy Simulation of Flows past Bluff Bodies*. Rottach-Egern, Germany. 19, 20, 23, 30, 31, 35

Rodi, W., Ferziger, J. H., Breuer, M. and Pourquié, M. (**1997**): Status of Large Eddy Simulation: Results of a workshop. *J. Fluids Eng.*, **119**, 248–262. 19, 20

Rotach, M. W. (**1995**): Profiles of turbulence statistics in and above an urban street canyon. *Atmos. Environment*, **29**, 1473–1486. 40, 67

Rotach, M. W., Vogt, R., Bernhofer, C., Batchvarova, E., Christen, A., Clappier, A., Feddersen, B., Gryning, S.-E., Martucci, G., Mayer, H., Mitev, V., Oke, T. R., Parlow, E., Richner, H., Roth, M., Roulet, Y.-A., Ruffieux, D., Salmond, J. A., Schatzmann, M. and Voogt, J. A. (**2005**): BUBBLE – an urban boundary layer meteorology project. *Meteorol. Atmos. Phys.*, **81**, 231–261. 2

Roth, M. (**2000**): Review of atmospheric turbulence over cities. *Quart. J. R. Meteorol. Soc.*, **126**, 941–990. 40, 57, 64, 67

Sagaut, P. (**2006**): *Large Eddy Simulation for Incompressible Flows*. Springer-Verlag, Berlin/Heidelberg/New York, 3rd edn., 556 pp. 4, 8, 10, 15, 16

Sanada, S., Iwasa, Y. and Yoshida, M. (**1980**): Full-scale measurement of environmental wind in the Shinjuku New Metropolitain Center. *J. Wind Eng. Ind. Aerodyn.*, **6**, 291–309. 84

Santiago, J. and Martín, F. (**2005**): Modelling the air flow in symmetric and asymmetric street canyons. *Int. J. Environment and Pollution*, **25**, 145–154. 39

Santos, J. M., Griffiths, R. F., Roberts, I. D. and Reis, N. C., Jr. (**2005**): A field experiment on turbulent concentration fluctuations of an atmospheric tracer gas in the vicinity of a complex-shaped building. *Atmos. Environment*, **39**, 4999–5012. 45

Schatzmann, M. and Leitl, B. (**2002**): Validation and application of obstacle-resolving urban dispersion models. *Atmos. Environment*, **36**, 4811–4821. 5

Schlichting, H. and Gersten, K. (**2006**): *Grenzschicht-Theorie*. Springer, 10th edn. ISBN 3-540-23004-1, 799 pp. 45, 47

Schlittgen, R. and Streitberg, B. H. J. (**2001**): *Zeitreihenanalyse*. R. Oldenbourg Verlag, München, 9th edn. ISBN 3-486-25725-0, 571 pp. 67

Schönwiese, C. D. (**2006**): *Praktische Statistik für Meteorologen und Geowissenschaftler*. Gebrüder Bornträger, Berlin-Stuttgart, 4th edn., 302 pp. 67

Schröter, M. (**2003**): *Untersuchung der Evolution von Konvektionsstrukturen bei Kaltluftausbrüchen mit Hilfe eines parallelisierten Grubstrukturmodells*. Ph.D. thesis, Institut für Meteorologie und Klimatologie, Universität Hannover. 14, 18

Schröter, M., Raasch, S. and Jansen, H. (**2005**): New results on the cell broadening problem during cold air outbreaks from high resolution large-eddy simulations. *J. Atmos. Sci.*, **62 (6)**, 2023–2032. 10

Schumann, U. (**1973**): *Ein Verfahren zur direkten numerischen Simulation turbulenter Strömungen in Platten- und Ringspaltkanälen und über seine Anwendung zur Untersuchung von Turbulenzmodellen*. Ph.D. thesis, Universität Karlsruhe, Fakultät für Maschinenbau, Kernforschungszentrum Karlsruhe KFK 1854. 8

Schumann, U. (1975): Subgrid scale model for finite difference simulations of turbulent flows in plane channels and annuli. *J. Comput. Phys.*, **18**, 376–404. 8

Schumann, U. and Sweet, R. A. (1988): Fast Fourier transforms for direct solution of Poisson's equation with staggered boundary conditions. *J. Comput. Phys.*, **75**, 123–137. 15

Settles, G. S. (2006): Fluid mechanics and homeland security. *Ann. Rev. Fluid Mech.*, **38**, 87–110. 1

Shah, K. B. and Ferziger, J. H. (1997): A fluid mechanicians view of wind engineering: Large eddy simulation of flow past a cubic obstacle. *J. Wind Eng. Ind. Aerodyn.*, **67 & 68**, 211–224. 19, 24, 36, 74

Shankar, P. N. and Deshpande, M. D. (2000): Fluid mechanics in the driven cavity. *Ann. Rev. Fluid Mech.*, **32**, 93–136. 44, 57

Sini, J.-F., Anquetin, S. and Mestayer, P. G. (1996): Pollutant dispersion and thermal effects in urban street canyons. *Atmos. Environment*, **30**, 2659–2677. 39, 60, 70

Smagorinsky, J. (1963): General circulation experiments with the primitive equation. Part 1: The basic experiment. *Mon. Wea. Rev.*, **91**, 99–164. 15, 24

Smits, A. J. and Wood, D. H. (1985): The response of turbulent boundary layers to sudden perturbations. *Ann. Rev. Fluid Mech.*, **17**, 321–358. 2, 44

So, E. S. P., Chan, A. T. Y. and Wong, A. Y. T. (2005): Large-eddy simulations of wind flow and pollutant dispersion in a street canyon. *Atmos. Environment*, **39**, 3573–3582. 39

Sorbjan, Z. (1986): On similarity in the atmospheric boundary layer. *Boundary-Layer Meteorol.*, **34**, 377–397. 16

Sorbjan, Z. (1989): *Structure of the atmospheric boundary layer*. Prentice Hall, Englewood Cliffs, NJ, 317 pp. 1, 16

Souch, C. and Grimmond, S. (2006): Applied climatology: urban climate. *Progr. Phys. Geogr.*, **30**, 270–279. 1

Soulhac, L., Méjean, P. and Perkins, R. J. (2001): Modelling the transport and dispersion of pollutants in street canyons. *Int. J. Environment and Pollution*, **16**, 404–416. 39

Steinfeld, G., Letzel, M. O., Raasch, S., Kanda, M. and Inagaki, A. (2007): Spatial representativeness of single tower measurements and the imbalance problem with EC fluxes – results of an LES study. *Boundary-Layer Meteorol.*, **123**, 77–98. 10

Stoesser, T., Mathey, F., Fröhlich, J. and Rodi, W. (2003): LES of flow over multiple cubes. *ERCOFTAC Bull.*, **56**. 36

Stull, R. B. (1988): *An Introduction to Boundary Layer Meteorology*. Kluwer Academic Publishers, Dordrecht, 666 pp. 1, 8, 15, 68

Team Clean (2003): *Report on Measures to Improve Environmental Hygiene in Hong Kong*. Tech. rep., The Government of the Hong Kong Special Administrative Region. 80

Temam, R. (1969): Sur l'approximation de la solution des équations de Navier-Stokes par la méthode des pas fractionnaires I. *Arch. Rat. Mech. Anal.*, **32**, 135–153. 14

Thomas, T. G. and Williams, J. J. R. (1999): Large eddy simulation of vortex shedding from cubic obstacle. *J. Aerosp. Eng.*, **12**, 113–121. 92

Tominaga, Y., Yoshie, R., Mochida, A., Kataoka, H., Harimoto, K. and Nozu, T. (**2005**): Cross comparisons of CFD prediction for wind environment at pedestrian level around buildings. comparison of results for flowfield around building complex in actual urban area. In: *The Sixth Asia-Pacific Conference on Wind Engineering (APCWE-VI)*. Seoul, Korea. 92

Tseng, Y.-H., Meneveau, C. and Parlange, M. B. (**2006**): Modeling flow around bluff bodies and predicting urban dispersion using large eddy simulation. *Environ. Sci. Technol.*, **40**, 2653–2662. 19, 36, 82, 89

Uehara, K., Murakami, S., Oikawa, S. and Wakamatsu, S. (**2000**): Wind tunnel experiments on how thermal stratification affects flow in and above urban street canyons. *Atmos. Environment*, **34**, 1553–1562. 40, 70

Uno, I., Cai, X.-M., Steyn, D. G. and Emori, S. (**1995**): A simple extension of the Louis method for rough surface layer modelling. *Boundary-Layer Meteorol.*, **76**, 395–409. 17

Van Driest, E. R. (**1956**): On turbulent flow near a wall. *J. Aeronautical Sciences*, **23**, 1007–1011. 22

Vardoulakis, S., Fisher, B. E. A., Pericleous, K. and Gonzalez-Flesca, N. (**2003**): Modelling air quality in street canyons: a review. *Atmos. Environment*, **37**, 155–182. 37

VDI/DIN Kommission Reinhaltung der Luft (**2005**): *Environmental meteorology – Prognostic microscale wind field models – Evaluation for flow around buildings and obstacles*. VDI/DIN-Handbuch Reinhaltung der Luft. Beuth, Berlin, 53 pp. VDI 3783 part 9. 92

Viecelli, J. A. (**1971**): A computing method for incompressible flows bounded by moving walls. *J. Comput. Phys.*, **8**, 119–143. 92

Walton, A. and Cheng, A. Y. S. (**2002**): Large-eddy simulation of pollution dispersion in an urban street canyon – Part II: idealised canyon simulation. *Atmos. Environment*, **36**, 3615–3627. 39, 40, 46

Wang, X. and McNamara, K. F. (**2005**): Numerical and wind tunnel simulation of pollutant dispersion in the near wake of buildings. *Wind and Structures*, **8**, 427–442. 21

Weil, J. C., Sullivan, P. P. and Moeng, C.-H. (**2004**): The use of large-eddy simulations in lagrangian particle dispersion models. *J. Atmos. Sci.*, **61**, 2877–2887. 77

Weinbrecht, S. and Raasch, S. (**2001**): High resolution simulations of the turbulent flow in the vicinity of an Arctic lead. *J. Geophys. Res.*, **106 (C11)**, 27035–27046. 10

Weinbrecht, S., Raasch, S., Ziemann, A., Arnold, K. and Raabe, A. (**2004**): Comparison of large-eddy simulation data with spatially averaged measurements obtained by acoustic tomography – presuppositions and first results. *Boundary-Layer Meteorol.*, **111**, 441–465. 5

Wu, J.-Z., Ma, H.-Y. and Zhou, M.-D. (**2006**): *Vorticity and Vortex Dynamics*. Springer, Berlin. ISBN 3-540-29027-3, 778 pp. 49

Xie, X., Liu, C.-H., Leung, D. Y. C. and Leung, M. K. H. (**2006**): Characteristics of air exchange in a street canyon with ground heating. *Atmos. Environment*, **40**, 6396–6409. 47, 70

Xie, Z. and Castro, I. P. (**2006**): LES and RANS for turbulent flow over arrays of wall-mounted obstacles. *Flow Turbulence Combust.*, **76**, 291–312. 36

Yakhot, V., Orszag, S. A., Tangham, S., Gatski, T. B. and Speziale, C. G. (**1992**): Development of turbulence models for shear flows by a double expansion technique. *Phys. Fluids A*, **4**, 1510–1520. xviii, 21

Yamartino, R. J. and Wiegand, G. (**1986**): Development and evaluation of simple models for the flow, turbulence and pollutant concentration fields within an urban street canyon. *Atmos. Environment*, **20**, 2137–2156. 38

Curriculum Vitae

Family Name	Letzel
First Name	Marcus Oliver
Date of birth	01 February 1974
Place of birth	Heessen (now Hamm), Germany
Nationality	German
Religion	Roman-Catholic
Family Status	Married, one child

Academic career	since 04/2002 Research Assistant, Institute of Meteorology and Climatology, Leibniz University of Hannover, Germany; DFG research project on "High resolution Large-Eddy Simulation of turbulent flow around buildings with thermal effects"
	04/2001–03/2002 Postgraduate Research Student, Department of International Development Engineering (Kanda-ken), Tokyo Institute of Technology, Japan

University Education	03/2001 German "Diplom" in Meteorology on "Large-Eddy Simulations of Thermally-Induced Circulations in the Convective Boundary Layer"
	10/1999–03/2001 Meteorology, Leibniz University of Hannover, Germany
	09/1997–09/1999 Meteorology, University of Reading, United Kingdom, Master of Science in "Weather, Climate and Modelling" (distinction)
	10/1993–09/1997 Meteorology, Leibniz University of Hannover, Germany

Higher Education	08/1984–06/1993 Freiherr-vom-Stein Grammar School, Hamm, Germany

Awards	March 2002 Japan Society of Civil Engineers Best Paper Price of the 46th "Suiko" (Water Civil Engineering) Conference for the paper Kanda et al. (2002).
	08/1996–06/2005 Scholarships awarded by the "Studienstiftung des deutschen Volkes" (German National Academic Foundation)

List of primary publications

Letzel, M. O. and Gaus, G. (2007): Turbulent flow in a densely built-up area in Kowloon, downtown Hong Kong. *Dynamic Visualization in Science*. URL `http://www.dyvis.org/DyVis?Sig=13118`. Submitted.

Letzel, M. O., Gaus, G., Raasch, S. and Jensen, N. (2007): Turbulent flow around high-rise office buildings in downtown Tokyo. *Dynamic Visualization in Science*. URL `http://www.dyvis.org/DyVis?Sig=13100`. Submitted.

Steinfeld, G., Letzel, M. O., Raasch, S., Kanda, M. and Inagaki, A. (2007): Spatial representativeness of single tower measurements and the imbalance problem with EC fluxes – results of an LES study. *Boundary-Layer Meteorol.*, **123**, 77–98.

Inagaki, A., Letzel, M. O., Raasch, S. and Kanda, M. (2006): Impact of surface heterogeneity on energy imbalance: a study using LES. *J. Meteor. Soc. Japan*, **84**, 187–198.

Kanda, M., Inagaki, A., Letzel, M. O., Raasch, S. and Watanabe, T. (2004): LES study on the energy imbalance problem with eddy covariance fluxes. *Boundary-Layer Meteorol.*, **110**, 381–404.

Inagaki, A., Kanda, M., Letzel, M. O. and Raasch, S. (2003): LES study of the energy imbalance problem for heterogeneous surface (in Japanese). *Annual J. Hydraulic Eng., JSCE*, **47**, 37–42.

Letzel, M. O. and Raasch, S. (2003): Large-eddy simulations of thermally induced oscillations in the convective boundary layer. *J. Atmos. Sci.*, **60**, 2328–2341.

Kanda, M., Letzel, M. O., Inagaki, A. and Raasch, S. (2002): Investigation on spatial representativeness of point measurements – implication for imbalance problem (in Japanese). *Annual J. Hydraulic Eng., JSCE*, **46**, 97–102.

Letzel, M. O. and Raasch, S. (2002): Large-eddy simulations of thermally induced oscillations in the convective boundary layer. *Annual J. Hydraulic Eng., JSCE*, **46**, 67–72.

List of secondary publications

Letzel, M. O. (2007): "Large-Eddy Simulation Feasibility Study of Tsim Sha Tsui, Kowloon", Project Report for "Urban Climatic Map and Standards for Wind Environment – Feasibility Study", Planning Department, The Government of the Hong Kong Special Administrative Region, 14 pp.

Letzel, M. O. (2001): Large-Eddy Simulations of Thermally-Induced Circulations in the Convective Boundary Layer. Diplomarbeit, Institut für Meteorologie und Klimatologie, Leibniz Universität Hannover, 86 pp.

Letzel, M. O. (1999): Polynomial advection schemes for LES models. MSc dissertation, Department of Meteorology, University of Reading, 80 pp.